LARGE EDDY SIMULATIONS OF AIRCRAFT ICING AERODYNAMICS

By
Brett Bornhoft and Parviz Moin

Prepared with support from
The Boeing Company,
NASA's Transformational Tools and Technologies (T3) Project, and
the Department of Defense (DoD) SMART Fellowship

Report No. TF-195

Flow Physics and Computational Engineering Group
Department of Mechanical Engineering
Stanford University
Stanford, CA 94305

June 2024

Large Eddy Simulations of Aircraft Icing Aerodynamics

By

Brett Bornhoft and Parviz Moin

Prepared with support from
The Boeing Company,
NASA's Transformational Tools and Technologies (T3) Project, and
the Department of Defense (DoD) SMART Fellowship

Report No. TF-195

Flow Physics and Computational Engineering Group
Department of Mechanical Engineering
Stanford University
Stanford, CA 94305

June 2024

Abstract

Predicting the aerodynamic performance of aircraft in icing conditions is crucial for ensuring flight safety. Modeling icing and its effect on aerodynamics has recently garnered attention in academia and industry due to the changes to the Code of Federal Regulations (CFR) in 2007 and 2014 [89, 90]. The changes state that the certification of transport-category airplanes requires the same handling/performance in both icing and non-icing conditions. This has motivated airplane designers to include icing effects in the first stage of the design process. The accurate prediction of the effects of ice shapes on the aerodynamic performance of airfoils and wings is considered an industry gap that we address in this dissertation [76].

Encouraged by recent studies using large eddy simulations (LES) that demonstrate the ability to predict stall characteristics on full aircraft with smooth wings at an affordable cost [49], this dissertation applies this methodology to icing conditions. Using laser-scanned, detailed representations of the icing geometries, wall-modeled LES (WMLES) calculations are conducted to compare integrated loads against experimental measurements in a variety of icing conditions, including early-time glaze, early-time rime, streamwise, horn, and spanwise ridge ice formations. These ice geometries, mounted to a NACA23012 airfoil, span the space of ice shape types as described in [11]. Good agreement is achieved for the early-time glaze, streamwise, horn, and spanwise ridge ice geometries. At low angles of attack, reduced span representations were adequate to capture the aerodynamic quantities of interest (lift, drag, moments, and pressure distributions), but at high angles of attack (at and beyond the stall angle), it was shown that using larger spanwise extents is necessary for achieving an accurate representation of the aerodynamic performance coefficients. In contrast to the other geometries, the rime ice geometry simulations showed inaccurate predictions of the quantities of interest. This is attributed to the resolution of the roughness elements, which was completely sub-grid at the resolutions tested. To address this issue, a new roughness wall model is developed.

For a turbulent rough-wall flow, it is known that the outer layer of a turbulent boundary layer is independent of wall roughness effects except in the roughness's role in setting both the friction velocity and boundary layer thickness [62, 65]. Therefore, to appropriately model these effects, a database of direct numerical simulations (DNS) of rough-wall turbulent channel flows is constructed and used to parameterize the rough-wall turbulent boundary layer using three roughness parameters:

the root-mean-square roughness height, the surface effective slope, and its skewness. From this parameterization, we develop and introduce a velocity transformation for rough-wall turbulent flows and apply it as a modification to the equilibrium wall model (EQWM). This new wall model is then tested in both a turbulent channel flow and the early-time rime ice geometry. In both cases, we observe large improvements in both local quantities, such as velocity profiles, but also in integrated quantities, such as lift and drag, when augmenting the EQWM with the newly obtained roughness velocity transformation.

Lastly, a scaled common research model (CRM) swept wing geometry is introduced and simulated using both ice shapes generated from laser-scanning in tunnel ice accretion (denoted as a 'real' ice shape) and a modified geometry that only maintains the smooth maximum observed cross-section of the laser-scanned ice shape (denoted as an 'artificial' ice shape). These artificial ice shapes are often introduced as surrogate models for more realistic ice geometries. In this dissertation, we show that the introduction of artificial ice shapes causes unnecessary difficulties for LES approaches. In particular, these ice shapes introduce additional physics not present in the real-ice geometry, such as laminar boundary layers, laminar separation, and non-roughness-induced turbulence transition events. In contrast, WMLES simulations of the real-ice geometry are shown to be accurate at very coarse grid resolutions at a variety of Reynolds numbers. These conclusions motivate the need for better roughness representation in artificial ice geometries for the prediction of iced aircraft.

Overall, these efforts provide heightened confidence in the application of LES for accurately predicting the complex effects of ice shapes on aerodynamic performance in a wide variety of ice shapes and conditions.

Acknowledgments

Financial support from The Boeing Co., NASA's Transformational Tools and Technologies (T3) Project, and the Department of Defense (DoD) SMART Fellowship are acknowledged. The work conducted in this report was made possible by the computing resources awarded through the Oak Ridge Leadership Computing Facilities under the ALCC Allocation Award program.

We thank Dr. Sanjeeb Bose, Prof. Suhas S. Jain, and Dr. Konrad Goc for their collaboration on this work. We extend our gratitude to Mr. Adam Malone from The Boeing Co. and, Dr. Andy Broeren and Dr. Sam Lee of NASA Glenn Research Center for their assistance in preparing the laser-scanned geometry for our solvers and for valuable discussions.

Acronyms

ATR	Avions de Transport Régional
BC	Boundary Condition
CFD	Computational Fluid Dynamics
CFR	Code of Federal Regulations
CRM	Common Research Model
CRM-HL	High-Lift Common Research Model
CV	Control Volume
DES	Detached-Eddy Simulation
EQWM	Equilibrium Wall-Model
FAA	Federal Aviation Administration
HLPW	High-Lift Prediction Workshop
IRT	Icing Research Tunnel
KES	k^+_{rms}, ES_x, and s_k model
LBM	Lattice-Boltzmann Method
LES	Large-Eddy Simulation
LWC	Liquid Water Content
MAC	Mean Aerodynamic Chord
MVD	Mean Volumetric Diameter
NACA	National Advisory Committee for Aeronautics
NASA	National Aeronautics & Space Administration
NTSB	National Transportation Safety Board

RANS	Reynolds-averaged Navier-Stokes
RMS	Root mean square
RPM	Rapid Prototyping Methods
SLD	Supercooled Large Droplets
WMLES	Wall-Modeled Large-Eddy Simulation
WRLES	Wall-Resolved Large-Eddy Simulation

Nomenclature

α	angle of attack
β	Clauser parameter
ρ	density
ν	kinematic viscosity
μ	dynamic viscosity
κ	Von Kármán constant
ϵ	percent error
λ	thermal conductivity
δ	boundary layer thickness
Δ	grid cell size
τ_{ij}	stress tensor
τ_w	wall stress
a_c	slope of roughness sublayer
b	span
B	log-layer intercept
c	chord
C_D	drag coefficient
C_f	skin friction coefficient
C_L	lift coefficient
$C_{L,max}$	maximum lift coefficient
C_M	pitching moment coefficient

C_p	pressure coefficient
e	internal energy
E	total energy
ES	effective slope
h	displacement height
k	roughness length scale
k_s	equivalent sand-grain roughness
M	Mach number
n	wall normal coordinate
N_p	number of points
p	pressure
Q_i	heat flux
R	radius of curvature
Re	Reynolds number
Re_{MAC}	MAC-based Reynolds number
Re_c	chord-based Reynolds number
Re_τ	friction Reynolds number
s	streamwise coordinate
S_p	spanwise extent
s_k	skewness
T	temperature
T_t	total temperature
T_s	static temperature
t	time
U_∞	freestream velocity
u_τ	friction velocity
u_i	velocity components
ΔU^+	roughness function
ΔU^+_{RSL}	avg. velocity at $y = 0$
x_i	coordinate directions
$\bar{(\cdot)}$	Reynolds averaging
$\tilde{(\cdot)}$	Favre averaging

Contents

List of Tables

List of Figures

THIS PAGE DELIBERATELY LEFT BLANK

Chapter 1

Introduction

1.1 Certification of transport aircraft under icing conditions

Predicting the aerodynamic performance of an aircraft in icing conditions is critical, as failures in an aircraft's ice protection system can compromise flight safety. In response to a series of icing-related accidents, the Federal Aviation Administration (FAA) implemented a new ruling in 2007 that modified the regulations that govern today's aircraft, which are found in Title 14 Code of Federal Regulations (CFR) Part 25 for Airworthiness Standards: Transport Category Airplanes, by adding a requirement to certify that transport-category airplanes exhibit the same handling/performance in both icing and non-icing conditions [89]. A follow-on change to both Parts 25 and 33, adding Appendix O, came into effect in 2015 and focused on extending the new certification requirement to both airframes and engines operating in supercooled large droplet (SLD) and ice crystal icing conditions [90]. These rule changes were largely in response to the 1994 accident in Roselawn, Indiana, where an Avions de Transport Régional (ATR) 72 series airplane experienced an un-commanded roll. The National Transportation Safety Board (NTSB) determined that the accident was caused by freezing raindrops that created a spanwise ridge of ice downstream of the wing's deicing boot.

Prior to the addition of Appendix O, no certification was required for aircraft performance during freezing rain or drizzle events, which induce both SLD and ice crystals. The rule changes have drastically altered how aircraft manufacturers design their airplanes by requiring them to consider the effects of icing in the earliest stages of design. Early designs do not often include ice tunnel testing, primarily due to the cost associated with these tests. Therefore, aircraft designs under these rules rely heavily upon computational fluid dynamics (CFD) simulations. Historically, studying the aerodynamic effects of icing has typically relied on Reynolds-averaged Navier-Stokes (RANS) modeling. RANS models usually struggle to accurately predict the stall behavior, particularly in conditions in which the effect of ice accretion, at early times (less than one minute of accretion), is to only introduce surface roughness to an otherwise smooth surface [93]. The accretion of ice

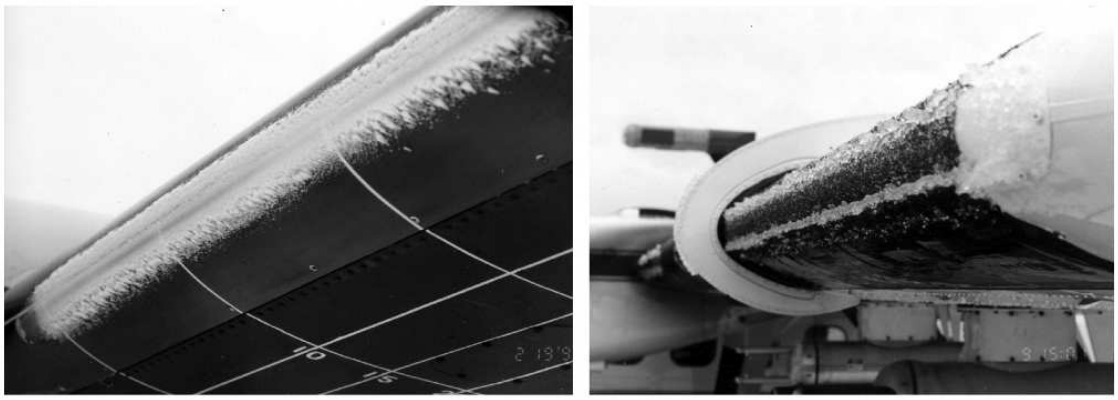

Figure 1.1: Icing examples from a post-flight test by the NASA Glenn Research Center's instrumented Twin Otter aircraft: (a) rime ice conditions and (b) glaze ice conditions.

on the surface of a wing drastically alters its stall characteristics, stability, and drag. Ice on wings introduces additional challenges for simulations, such as complex geometries, additional scales due to surface roughness, and non-trivial separation and reattachment behavior. Hence there is a clear need to accurately predict and model ice accretion and its effect on aerodynamics.

The two primary types of icing are rime and glaze [43, 86]. Rime ice typically occurs at low flight temperatures ($< -20°$C), low speeds, low atmospheric liquid water concentration, LWC, and small droplet sizes. Rapid and complete freezing of the droplets impacting the aerodynamic surfaces leads to opaque accretion of ice on the wing's leading edge, which is still streamlined. Rime ice's primary aerodynamic impact comes from its characteristic roughness. Glaze ice occurs at higher flight temperatures (near freezing), higher speeds, high atmospheric LWC, and large droplet sizes. Upon impact, the droplets still attach to nucleation points on the wing, but due to larger droplet sizes and higher temperatures, water will run back along the wing body and experience delayed freezing. This results in translucent and smoother ice covering the surface of the aircraft, and when exposed to icing conditions for a longer time, glaze ice leads to so-called horn ice conditions. Ice horns can drastically impact the aerodynamic performance of an aircraft by inducing separation at modest angles of attack, leading to an overall decrease in maximum lift and stall angle [43]. Figure 1.1 shows examples of (a) rime and (b) glaze ice from a flight test [86].

1.2 State-of-the-art of LES for complex aerodynamic flows

Recent advances in rapid, high-quality mesh generation, low-dissipation numerical schemes, and physics-based subgrid-scale and wall models have led to, for the first time, accurate simulations of a realistic aircraft in landing configuration in less than a day of turnaround time with modest resource

requirements [49]. Additionally, the fourth High-Lift Prediction Workshop (HLPW) has identified LES approaches as a leader in predicting quantities such as $C_{L,max}$ in high-lift landing/take-off configurations [94].

The investigation of the use of LES for aeronautical design was in part motivated by one of the Grand Challenge Problems in computational aerosciences identified in the NASA 2030 Computational Fluid Dynamics (CFD) Vision Report [99]: "LES of a powered aircraft configuration across the full flight envelope". The present use of CFD in the engineering design process has been mostly in cruise conditions. These operating points are largely characterized by attached boundary layers where the turbulence models used in traditional CFD approaches (often, but not exclusively, based on RANS closures) are relatively accurate. Other operating conditions, such as take-off or landing, experience more complex and unsteady phenomena, including boundary layer separation. The extension of the flight envelope through the use of LES has been realized in studies such as [66], where seven different HLPW participants simulated $C_{L,max}$ to within a 2% error [3, 44, 48, 61, 106, 115]. LES has been used to extend the computational analysis and flight envelope to effects such as evaluating wind tunnel effects [50], prediction of transonic buffet [47], and extension to higher Reynolds numbers [2].

Two established milestones in the application of LES to complex aerodynamic flow fields are used as motivation for the current dissertation. First, the accurate representation of the critical stall angle as well as $C_{L,max}$. Figure 1.2(a) shows predictions of the lift coefficient versus angle of attack for the NASA high-lift common research model (CRM-HL) (with different grid resolutions) compared to the experimental data. The calculations accurately predict the maximum lift as well as the onset of the stall [50]. Second, advancements in grid generation for complex shapes using Voronoi diagrams led to the simulation of a NACA65 compressor blade with multiple roughness heights [63]. For these cases, detailed descriptions of the roughness scales of the compressor blades do not exist; therefore, randomly distributed roughness patterns were generated (as shown in Figure 1.3(a)) that targeted root-mean-square roughness height normalized by chord, k_{rms}/c, values of 0, 1.6×10^{-3}, and 5.6×10^{-3}, respectively. In Figure 1.3(b), blade loading comparisons to experiments were made for the case with a $Re_c = 400,000$. Generally good agreement was observed, highlighting the capability to geometrically model and resolve roughness in relevant geometries. Given the state-of-the-art in modeling complex aerodynamic surfaces, this thesis aims to extend the applicability of LES to aerodynamic surfaces under icing conditions.

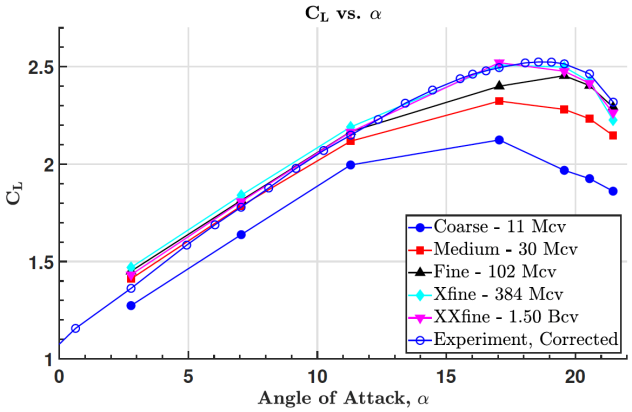

Figure 1.2: Lift curve (C_L versus α) with increasing grid resolution for the CRM-HL [50].

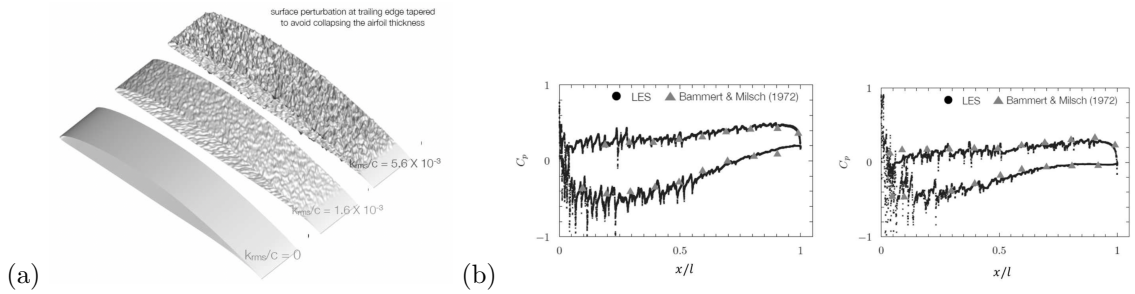

(a) (b)

Figure 1.3: (a) Geometry of the compressor blade with randomly distributed roughness elements. (b) Blade loadings of randomly distributed roughness cases; (left) $k_{rms}/c \approx 1.56 \times 10^{-3}$; (right) $k_{rms}/c \approx 5.56 \times 10^{-3}$ [63].

1.3 Current state-of-the-art in aerodynamic modeling performance of iced shapes

Most previous studies of icing predictions and its aerodynamic performance typically used lower-fidelity modeling approaches, such as the RANS equations [10, 27, 57, 68, 88]. More recently, glaze and horn ice shapes have been simulated using a variety of scale-resolving simulation approaches. In [84], a detached-eddy simulation (DES) method was used to study the aerodynamic performance of spanwise ridge ice shapes. Their results showed improved surface pressure distribution compared to RANS methods but exhibited worse agreement in the lift coefficient versus the angle-of-attack curve. This discrepancy arose because the RANS results had misleading error cancellations, which led to good agreement for the lift curve for incorrect reasons. Other hybrid RANS/LES approaches are used in [5, 36, 122] where two-dimensional horn and spanwise ridge shapes are simulated and compared with experimental data with marginal improvements in surface pressures and lift coefficients as

compared to RANS approaches. A lattice-Boltzmann method (LBM) was used in [69], where they simulated glaze and horn ice geometries that are considered in the present study. These simulations marked a first attempt at simulating complex roughness topologies in iced airfoils. We use the results of [69] as a baseline state-of-the-art literature for the glaze and horn ice geometries and to compare with our simulations. Further discussion of their results are made in Chapter 3, Sections 3.5.1, 3.5.2, and 3.5.3. The wall-modeled LES (WMLES) approaches of [119] and [117] focused on large two-dimensional ice shapes. In [119], a NLF-0414/623 airfoil was simulated with a large horn ice shape attached to the leading edge. Both the lift and drag coefficients showed large improvements over RANS methods, where the error in lift was reduced from 19% to approximately 1%. In [117], an immersed boundary method was utilized to simulate the complex horn ice shape of a 2D airfoil. Their wall-modeled approach improved upon the existing unsteady RANS methods, but ultimately underpredicted the lift coefficient in the post-stall region and the critical angle of attack.

Limited work has been conducted for three-dimensional geometries, such as swept wings. Early studies of iced-swept wing aerodynamics utilized RANS models for the NACA0012 airfoil with a 30° sweep angle [10, 68, 88]. In these cases, a reasonable agreement was observed for lower angles of attack, but for higher values, RANS-based methods struggled to predict the flow separation patterns accurately. More recent studies on simulations of iced-swept wings have used both RANS and hybrid-RANS/LES methods to simulate an artificial ice shape for a modified CRM65 wing [83, 100, 102]. In [100] and [102], good agreement was observed for lower angles of attack, but for higher values, quantities of interest such as C_L and C_D were underpredicted when using the RANS models. For the hybrid-RANS/LES approaches of [102], only two angles were simulated. Both had a reasonable agreement for the integrated quantities, such as lift and drag coefficients. Still, the C_P values showed both overprediction and underprediction in different regions, suggesting the cancellation of errors in the integrated quantities. The more recent work of [83] focused on simulations of the real-ice geometry used in the current study. Here, they filtered the roughness by 0.0003 meters to achieve a body-fitted unstructured mesh where a single scallop is approximately 0.005 meters. Utilizing RANS models, the resulting forces, moments, and pressure profiles were in reasonable agreement with the experimental data after sweeping a tuning parameter to a desired result.

While the existing literature has predominantly focused on large ice obstructions such as horns, ridges, and scallops and mostly in 2D airfoils with the extruded ice shape in the third dimension [101], it is noteworthy that higher-fidelity approaches have not yet been applied to rime ice shapes and airfoils with full 3D ice shape geometries. In light of this gap, this thesis aims to comprehensively evaluate WMLES for various ice shapes, including large and small ice accretions.

1.4 Roughness modeling for LES

The effects of ice on aerodynamic surfaces are closely linked to two length scales. The first represents the displacement height due to ice growth, h, and the second represents the roughness, k, of the ice surface, which is defined as a displacement height minus an average displacement height and is given by

$$k(\vec{\xi}) = h(\vec{\xi}) - \overline{h(\vec{\xi})} \tag{1.1}$$

where $\vec{\xi}$ represents a general coordinate system. Specific definitions of appropriate coordinate systems and averaging operators are provided in Chapter 3.2. Rough-wall turbulent flows have been studied in length outside of the icing community and are ubiquitous in fluid mechanics. Several critical components in various propulsion and turbomachinery devices are subject to conditions where the flow within the boundary layers interacts with surface roughness. For instance, wind turbines and aircraft lifting surfaces experience leading-edge ice accretion [15, 18], compressor blades suffer from erosive damage [104], turbine blades are roughened by molten particulate deposition [7, 56], and limited precision in additive manufacturing/3D printing engenders small-scale roughness [111]. In all of these instances, the presence of surface roughness compromises aerodynamic performance and operability.

Several different approaches exist for modeling roughness in simulations. We follow the broad categorization of [37], where roughness can be modeled using, the discrete element method (DEM) [6, 58, 103, 108], a local drag force model [21, 97], or from a wall boundary condition [95, 96, 121]. For the DEM, the governing equations are double-averaged, meaning first the temporal ensemble average followed by a spatial average, typically a planar average in the wall-normal direction. In the context of LES, this adds the following terms that require closures: the Reynolds stress, the dispersive stresses, and the body force due to the presence of the rough surface [37]. These additional closures can exacerbate the difficulty in roughness modeling but can serve as a way to better understand the detailed physics of rough-wall turbulent flows. The second approach of a local drag force assumes that the roughness acts as a local drag force on the flow. This approach requires a term that scales the drag as a function of the distance from the wall and the sand-grain roughness, k_s^+. This term often utilizes the actual rough surface and can be represented as a void fraction, or some calibrated representation of the scaling term as observed in [112]. While promising results have been shown in this modeling approach, it still requires meshes that cluster near the wall with wall-resolved limits. This incurs a computational cost for these cases and may not be suitable for iced airfoils where computational cost is critical to scale the approach to complex geometries.

The last approach is to modify the law of the wall given a modeled roughness function. This approach has worked well when wall-models matching location is consistently in the logarithmic layer [95] but is not designed to work when the resolutions approach that of the roughness sub-layer (RSL). Here, we have direct access to the iced geometries and, therefore, take a hybrid approach where we

utilize the marginally resolved surface and augment it either with the equilibrium wall-model [22], detailed in Chapter 2.3, or a transformed velocity profile that accounts for both the modification of the RSL and logarithmic layer of the rough-wall turbulent boundary layer (see Chapter 4).

1.5 Accomplishments

The following list summarizes the key contributions of this work:

- Established the utility of LES for the design of aircraft in icing conditions by conducting a comprehensive evaluation of WMLES for ice shapes across diverse conditions (glaze, rime, supercooled large droplets), including scenarios simulating ice formation past ice protection systems and on full-scale iced wings. Demonstrated and showed accurate prediction of lift, drag, moment, and pressure coefficients at moderate grid resolutions. Highlighted the need for enhanced grid resolution or modeling to accurately predict post-stall angles of attack under early-time rime conditions.
- Introduced a parameterized linear profile for the collapse of the roughness sub-layer (RSL), relying solely on roughness height, effective slope, and skewness.
- Developed a roughness function using just three averaged roughness parameters, outperforming existing two and three-parameter models derived from a newly constructed DNS database of rough-wall channel flows.
- Derived a rough-wall turbulent velocity transformation that collapses the velocity profiles in the DNS database from a combination of the RSL and roughness function models.
- Integrated the rough-wall velocity transformation as an augmentation to the equilibrium wall model, enabling accurate predictions of turbulent channel flows over rough surfaces and early-time rime ice conditions, including stall simulations, at coarse resolutions.
- Identified critical limitations in using artificial ice shapes with WMLES for predicting integrated aerodynamic loads. Demonstrated robust aerodynamic coefficient predictions for a real ice-swept wing geometry across varying grid resolutions and Reynolds numbers.

Chapter 2

Governing equations, physical models, & numerical methods

2.1 LES equations

We utilize LES to simulate the flow about various ice shapes. These methods rely on resolving the large scales and providing closure models for turbulence in the sub-grid regime. We solve the governing equations for a low-pass filtered, compressible Navier–Stokes system for mass, momentum, and total energy, which can be written as

$$\frac{\partial \bar{\rho}}{\partial t} + \frac{\partial \widetilde{u}_i \bar{\rho}}{\partial x_i} = 0, \tag{2.1}$$

$$\frac{\partial \bar{\rho}\widetilde{u}_i}{\partial t} + \frac{\partial \bar{\rho}\widetilde{u}_i\widetilde{u}_j}{\partial x_j} = -\frac{\partial \bar{p}}{\partial x_i} + \frac{\partial \widetilde{\tau}_{ij}}{\partial x_j} - \frac{\partial \tau_{ij}^{sgs}}{\partial x_j}, \tag{2.2}$$

$$\frac{\partial \bar{E}}{\partial t} + \frac{\partial \widetilde{u}_i \bar{E}}{\partial x_i} + \frac{\partial \widetilde{u}_i \bar{p}}{\partial x_i} = \frac{\partial \widetilde{\tau}_{ij}\widetilde{u}_i}{\partial x_j} - \frac{\partial \tau_{ij}^{sgs}\widetilde{u}_i}{\partial x_j} + \frac{\partial}{\partial x_i}\left(\lambda \frac{\partial \bar{T}}{\partial x_i}\right) - \frac{\partial Q_i^{sgs}}{\partial x_i}, \tag{2.3}$$

where $\widetilde{\cdot}$ and $\bar{\cdot}$ represent Favre–and Reynolds-averaged quantities, respectively, ρ is the density, $\vec{u}$ is the velocity, p is the pressure, $\widetilde{\tau}_{ij} = 2\mu(\widetilde{T})\widetilde{\mathbb{S}}_{ij} - 2\mu(\widetilde{T})(\partial \widetilde{u}_k/\partial x_k)\delta_{ij}/3$ is the resolved Cauchy stress tensor, $\mu(\widetilde{T})$ is the dynamic viscosity, $\widetilde{\mathbb{S}}_{ij} = \{(\partial \widetilde{u}_i/\partial x_j) + (\partial \widetilde{u}_j/\partial x_i)\}/2$ is the resolved strain-rate tensor, $\widetilde{E} = \bar{\rho}(\widetilde{e} + \widetilde{u}_i\widetilde{u}_i/2)$ is the resolved total energy per unit volume, λ is the thermal conductivity, and T is the temperature. The subgrid terms, denoted by superscript sgs, are the terms that account for the effect of subgrid stress and heat flux on the resolved scales and are defined as

$$\begin{aligned} \tau_{ij}^{sgs} &= \bar{\rho}(\widetilde{u_i u_j} - \widetilde{u}_i\widetilde{u}_j), \\ \vec{Q}_i^{sgs} &= \bar{\rho}(\widetilde{eu_i} - \widetilde{e}\widetilde{u_i}). \end{aligned} \tag{2.4}$$

The subgrid closures are modeled using the dynamic-Smagorinsky approach of [77].

2.2 Numerical modeling

The solver employed is charLES [49], a massively parallel, second-order, low-dissipation finite-volume solver. The numerical scheme is based on discretely kinetic energy–and entropy-preserving formulation [26, 59, 105] that has been shown to be suitable for coarsely resolved LES of turbulent flows that are especially sensitive to numerical dissipation. The discretization is suitable for arbitrary unstructured, polyhedral meshes, and the solutions contained herein are computed on unstructured grids constructed based on Voronoi diagrams. The use of Voronoi diagram-based meshes allows for the rapid and automatic generation of high-quality grids with some guaranteed properties (for instance, the vector between the centroids of two adjacent Voronoi sites is parallel to the normal of the face that they share). Hexagonaly Close-Packed (HCP) topologies are typically acquired from the seeding procedure that obtains the Voronoi diagram around the complex ice shapes. This approach is ideal for complex geometries because it results in a body-fitted mesh without the need for manual intervention, including in situations with the presence of realistic rough walls like in the current study. Figure 2.1 shows a zoomed-in view of an LES Voronoi grid adjacent to a rough wall. To achieve additional near-wall refinement, each finer mesh is obtained by homothetically refining the near-wall cells by a factor of two. Each additional layer adds ten cells in the wall-normal direction and isotropically refines the elements in the other two directions. The time advancement is performed using a three-stage explicit Runge Kutta scheme [52], and the spatial discretization is formally second-order accurate. Additional details on the numerical discretization and the grid generation can be found in [42], [73], and [12].

2.3 Wall modeling

In a wall-modeled LES, only turbulent eddies that scale with the boundary layer thickness are resolved and the remaining effect of the near-wall region is modeled, resulting in significant computational cost savings. In this work, near-wall regions are modeled using an equilibrium wall-modeling approach in which we assume the pressure gradient balances the advective terms, which leads to the constant stress layer approximation [9],

$$\frac{d\tau}{dn} = \frac{d}{dn}\left(\mu\frac{dU}{dn} - \overline{\rho u' v'}\right) = 0, \tag{2.5}$$

which can be solved for the wall stress, given the no-slip condition at the wall, a closure for Reynolds shear stress, and the velocity at the matching first grid point from the LES solution. The schematic in Figure 2.1 illustrates this procedure. Additional details on equilibrium wall modeling can be found

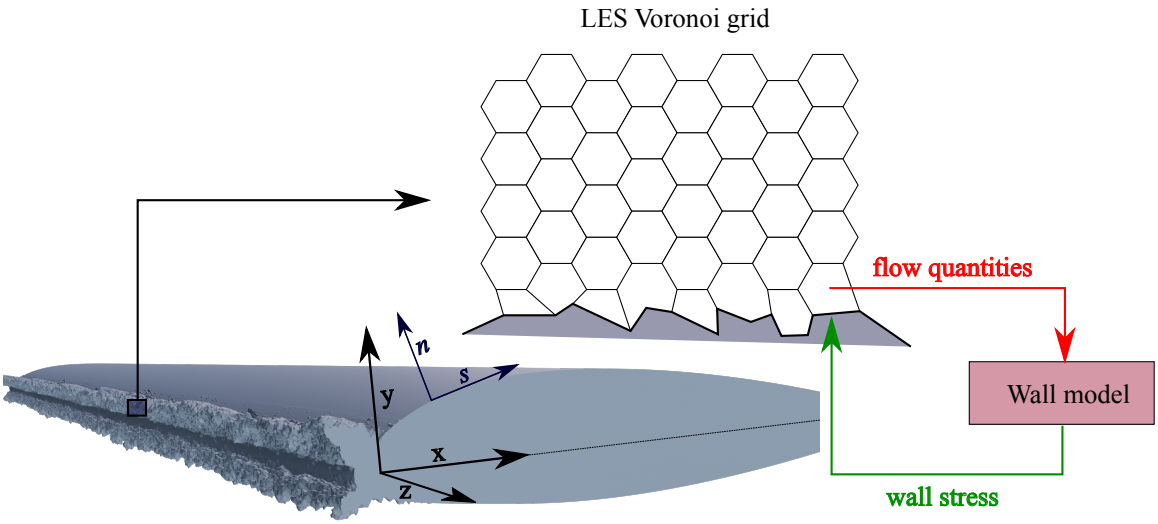

Figure 2.1: Schematic representing the wall modeling procedure.

in [49]. By leveraging the polyhedral element capabilities in the Voronoi diagram, one can simulate the complex topologies of a roughened surface. This marginally resolved rough surface boundary condition can either be simulated with the standard EQWM when enough resolution is provided in the near wall surface or by modifying the local boundary condition through an augmentation to the EQWM given the roughness correlation derived in Chapter 4.

Chapter 3

Large-eddy simulations of the NACA23012 airfoil with laser-scanned ice shapes[1]

3.1 Background

In this chapter, five ice shapes generated at NASA Glenn's Icing Research Tunnel (IRT) are simulated at multiple angles of attack [15]. These geometries target different icing environments, both early-time and longer-duration glaze and rime ice exposure events, including a geometry that results from using a thermal ice-protection system. At first, ice introduces only roughness to the surface, but after long accretion, large deformations are eventually introduced to the otherwise clean surface. Using the laser-scanned geometries, detailed representations of the three-dimensional ice geometries are resolved on the grid and simulated using wall-modeled LES. The viability of the WMLES as a tool to predict the effect of icing on aerodynamics in these various conditions is assessed. Integrated loads (lift, drag, and moment coefficients) and pressure distributions are compared against experimental measurements in both clean and iced conditions for several angles of attack in both pre-and post-stall regions.

Glaze ice formations exhibit larger and highly nonuniform ice features, such as 'horns', in contrast to rime ice formations characterized by smaller, uniformly distributed roughness elements. In wall-modeled LES, it was observed that larger roughness scales in the glaze ice that trigger transition can be accurately resolved. Therefore, it is possible for WMLES to accurately capture the aerodynamics

[1]This Chapter contains previously published work, adapted here with minor modifications, from the following reference: Bornhoft, B., Jain, S. S., Goc, K., Bose, S. T., & Moin, P. (2024). "Large-eddy simulations of the NACA23012 airfoil with laser-scanned ice shapes", Aerospace Science and Technology, 108957.

of glaze ice shapes without the need for additional modeling. In contrast, rime ice geometries required additional resolution to accurately represent the aerodynamic loads. This chapter demonstrates the effectiveness of the wall-modeled LES technique in simulating the complex aerodynamic effects of iced airfoils, providing valuable insights for aircraft design in icing environments and highlighting the importance of accurately representing ice geometries and roughness scales in simulations.

The chapter is organized as follows. Section 3.2 describes the general impact of ice on two-dimensional aerodynamic surfaces and 3.3 details the specific roughness encountered for each geometry. Section 3.4 details the setup for the simulations. A discussion of the computational results is provided in Section 3.5. The summary of the study and important conclusions are discussed in Section 3.11.

3.2 Effects of icing: experimental data

NASA Glenn's Icing Research Tunnel (IRT) has conducted research on the effect of ice accretion on aerodynamic bodies since 1944 [87]. The IRT creates a cloud of supercooled water droplets from a series of spray bars that target various droplet diameter ranges, LWC, and temperatures. Recently, laser-scanning techniques have been developed and tested for iced airfoils in the IRT [70]. This advancement provides digital representations of iced airfoils that can be used with rapid prototyping methods (RPM) for manufacturing ice shapes, which can then be used for wind tunnel testing.

Ice geometries obtained using the laser scanner are shown along with the clean NACA23012 geometry in Figure 3.1. Here, the ranges of k/c describes the roughness length scale, k, normalized by the clean airfoil chord length, c. The value of h is defined as the displacement height due to ice accretion with respect to the clean geometry. The value of k is defined, in this study, as the displacement height minus the average displacement height (averaged along the spanwise direction) and is given by

$$k(s,z) = h(s,z) - \overline{h(s)}. \tag{3.1}$$

We classify ice accretion using two length scales, whereby the ice geometrically modifies the airfoil outer mold line (represented by h) and also introduces additional roughness scales (represented by k). Here, k is evaluated for the whole surface and is known at each streamwise, s, and spanwise, z, locations (see Figure 2.1 for reference coordinates). Details of the ice shapes considered in this study and the specific IRT test conditions are included in Table 3.1 with specified ice shape, run number, airspeed, mean volumetric droplet diameter, MVD, LWC, total temperature, T_t, static temperature, T_s, and spray time. Ice accretion tests for rime, glaze, streamwise, and horn ice shapes in Figure 3.1(a, b, c, d) were conducted at an angle of attack, α, of 2°. The ice accretion test for the spanwise ridge shape, in Figure 3.1(e), was done at $\alpha = 1°$.

Figure 3.1 shows the (f) lift, C_L, (g) quarter-chord pitching moment, C_M, and (h) wake drag, C_D,

Ice Shape	IRT Run Number	Airspeed (kt)	MVD (μm)	LWC (g/m^3)	T_t ($^\circ F/^\circ C$)	T_s ($^\circ F/^\circ C$)	Spray time (min)
Early-time glaze	ED1974	200	15	0.75	28.0/–2.2	18.5/–7.5	0.5
Early-time rime	ED1983	200	30	0.4	0.0/–17.8	–9.5/–23.1	1.0
Horn	ED1978	200	15	0.75	28.0/–2.2	18.5/–7.5	5
Streamwise	ED1977	200	30	0.4	0.0/–17.8	–9.5/–23.1	5
Spanwise Ridge	ED1967	175	15	0.64	24.0/–4.4	16.8/–8.4	9.5

Table 3.1: Details of the ice accretion parameters for the ice shapes generated in the NASA Glenn IRT [15].

coefficients for the clean and the five ice geometries obtained from the experimental results of [15]. The rime, glaze, streamwise, and horn geometries result in an early onset of stall accompanied by a significant rise in drag and an increased nose-down pitching moment. The spanwise ridge geometry results in a delayed stall angle due to the local energization of the boundary layer generated from a small separation bubble downstream of the ridge [116]. This phenomenon is discussed at length in Section 3.5.6. Similar to the clean airfoil, the rime and spanwise ridge ice geometries have aggressive stall behavior with a sharp decrease in C_L. By contrast, the glaze, horn, and streamwise ice geometries have a shallower stall behavior with an earlier onset of stall. For the two early-time ice geometries, the scales of ice are less than 1% of the chord length, yet they still result in a drastic reduction in the aerodynamic performance. The horn ice geometry yields the largest aerodynamic effect, given its larger and irregular shape, with a region of a nose-up pitching moment at moderate angles of attack ($\alpha \approx 4^\circ - 6^\circ$). Uncertainties in the experimental data are provided for an angle of attack each for the clean and horn ice geometry and is summarized in Tables 3.2 and 3.3. Additional details of the uncertainty analysis are described in [78]. Assuming the relative uncertainty remains approximately constant across all α and geometries, the resulting error bars would be barely visible in Figure 3.1(f) and (h). Due to the higher relative uncertainty in the moment calculation, we would find visible error bars in Figure 3.1(g), but still smaller than the relative difference between the ice shapes. As the uncertainty for the prescribed α values is small, they will be omitted from the figures comparing the experimental data and numerical simulations.

3.3 Characterization of the roughness in the iced geometries

The icing conditions listed in Table 3.1 have implications for the variation in the distribution of the ice displacement height as well as the roughness length scales contained in each shape. In Figure 3.2, displacement heights, h, and roughness length, k, profiles are compared between the early-time rime (a, b, c), streamwise (d, e, f), early-time glaze (g, h, i), and horn (j, k, l) ice shapes. We omit

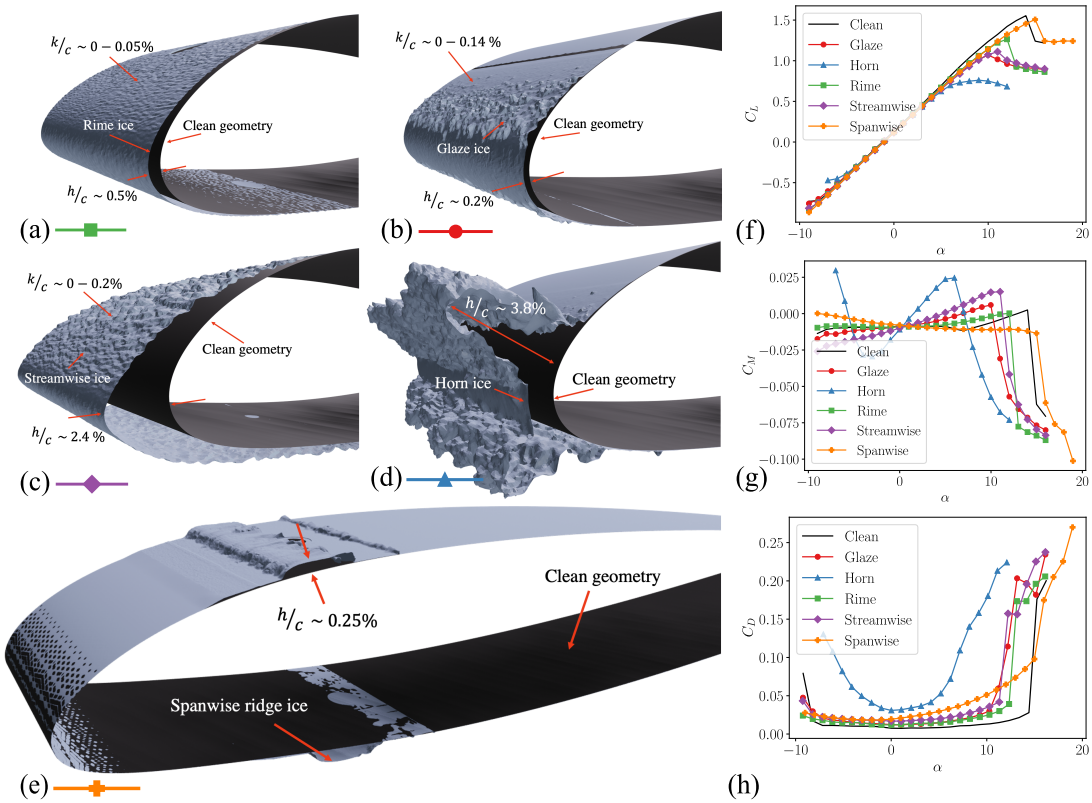

Figure 3.1: Experimental illustration of the geometric changes to the NACA23012 airfoil due to the (a) early-time rime, (b) early-time glaze, (c) streamwise, (d) horn, and (e) spanwise ridge ice accretions on the NACA23012 clean geometry detailing ice scales that geometrically modify the airfoil outer mold line (h) and roughness scales (k). Aerodynamic performance impacts are shown using the integrated quantities of experimental (f) lift (C_L), (g) quarter-chord pitching moment (C_M), and (h) wake drag (C_D) coefficients for the clean, glaze, horn, rime, streamwise, and spanwise ridge ice airfoils from [15]. Note: colors and symbols denoted with each geometry map to the corresponding color and symbol in the integrated force plots (f, g, h).

Aerodynamic quantity	Reference value	Absolute uncertainty	Relative uncertainty
α	4.16°	±0.02°	±0.48%
C_L	0.548	±0.00019	±0.35
C_M	−0.002	±0.00023	±12.1
C_P	−0.962	±0.0045	±0.47
C_D	0.0071	±0.00014	±1.9

Table 3.2: Estimated experimental uncertainty of Broeren *et al.* [15] for the clean NACA23012 geometry at $\alpha = 4.16°$ and $Re_c = 1.8 \times 10^6$.

Aerodynamic quantity	Reference value	Absolute uncertainty	Relative uncertainty
α	6.998°	±0.02°	±0.2858%
C_L	0.7595	±0.00295	±0.389
C_D	0.0935	±0.00407	±0.4518

Table 3.3: Estimated experimental uncertainty of Monastero [78] for the horn-ice geometry at $\alpha = 6.998°$ and $Re_c = 1.8 \times 10^6$.

the spanwise ridge ice shape from this comparison, as most of the roughness features are absent due to the melting of ice from the thermal ice protection system. For modeling purposes, we note that the height of the ridge on both the top and the bottom is approximately 0.25% of the chord across the entire spanwise extent.

Locations of peak h and k are dependent on the type of icing event (i.e. rime or glaze). For example, in both rime ice geometries, a maximum displacement occurs near the stagnation point of the airfoil, which corresponds to $s = 0$, where s is the streamwise coordinate along the airfoil. The peak displacement for the early-time rime and streamwise shapes is $h = 0.0051$ and $h = 0.024$, respectively. Increased icing exposure time results in increased displacement heights. While the displacement increases, the ice profile remains similar between the two geometries. The roughness height also increases due to longer exposure to rime ice conditions. This is clear when comparing Figures 3.2 (c) and (f), where the roughness length scales increase by an order of magnitude between the two ice shapes. This has implications of the resolvability of the rough surfaces as the same resolution level for the streamwise ice shape can provide an order of magnitude higher number of cells per roughness length scale. In both geometries, smooth circular shapes are observed near $s = 0.075$. These are fasteners required to attach the leading edge ice shapes to the rest of the airfoil.

For the early-time glaze ice geometry, the maximum displacement occurs at two locations, $s = -0.023$ and $s = 0.015$. Likewise, the maximum values for the horn ice geometry are located at $s = -0.007$ and $s = 0.014$. The conditions for these two geometries are such that larger droplets

that impact around the stagnation location of the airfoil only partially freeze. The remaining portion of the droplet then runs back along the surface of the airfoil and freezes at a further downstream location. The airfoil leading edge curvature and positive fixed α during the accretion process result in a higher probability of the droplet running back along the suction side of the airfoil. This results in larger horn shapes along the airfoil's upper surface. These horns, both in the early-time and longer-time exposure geometries are critical to capturing the appropriate aerodynamic response. They are geometric features that trigger boundary layer transition in the early-time geometry and geometrically induced separation in the horn ice geometry.

The details of roughness distributions for all four geometries can be seen in Figure 3.2 (c, f, i, l). It can be observed that the rime ice geometries have more regular roughness features, while the glaze ice geometries have concentrated roughness features at two locations. Both scales (h and k) have implications for the aerodynamic effects caused by the roughness. These will be described for each shape in Section 3.5.

In addition to $\overline{|k|}$ (the arithmetic mean about the averaged displacement height), additional moments and roughness parameters can be useful for the description and modeling of rough surfaces. A list and review of all roughness parameters can be found in [28, 62, 65]. It has been shown that at least two or more parameters are required to appropriately characterize the roughness' effect on near-wall turbulent flows [33, 40, 65]. These parameters include the arithmetic mean, root-mean-square roughness height, k_{rms}, effective slope, ES, and skewness, s_k, defined as

$$\overline{|k|}(s) = \frac{1}{S_p} \int |k(s,z)|\, dz \tag{3.2}$$

$$k_{rms}(s) = \sqrt{\frac{1}{S_p} \int k^2(s,z) dz}, \tag{3.3}$$

$$ES(s) = \frac{1}{S_p} \int \left| \frac{\partial k(s,z)}{\partial s} \right| dz, \tag{3.4}$$

and

$$s_k(s) = \frac{1}{k_{rms}^3} \frac{1}{S_p} \int k^3(s,z) dz, \tag{3.5}$$

respectively, where S_p is the spanwise length of the computational domain. These parameters are averaged in the spanwise direction for each ice shape and are a function of the streamwise direction. In Figure 3.3 and 3.4, we plot the values of k_{rms}, ES, and s_k for the rime and glaze ice geometries, respectively. For the early-time rime and streamwise shapes in Figure 3.3, we observe relatively small variation in the streamwise direction for our quantities of interest. The increased values of k_{rms} and the decreased values of s_k between $s = 0.075$ and $s = 0.1$ are attributed to the inclusion of the leading edge fasteners. We observe an increase in both k_{rms} and ES values for streamwise ice compared with the early-time rime due to longer-time rime ice exposure. This indicates that

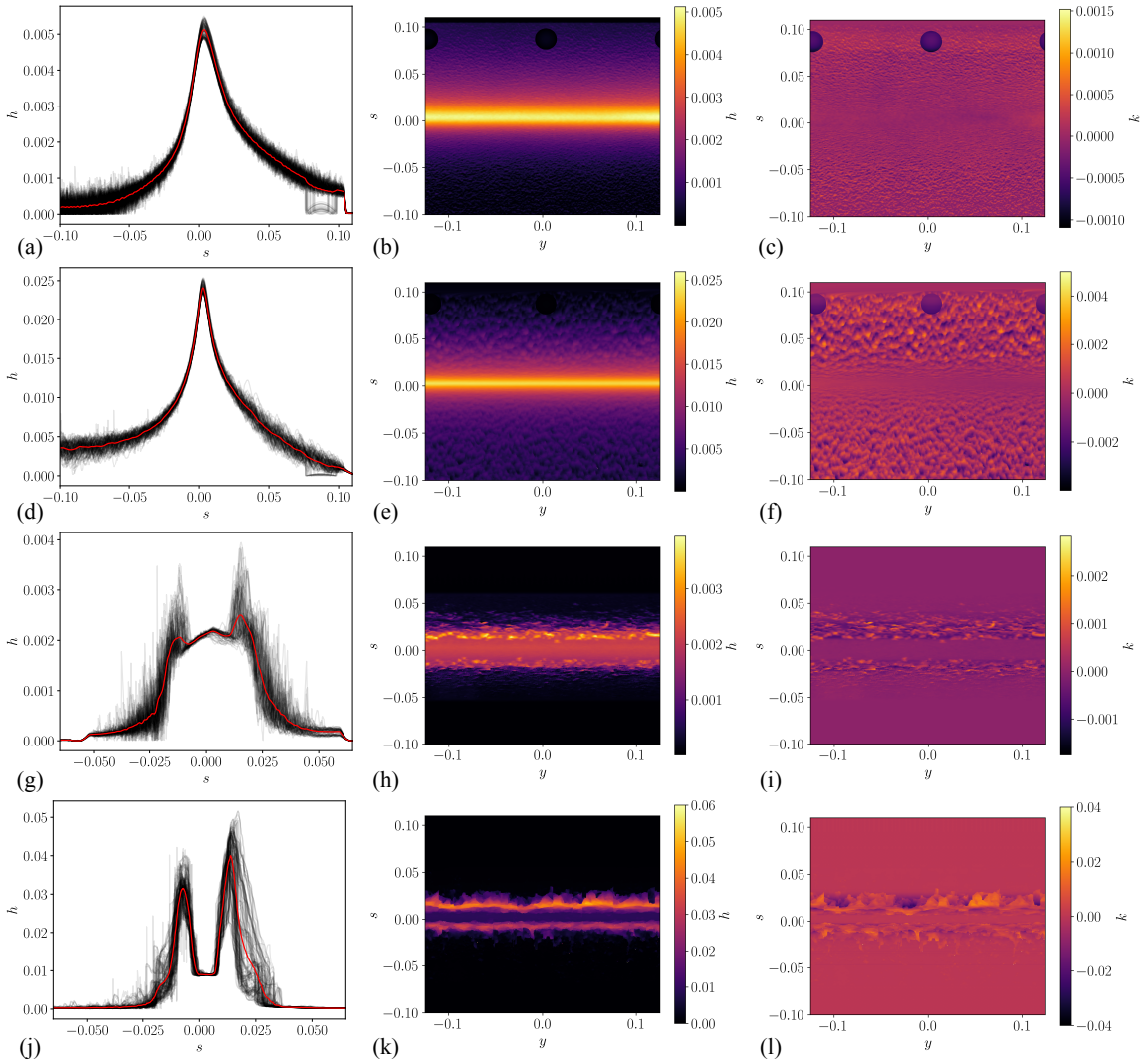

Figure 3.2: Plot of displacement height (h ——) and spanwise averaged displacement height ($\bar{h}$ ——) with respect to s displayed as line plots in (a), (d), (g), and (j). Contour plots of h with respect to spanwise location (y) are displayed in (b), (e), (h), and (k). Roughness heights (k) are displayed in (c), (f), (i), and (l). Each row represents a different ice shape, including early-time rime (a), (b), (c), streamwise (d), (e), (f), early-time glaze (g), (h), (i), and horn (j), (k), and (l). All quantities are normalized by c.

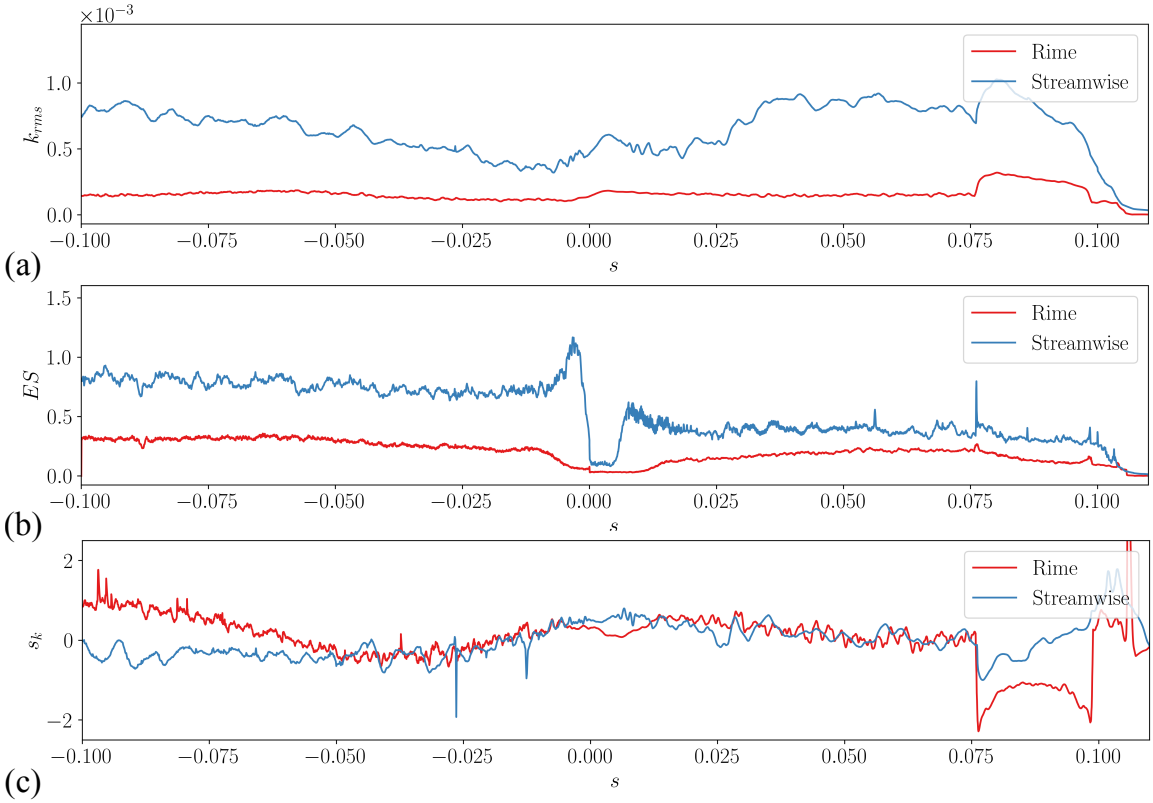

Figure 3.3: Values of (a) k_{rms}, (b) ES, and (c) s_k for the early-time rime and streamwise ice shapes. All values are normalized by c.

the rough structures are becoming steeper and larger with time. Contrarily, the values of s_k remain similar between the shapes. This indicates that the proportion of peaks and valleys in the rough surface is not changing with increased rime ice exposure.

In Figure 3.4, we observe similar trends in k_{rms} and ES for early-time glaze and horn geometries. After increased exposure to glaze icing conditions, we observe an increase in values for both quantities. We also observe a small increase in s_k. Regions of increased s_k for the horn ice geometry are located near regions with spanwise in-homogeneity. Large peaks and valleys occur in the spanwise direction for each streamwise location near the ice horns. This results in large skewness values near the ice horns.

3.4 Computational setup

The cases simulated utilize the NACA23012 two-dimensional airfoil. The flow field is characterized by a free-stream Mach number, M_∞, of 0.18 and a chord-based Reynolds number, Re_c, of 1.8 M. As highlighted in Section 3.2, six geometries are considered in this study; the clean NACA23012

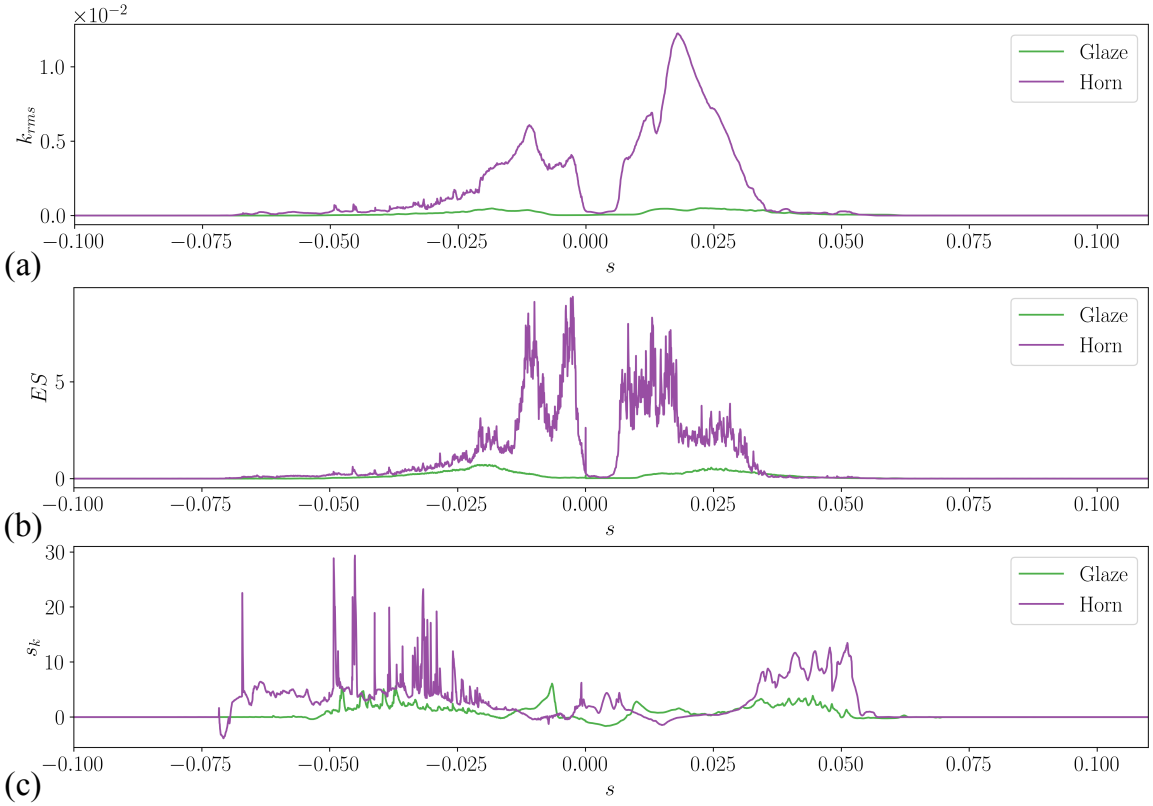

Figure 3.4: Values of (a) k_{rms}, (b) ES, and (c) s_k for the early-time glaze and horn ice shapes. All values are normalized by c.

geometry, two glaze ice geometries (early-time and horn), two rime ice geometries (early-time and streamwise), and the spanwise ridge ice case mimicking SLD conditions with an ice protection system. Hereafter, we refer to the cases as clean, glaze ice, horn ice, rime ice, streamwise ice, and spanwise ridge ice, respectively. A set of angles of attack (α) are simulated by rotating the airfoil about the quarter chord location. The geometries are modeled in a rectangular domain, as shown in Figure 3.5(a), approximately mimicking the wind tunnel effects (see Section 3.7 for additional details on the choice of a rectangular domain). Inflow conditions are specified using free-stream pressure, density, and Mach number ($P_\infty = 101,325$ Pa, $\rho_\infty = 1.225$ kg/m^2, and $M_\infty = 0.18$). No freestream turbulence is supplied at the inflow condition. The outflow boundary is modeled as the non-reflecting characteristic boundary condition [85]. The top and bottom of the domain are modeled using an inviscid wall boundary condition. An algebraic equilibrium wall model is applied at the airfoil surfaces [71]. The spanwise boundaries are treated as periodic conditions. Periodicity is forced on the streamwise, horn, and spanwise ridge ice cases by mirroring a spanwise section of the domain. The clean, rime, and glaze ice geometries do not require mirroring as the deviation in the spanwise boundaries is minimal and periodicity can be enforced. Statistics are gathered throughout the simulation and averaged across at least 20 chord-based flow-through times. Further discussion of the instantaneous force measurements for each ice shape at several angles of attack are outlined in Section 3.8.

Details of the specific spanwise extents, S_p, are outlined in Table 3.4. Only a portion of the ice geometry is used along the spanwise direction for each simulation. The experimental ice accretion test has a span of $0.62c$. For the subsequent wind tunnel tests, this section was copied three times to fit the wind tunnel width, resulting in a total span of $1.86c$ [15]. Including the entire span becomes computationally prohibitive, and therefore, we here choose to simulate only a portion of each geometry along the spanwise direction and assume that the chosen portion is representative of the full ice geometry. To determine the effect of this assumption, we plot the probability density function (PDF) of the magnitude of the roughness length scale, $f_{|k|}(|k|)$, in Figure 3.6 for the selected subsection of the ice shapes and its comparison with the full geometry. The early and long-time exposure to rime ice conditions results in nearly homogeneous spatial distribution in the spanwise direction. Therefore, we see similar PDF profiles for the subset and full geometric representation of the ice in Figure 3.6 (a) and (b). For the glaze ice (early and long-time exposure) geometries [Figure 3.6 (c) and (d)], we observe larger deviations between the full and subset ice geometries, particularly for the long-time exposure case. This is due to the larger spanwise variations observed in horn-ice geometries. To determine sensitivities to this variation, we perform additional spanwise extent studies for both glaze ice geometries (see Table 3.4).

Water-tight geometries of the airfoils are used as the surfaces for generating a Voronoi diagram following the algorithm proposed by [35]. The complex roughness elements present in the ice are resolved using the Voronoi points. This leads to a series of body-fitted unstructured meshes. Figure

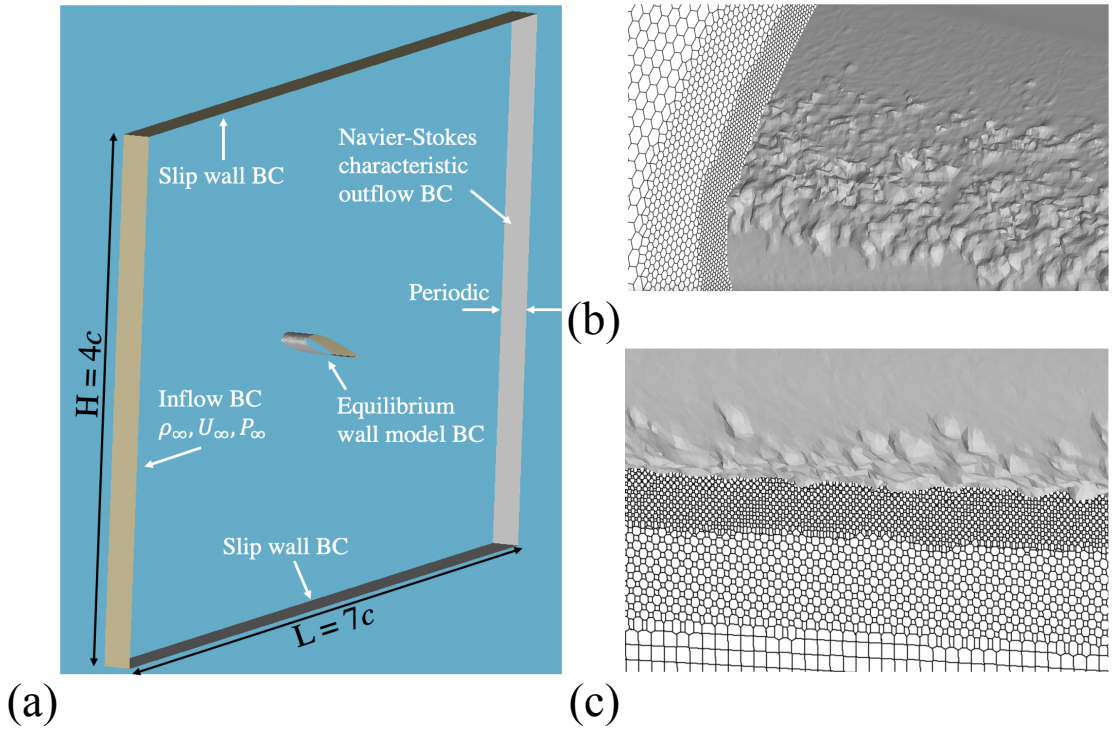

Figure 3.5: (a) Schematic showing the computational domain setup highlighting the inflow boundary condition (BC), outflow BC, equillibrium wall model BC (applied on the airfoil surface), slip wall BC for the top and bottom of the domain, and periodic BC in the spanwise direction. (b,c) HCP element slices highlighting the resolution near rough surfaces: (b) streamwise and (c) spanwise slices. Lengths are defined with respect to the chord length (c).

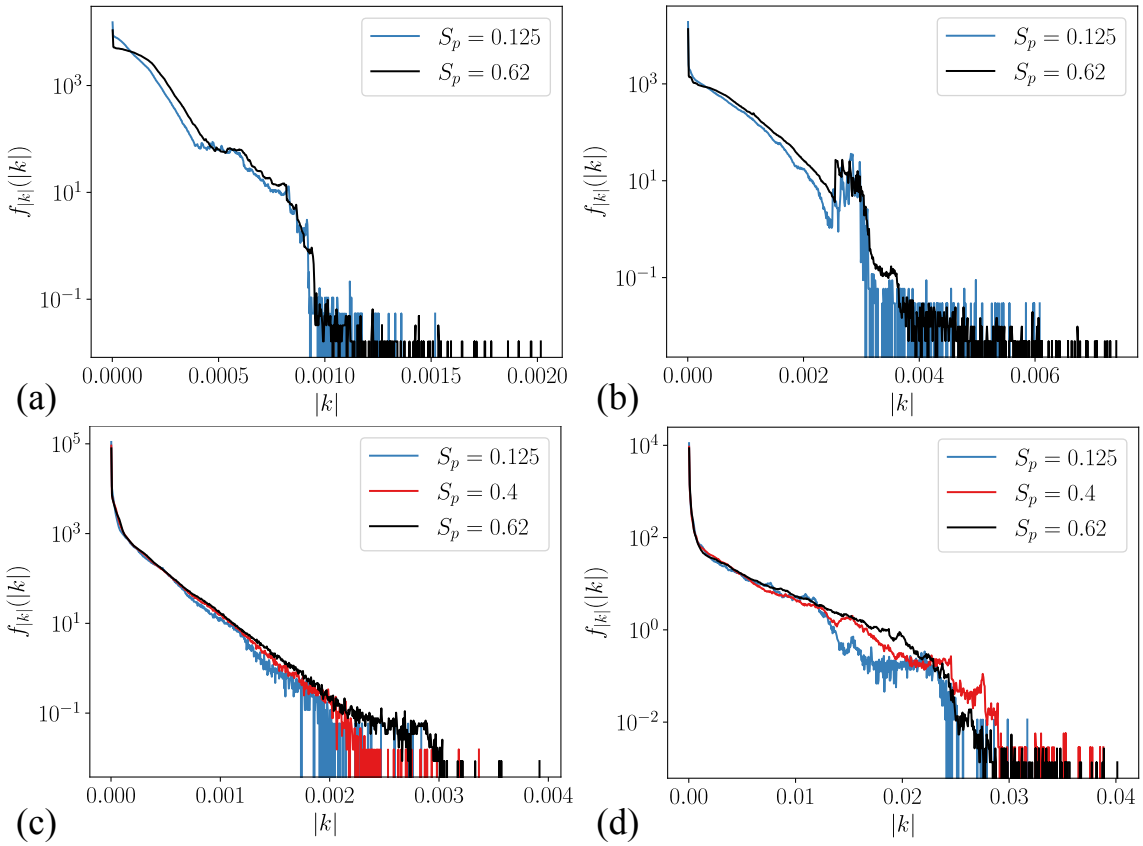

Figure 3.6: Normalized PDF of $|k|$ with simulated spanwise extents (S_p) for the (a) early-time rime, (b) streamwise, (c) early-time glaze, and (d) horn ice shapes. Here, k and S_p are normalized by c.

3.5 (b) and (c) illustrate the ability of the Voronoi points to resolve the complex roughness elements present in the ice. The coarsest grid for the clean ice geometry contains ≈ 1.2 M control volumes (CV). Each successive grid is obtained by homothetically refining the near-wall cells by a factor of two. Each additional layer adds ten cells in the wall-normal direction and isotropically refines the elements in the other two directions. This results in ≈ 4 M CV for the medium clean case, and similarly ≈ 14.25 M CV for the fine, and ≈ 54 M CV for the extra fine cases. Approximate grid cell counts, S_p, number of points per boundary layer height evaluated at 10%, 20%, and 100% of the chord, δ/Δ_{min}, and cells per chord are detailed in Table 3.4. Here, δ is the boundary layer thickness, and Δ_{min} is the minimum grid length scale in the mesh at each evaluated location. An additional level of refinement is added for the first quarter of the chord, as it was observed that leading edge refinement contributed to capturing the correct flow acceleration. This is essential in predicting stall, especially at higher angles of attack [45]. Additional refinement is also applied to all rough surfaces on the airfoil's upper and lower surfaces. Grid refinement studies for each geometry at selected angles of attack are detailed in Section 3.6.

3.5 Computational Results

We compare with the experimental data of [15] in each case. We use the uncorrected force balance measurements for comparison based on a domain size sensitivity study. These simulations showed that the chosen domain is more representative of a wall-bounded wind tunnel rather than a free-air configuration. In addition to force balance measurements, a wake rake determines momentum losses across the airfoil. We include these measurements in the drag coefficient comparisons of Figure 3.7(b) [78]. Previously, [69] used an LBM to simulate the clean, glaze, and horn ice geometries used in the current study. To the best of our knowledge, no other studies consider these ice geometries other than the present work and the LBM results in [69]. Where appropriate, we have included the LBM results in the plots throughout this work. The LBM results utilize a span of approximately $0.63c$ with an applied slip boundary condition to the side walls. The LBM method also utilizes the wall function approach of [38].

3.5.1 NACA23012 clean airfoil

Accurate prediction of lift, drag, and moment coefficients for the clean airfoil geometry are necessary to establish simulation credibility before simulating the airfoil using various ice geometries. In Figure 3.7, aerodynamic coefficients are plotted as a function of the angle of attack for a series of grid resolutions. As the angle of attack increases, the lift coefficient linearly increases while the moment and drag coefficients remain approximately constant, with minor increases nearing the critical stall angle. Around $\alpha = 14^{\circ}$, a sharp decline in lift occurs due to the rapid onset of stall. This is accompanied by a nose-down pitching moment and a rapid rise in drag. We note that the LBM

Ice Shape	Ref. Level	Cell count (M CV)	S_p	$(\delta/\Delta_{min})_{0.1c}$	$(\delta/\Delta_{min})_{0.2c}$	$(\delta/\Delta_{min})_c$	Cells/c
Clean	Coarse	1.2	0.125	2	4	8	780
	Medium	4		4	7	14	1,560
	Fine	14.25		8	13	25	3,125
	Extra fine	54		16	25	40	6,250
Early-time glaze	Coarse	2	0.2	2	4	8	780
	Medium	7.15	0.2	4	7	14	1,560
	Fine	27	0.2	8	13	25	3,125
	Fine	43	0.4	8	13	25	3,125
	Medium	21.23	0.8	4	7	14	1,560
	Fine	85	0.8	8	13	25	3,125
	Extra fine	310	0.8	16	25	40	6,250
	Fine	170	1.6	8	13	25	3,125
Early-time rime	Medium	4.1	0.125	4	7	14	1,560
	Fine	21	0.125	8	13	25	3,125
	Extra fine	109	0.125	16	25	40	6,945
Horn	Fine	33.25	0.25	8	13	25	3,125
	Medium	28	0.8	4	7	14	1,560
	Fine	110	0.8	8	13	25	3,125
	Extra fine	435	0.8	16	25	40	6,250
Streamwise	Medium	8.9	0.25	4	7	14	1,560
	Fine	34		8	13	25	3,125
	Extra fine	134.5		16	25	40	6,250
Spanwise Ridge	Medium	9.5	0.25	4	7	14	1,560
	Fine	37	0.25	8	13	25	3,125
	Extra fine	137.5	0.25	16	25	40	6,250
	Fine	453	1.86	8	13	25	3,125

Table 3.4: Grid refinement details for the different geometries comparing refinement levels; cell counts in millions of control volumes (M CV); chord normalized spanwise extent (S_p); points per boundary layer thickness (δ), where Δ_{min} is the minimum grid length scale; and number of cells per chord. Note: All values of δ/Δ_{min} are evaluated at the denoted chord-based location of the clean ice simulation's boundary layer height.

results do not show the stall that is seen in the experiments of [15]. König *et al.* attribute this to not correctly reproducing a laminar separation bubble at the leading edge of the airfoil [69]. According to Broeren *et al.*, the NACA 23012 airfoil exhibits a leading-edge stall type where the flow abruptly separates due to the bursting of a small leading-edge laminar separation bubble [13]. While the WMLES solution also does not resolve a laminar separation bubble, the results presented here do show stall behavior starting with the medium grid resolution.[2] Upon further refinement, the stall is more representative of the experimental data, albeit not as abrupt. In the linear region of the lift curve, both methods agree with the slope of the lift curve. An extra-fine resolution is simulated at higher angles of attack. Here, the additional refinement leads to a good agreement in the regime just prior to stall. A general improvement is observed compared to the previous LBM results across all quantities. The overprediction of a nose-down pitching moment at finer angles of attack is discussed in Section 3.5.2, relating the phenomenon to spanwise periodic restrictions. For this study, the results of the clean airfoil can be considered acceptable, as they have improved upon previous results in the literature and capture the experimental stall behavior. In the rest of the chapter, unless otherwise stated, we report the fine grid results for the clean case when comparing them to other iced cases. We choose this resolution because it is considered tractable for simulating more complicated configurations of interest, such as swept wings, engine nacelles, and the high-lift common research model, under icing conditions [49]. Additional grid resolution studies for each ice geometry are included in Section 3.6.

3.5.2 Early-time glaze ice geometry

The first ice geometry considered in this work is an early-time glaze ice case, shown in Figure 3.1(b). The glaze ice geometry has a smoother ice section near the leading edge, with roughness elements downstream on both the upper and lower wing surfaces. Prolonged exposure to icing conditions for this geometry leads to ice horns. As stated in Section 3.5.1, we use the fine grid as the benchmark grid resolution. Table 3.4 has a total grid count of 27 M CV for the glaze ice case. Similar to the clean NACA23012 geometry, we compare with the experimental results and the LBM results of [69] in Figure 3.8. Improved results are observed compared to those of [69] for the lift and drag coefficients in the present study. Here, the stall is less pronounced than that of the clean airfoil. A rapid transition can be observed in the comparison of velocity magnitude slices with wall-shear-stress colored surfaces in Figure 3.9. Compared to the smooth streaks in the clean geometry, the glaze ice geometry's large rough elements immediately trigger boundary layer transition (see 3.6). The WMLES results correctly predict the stall angle of attack (after $\alpha = 10^{\circ}$), while the LBM method predicts stall at one degree past the experimental measurement. The stall is less abrupt, with a shallower post-stall C_L slope—the lift coefficient levels off in the post-stall region, which is

[2] In [69], no resolution is reported for the clean geometry. The early-time glaze ice geometry results in ≈ 11 MCV for an equivalent $S_p = 0.2$. This lies between our medium and fine resolutions for the early-time glaze ice geometry.

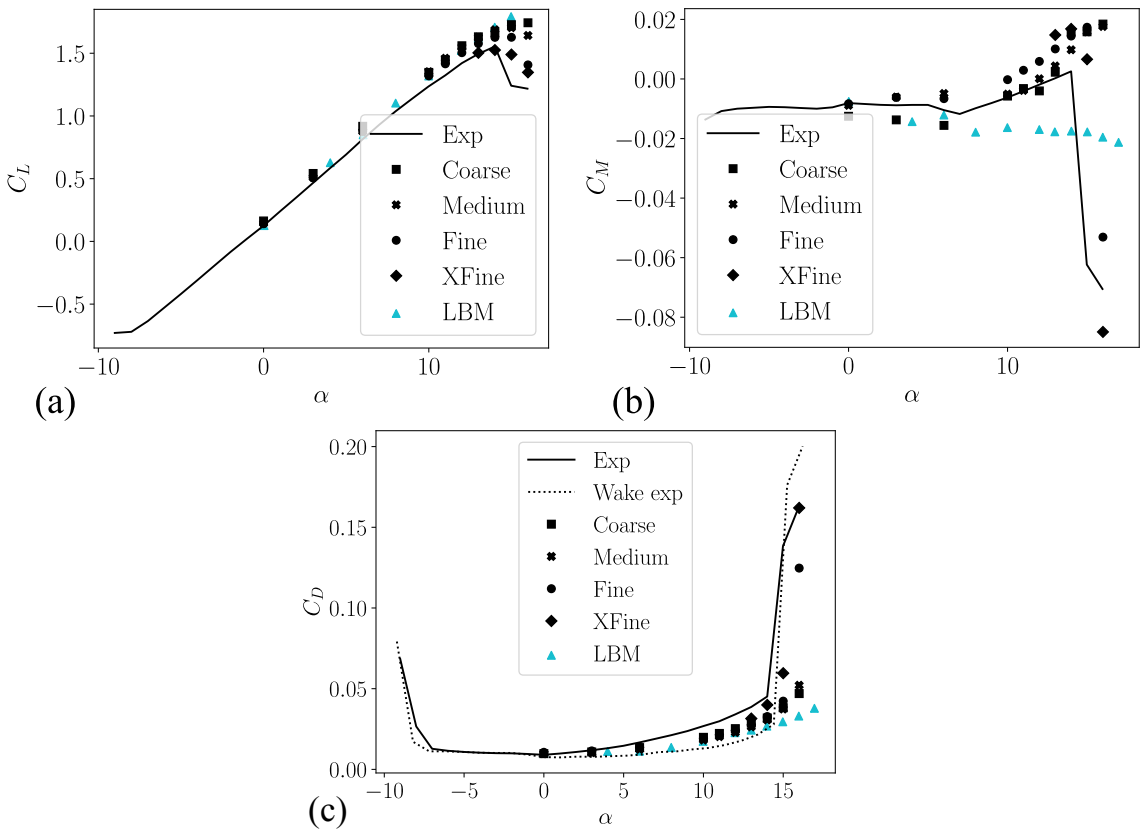

Figure 3.7: Comparing (a) lift (C_L), (b) moment (C_M), (c) and drag (C_D) coefficients of the present WMLES results at three grid resolutions to experimental wake (·····) and force balance (——) measurements [15] as well as LBM results [69] for the clean NACA23012 geometry as a function of angle of attack (α).

also observed in the WMLES results. Figure 3.8(c) compares drag coefficients between the methods. At stall, both the clean and glaze ice geometries undergo a rapid rise in drag due to the onset of separation. The rapid decrease and subsequent increase in drag observed in the experimental wake drag measurements at high angles of attack is due to the experimental uncertainties [15]. This discrepancy was not present in the force balance measurements. In Figure 3.10, spanwise averaged pressure coefficients plotted as a function of x/c, where x is the spatial location along the chord (see Figure 2.1 for reference coordinate), are compared to pressure probes on the glaze ice geometry at four angles of attack. In Figure 3.10(a-b), reasonable agreement is observed between the experimental and WMLES results, leading to less than 10% error in the lift coefficient results. These two cases represent a pre-stall angle, $\alpha = 6°$, and $\alpha = 10°$ corresponding to $C_{L,max}$. At higher angles of attack [Figure 3.10(c-d)], there is an over-prediction of lift generation near the leading edge of the suction side of the airfoil. For $\alpha = 12°$, the C_p values are both underpredicted and overpredicted in different regions, leading to the cancellation of errors, and therefore, a good agreement in the lift coefficient can be seen. Both cases result in a delayed region of adverse pressure gradient near the airfoil's leading edge compared to the experimental result. For $\alpha = 14°$, the pressure recovers to the experimental value around $x/c = 0.5$. A small pocket of lift is seen near $x/c = 0.85$ for Figure 3.10(d). Additionally, the moment coefficients are underpredicted in the post-stall region compared to the experimental results. These discrepancies are due to non-physical domain constraints and are discussed in detail in Section 3.5.2. Generally, we find good agreement between our WMLES calculations and the experimental results.

Spanwise variation

Instantaneous velocity magnitude contours of the resulting flow field as shown in Figure 3.11 indicate the presence of two-dimensional vortical structures. These are believed to be caused by the spanwise restriction imposed by using a periodic domain with a $0.2c$ extent. To investigate this further, we conduct a spanwise extent study for early-time glaze ice case at $\alpha = 9.3^{\circ}, 14^{\circ}$, and 16°. Table 3.4 shows the details of the grids for the spanwise study. Three additional geometries are simulated with a span of $0.4c$, $0.8c$, and $1.6c$.

In Figure 3.12, spanwise conditioned pressure coefficients are plotted for each successively increased spanwise geometry. Minimal changes are observed near the leading edge ($x/c < 0.2$). Around $x/c = 0.85$, a small pocket of lower C_p is observed. This region is indicative of a region of lift that is far from the center of the quarter-chord moment. As the span is increased, this pocket becomes small, indicating that it is an artifact of the spanwise restricted flow field for high angles of attack. Indeed, in Figure 3.13(b), we observe drastic changes in the moment coefficients for high angles of attack. Similar behaviors were noted in the work of Aihara et al., where spanwise variations were considered for a stalled clean airfoil at wall-resolved conditions [4]. They found that the span needed to be at least the same size as the largest length scale in the separation bubble. Increasing the span

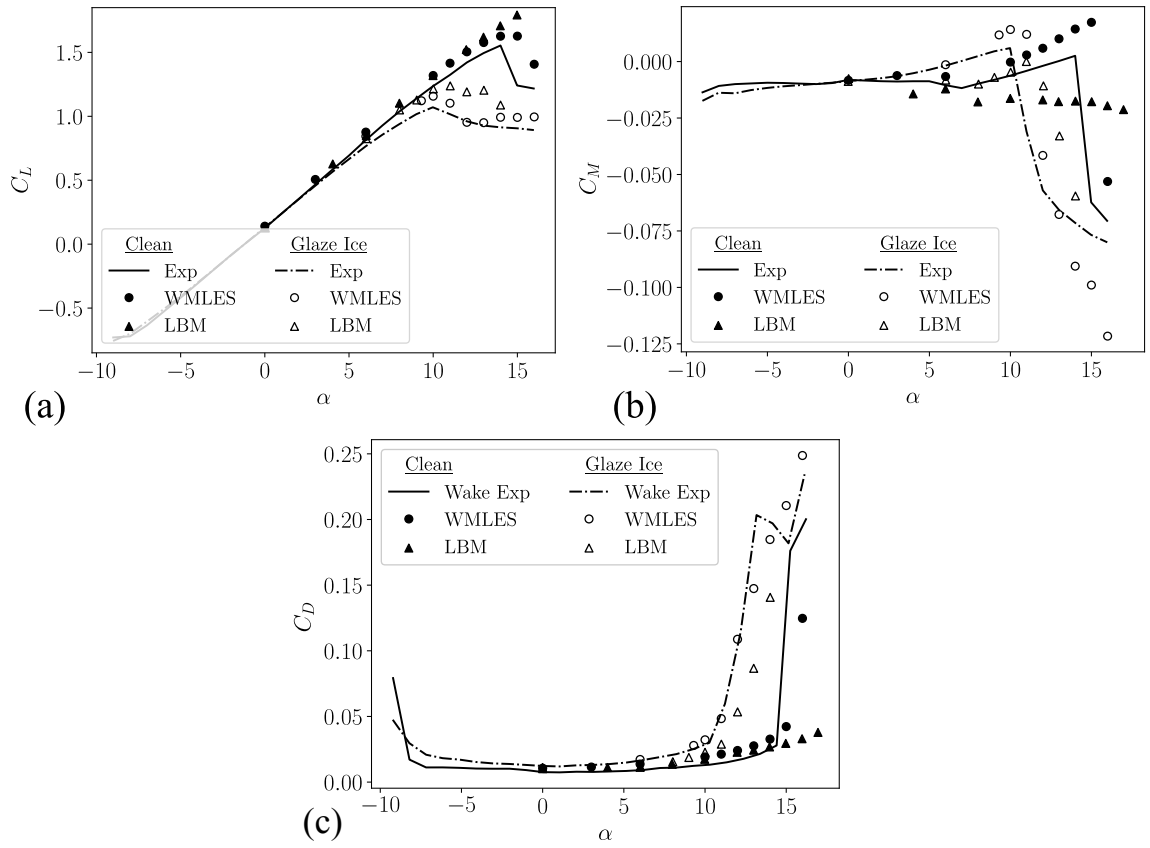

Figure 3.8: (a) Lift (C_L), (b) moment (C_M), and (c) drag (C_D) coefficients comparing the clean (closed symbols, ——) and glaze ice (open symbols, - - -) geometries of the experimental [15], LBM [69], and present WMLES results.

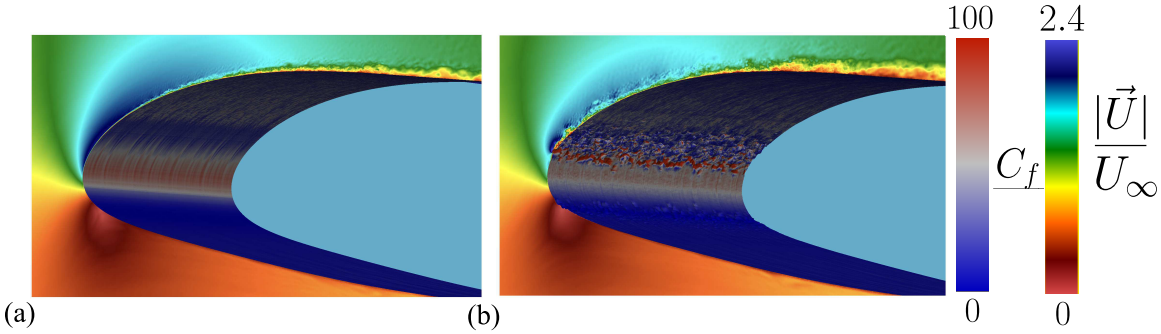

Figure 3.9: Center-line flow-field slice colored by velocity magnitudes with surface plot colored by wall shear stress of (a) NACA23012 clean geometry and (b) early glaze ice geometry, both at $\alpha = 9.3^{\circ}$.

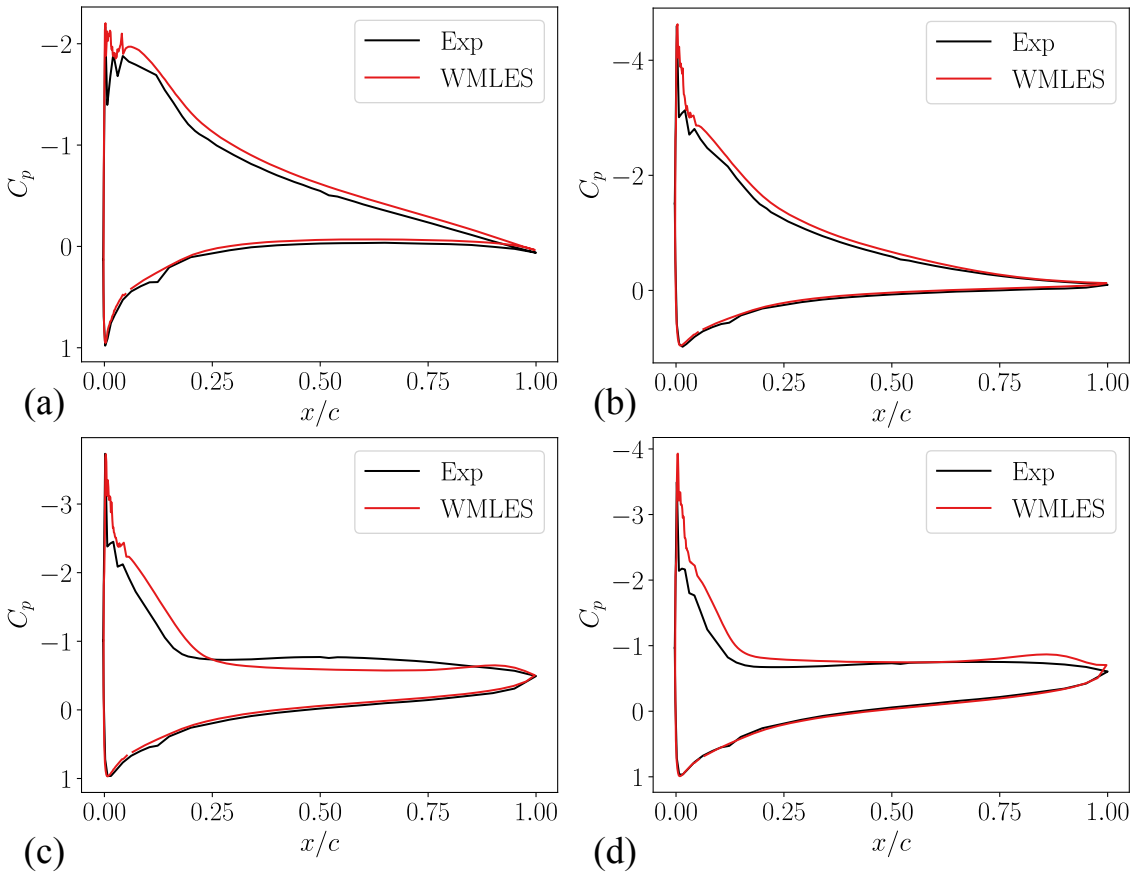

Figure 3.10: Pressure coefficient (C_p) comparison to experimental data for the glaze ice geometry with angles of attack at (a) 6°, (b) 10°, (c) 12°, and (d) 14° [15].

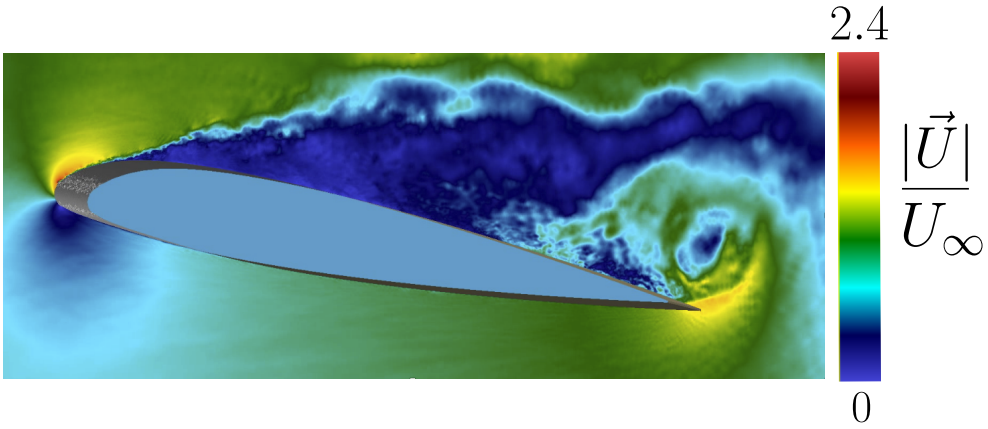

Figure 3.11: Instantaneous center-line flow-field snapshot of velocity magnitude during a sixteen-degree angle of attack ($\alpha = 16^{\circ}$) simulation.

reduces the magnitude of the nose-down pitching moment and brings it closer to the experimental results. In contrast, as the span is increased, minimal changes are observed in the lift coefficients (Figure 3.13(a)). Figure 3.13(c) compares the drag coefficient for each span. At $\alpha = 9.3^{\circ}$, minor sensitivity to the spanwise extent is observed. At higher angles of attack, the drag decreases with an increase in span. A single case with a span of $1.6c$ is run at the highest α. At this spanwise extent, lift remains similar to the $0.8c$ span case while the drag is reduced and the moment is increased. With each successive increase in spanwise extent, additional roughness scales are introduced. While larger span cases include additional changes in geometry, the change in the moment coefficient between successively increased span decreases. Beyond this span, details of the side wall experimental domain would be required. When simulating post-stall angles of attack, selecting a spanwise extent that minimizes errors due to the spanwise domain restrictions is necessary. This is especially necessary for predicting the moment coefficients accurately.

3.5.3 Horn ice geometry

Next, we assess the LES approaches for the horn ice geometry, shown in Figure 3.1(d). In Figure 3.14, the simulated results' lift, moment, and drag coefficients are compared with the experimental and LBM results. We observe good agreement with the experimental data for the horn ice case. Similar results are obtained with the LBM approach. At high angles of attack, we observe overpredicted drag and underpredicted moments. Similar to Section 3.5.2, we run additional cases with higher spanwise extents, here $S_p = 0.8c$. In Figure 3.15, aerodynamic coefficients are assessed with respect to increasing span. Similar to the glaze ice case, increasing the spanwise extent improves the prediction of C_M, reduces C_D (here, closer to the wake drag measurements, and has less effect on C_L). At $\alpha = 10^{\circ}$, C_L becomes worse with additional span. This discrepancy is explained below using the

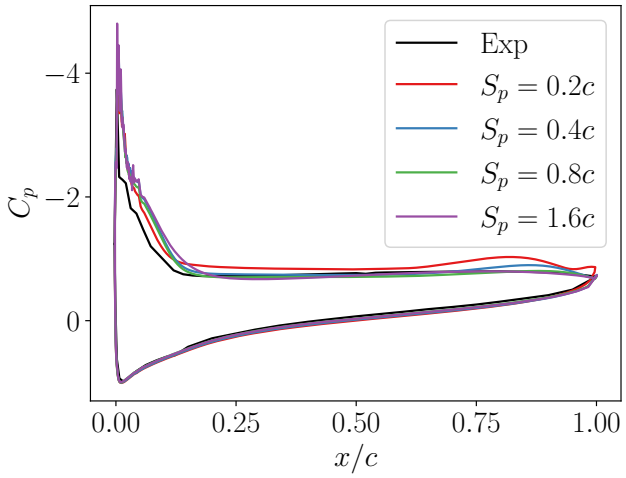

Figure 3.12: Sensitivity of pressure coefficients (C_P) as a function of x/c with increasing span with comparisons to experimental pressure measurements [15].

pressure coefficient data of Figure 3.16. Increasing the span of the horn ice shape also incorporates more of the three-dimensional features of the original laser-scanned airfoil (see Figure 3.6). The introduction of the additional scales with the increase in span can also affect drag and bring it closer to the experimental drag measurements (Figure 3.15(c)).

Pressure coefficients are compared to the experimental data in Figure 3.16 for two angles at pre-stall conditions in Figure 3.16(a-b), one at $C_{L,max}$ in Figure 3.16(c), and one at post-stall in Figure 3.16(d). The spanwise extent is $0.25c$ for (a,b). The effect of spanwise extent for the horn ice geometry is shown in Figure 3.16(c,d). It is observed that the more accurate C_L with the lower span was directly related to cancellation of errors where the leading edge was largely underpredicted and the trailing edge exhibited a pocket of lift similar to the observed effect of Figure 3.12. With appropriate spanwise extents, reasonable agreements are observed across the cases. But at the critical angle of attack, 6°, the region just downstream of the horn ice accretion is overpredicted, indicating a need for additional refinement near the separation locations or the inclusion of geometric features outside the chosen span.

The horn ice case is less challenging for WMLES simulations, but more challenging for constructing body-fitted meshes due to the complex geometric features. In Figure 3.17, an instantaneous center-line slice colored by the velocity magnitudes shows how the flow is immediately separated downstream of the horn ice shape even for a moderate angle of attack ($\alpha = 5^{\circ}$). Wall shear stress contours on the surface highlight the localized value of shear stress at the tips of the ice horns. Flow separation occurs due to the geometric obstruction of the horns, whereas the other geometries, with less ice accretion, have less intrusive separation mechanisms.

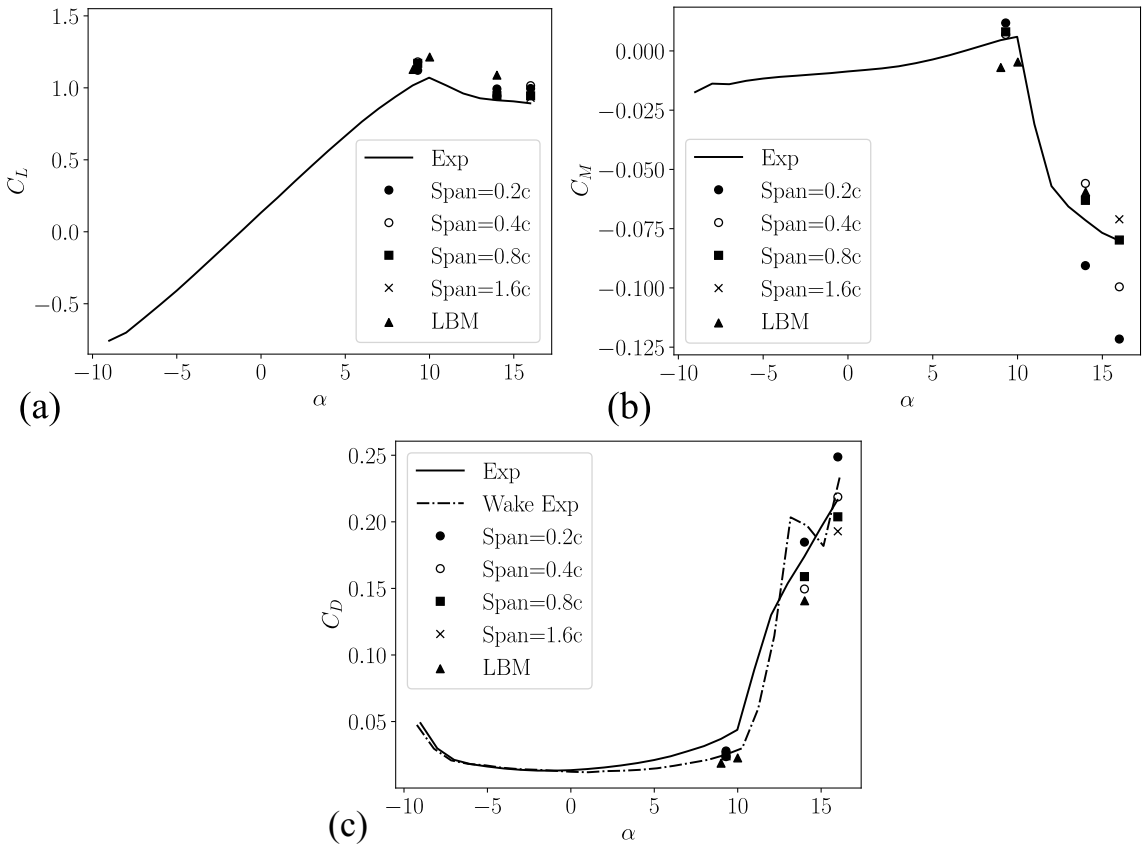

Figure 3.13: Sensitivity of (a) lift (C_L), (b) moment (C_M), and (c) drag (C_D) coefficients for the glaze ice geometry with increasing span with comparisons to experimental wake (-···-) and force balance (——) measurements [15] as well as LBM simulations [69].

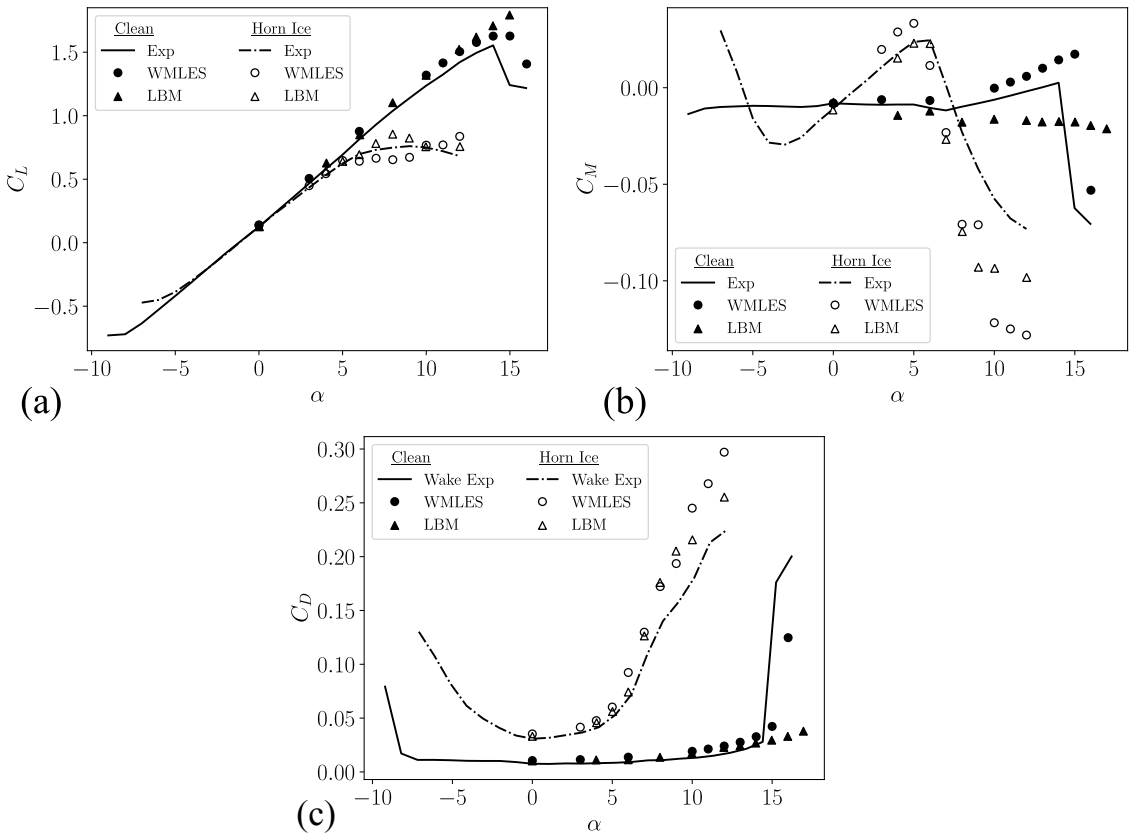

Figure 3.14: (a) Lift (C_L), (b) moment (C_M), and (c) drag (C_D) coefficients comparing the clean (closed symbols, ——) and horn ice (open symbols, -···-) geometries of the experimental [15], LBM [69], and present WMLES results.

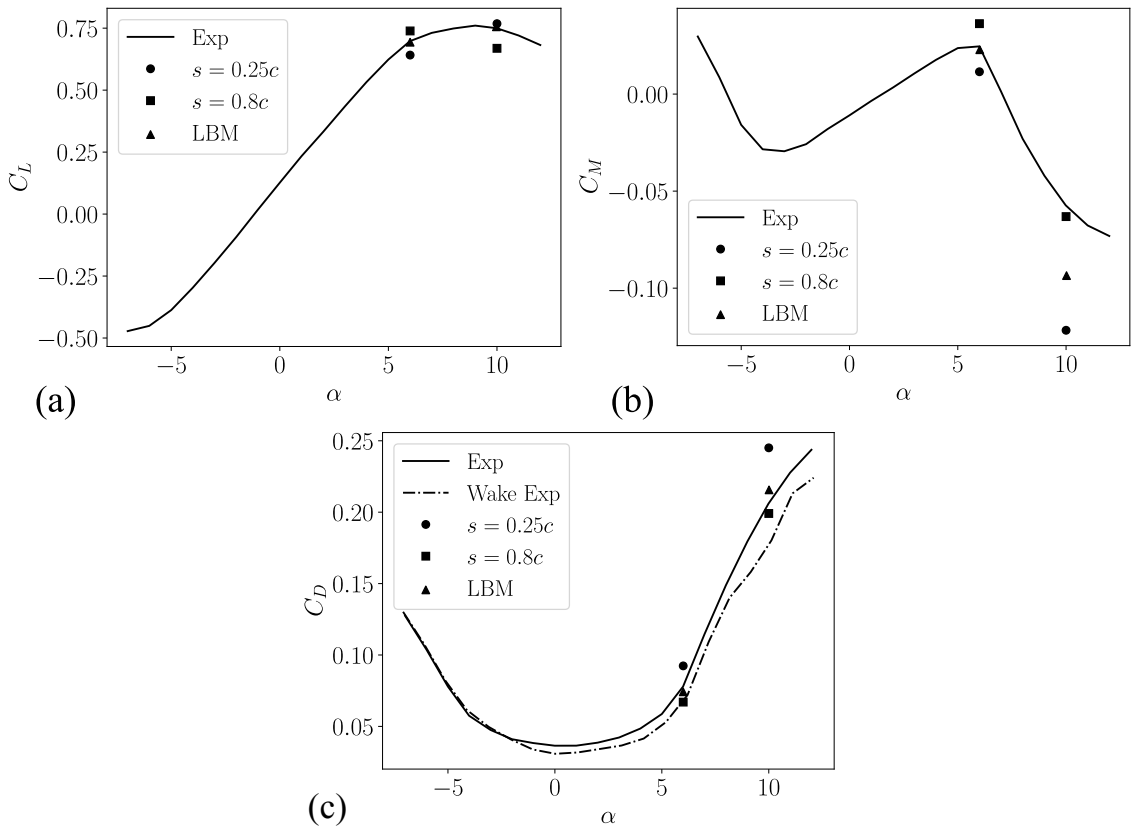

Figure 3.15: Sensitivity of (a) lift (C_L), (b) moment (C_M), and (c) drag (C_D) coefficients for the horn ice geometry with increasing span with comparisons to experimental wake (-···-) and force balance (——) measurements [15] as well as LBM simulations [69].

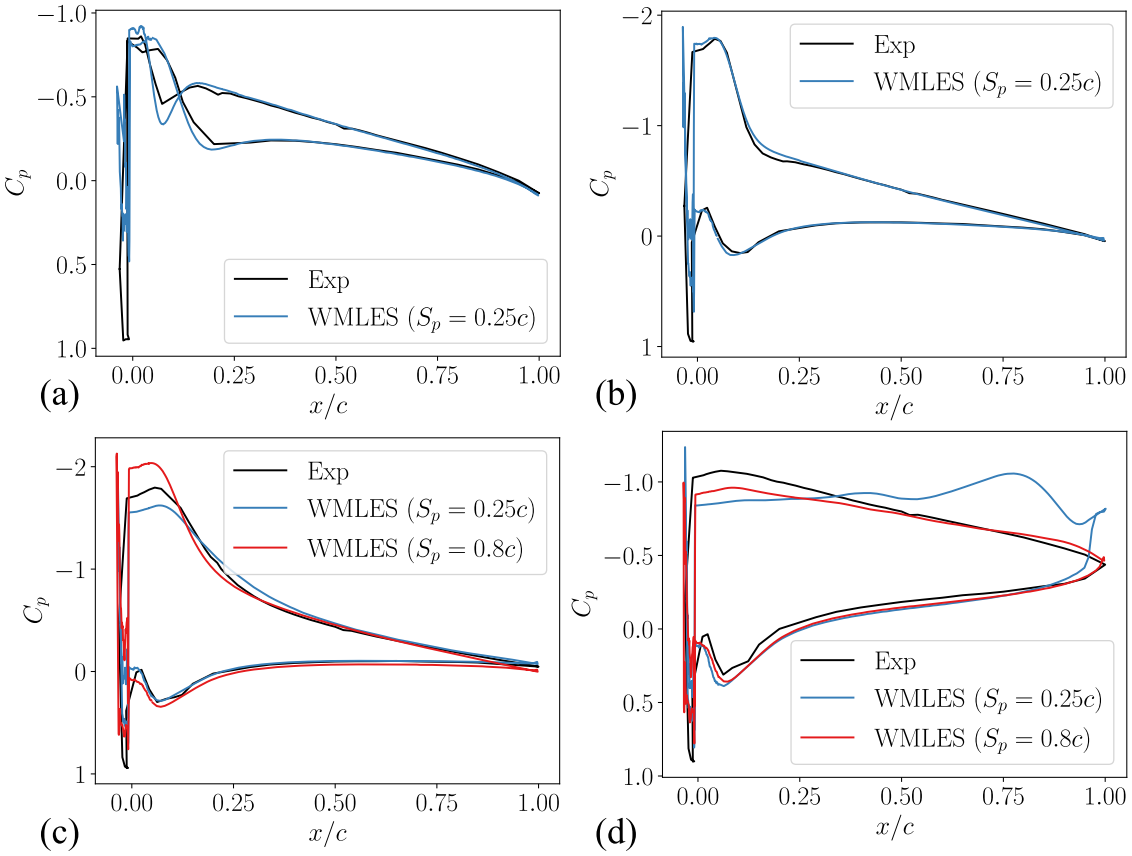

Figure 3.16: Pressure coefficient (C_p) comparison to experimental data for the horn ice geometry with angles of attack (and span) at (a) 0° ($S_p = 0.25c$), (b) 4° ($S_p = 0.25c$), (c) 6° ($S_p = 0.25c$ and $S_p = 0.8c$), and (d) 10° ($S_p = 0.25c$ and $S_p = 0.8c$) [15].

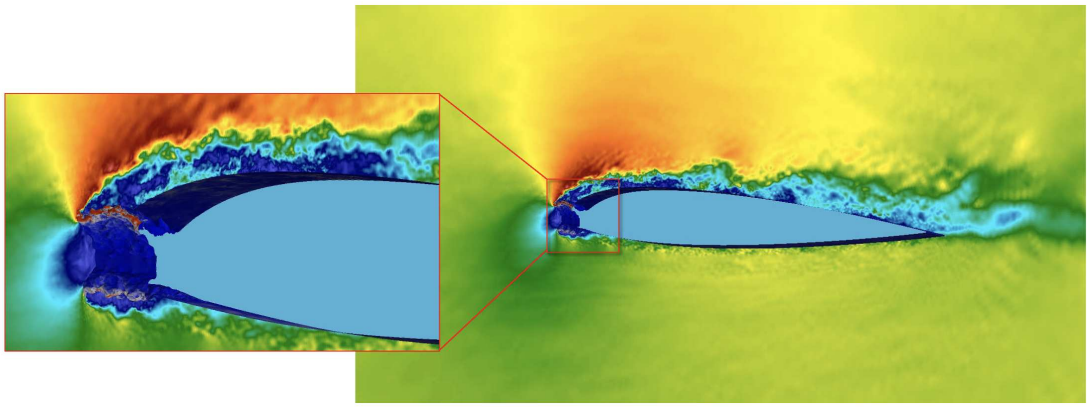

Figure 3.17: Center-line flow-field slice colored by velocity magnitudes with surface plot colored by wall shear stress of the NACA23012 airfoil at $\alpha = 5^{\circ}$ with horn ice. Inset focuses on the leading edge of the airfoil, highlighting the high shear stress near the tips of each horn.

3.5.4 Early-time rime ice geometry

The third geometry simulated is the early-time rime ice geometry, shown in Figure 3.1(a). Unlike the glaze ice geometry, the roughness is distributed evenly across the upper and lower surfaces of the NACA23012 airfoil. We apply the established practices from the glaze ice simulations (Section 3.5.2) to the rime ice geometry. To the best of our knowledge, these are the first-ever simulations of a laser-scanned rime ice geometry.

In Figure 3.18, lift, drag, and moment coefficients are compared with the experimental data. Contrary to the glaze ice case, the rime ice case does not predict the correct change in lift and drag. The maximum lift and critical stall angle are both overpredicted. The delayed separation can also be observed when comparing the wake drag measurements to the simulated results. These mispredictions are due to the under-resolved roughness scales near the leading edge. The maximum roughness height, as a percentage of chord length, is approximately 0.03% for the rime ice geometry. This results in about 1.5 control volumes per maximum roughness height; hence, all the roughness scales are in the sub-grid scale regime.

This is further emphasized in Figure 3.19, where pressure coefficients are compared to the experimental data for two angles at pre-stall conditions in Figure 3.19(a-b), one at $C_{L,max}$ in Figure 3.19(c), and one at post-stall in Figure 3.19(d). Here, minor overpredictions of C_p lead to larger overshoots for C_L (a-c). For the post-stall angle, we observe a large overprediction of C_p on the suction side of the airfoil near the leading edge. A small separation event occurs near the trailing edge of the airfoil. For this angle of attack, the experimental observation is that the flow over the airfoil is fully separated.

In Figure 3.20, we refine the grid to an additional level (equivalent to the extra fine clean airfoil simulation) for three angles of attack (one at $C_{L,max}$ and two in the post stall region). It can be observed that predictions of the lift, drag, and moment coefficients improve with respect to the experimental data. Additionally, in Figure 3.21, we plot pressure coefficients for $\alpha = 12^\circ$ (a) and $\alpha = 13^\circ$ (a) compared to experimental pressure coefficients for two grid resolutions (fine and extra fine). At the critical angle of attack, small reduction in C_p, with grid refinement, at the leading edge lead to a better prediction of $C_{L,max}$ (as seen in Figure 3.20). In the post-stall angles, we observe only minor improved results as compared to the experimental data, but it is clear that additional refinement is required to accurately capture the stall event.

There are approximately 3 control volumes per maximum roughness height at this extra-fine resolution. For the methods used in this work, the recommended number of points per roughness height is at least 4 [46, 63] to resolve the roughness features. Here, we are beginning to resolve the roughness scales, but further refinement is required to resolve all the scales appropriately. These refinement regimes begin to approach wall-resolved resolutions, limiting their utility in engineering applications.

In Figure 3.22, we compare the qualitative features of the flow field for the fine case [Figure

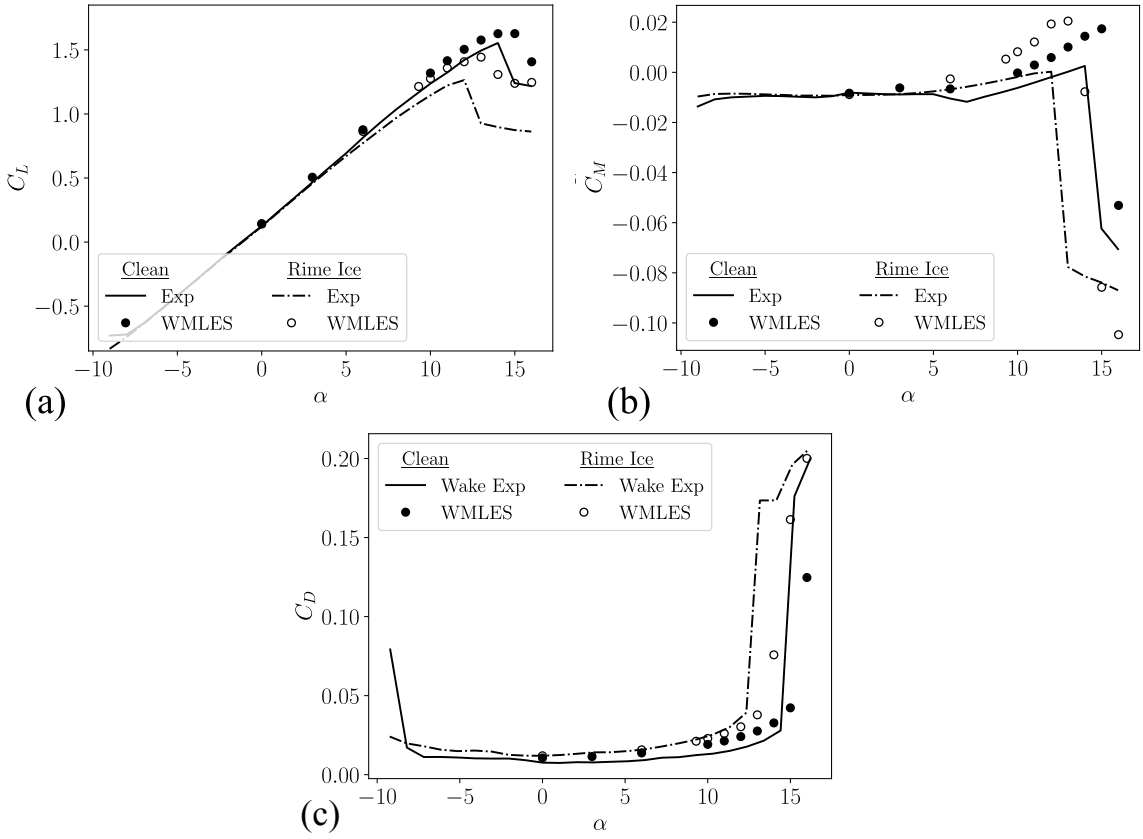

Figure 3.18: (a) Lift (C_L), (b) moment (C_M), and (c) drag (C_D) coefficients comparing the clean (closed symbols, ——) and rime ice (open symbols, -·-·-) geometries of the experimental [15] and present WMLES results.

3.22(a)] and the extra fine case [Figure 3.22(b)]. Comparing the two results highlights that the roughness elements are completely sub-grid for the fine-grid simulations. For the fine case, we observe a flow field qualitatively similar to those observed in the clean geometry. In contrast, for the extra fine case, regions of increased wall shear stress can be observed in the regions with rime ice roughness. The additional refinement required to capture the roughness elements becomes intractable when simulating a wing or complete aircraft under similar resolutions. Therefore, these results highlight the need for roughness wall models in rime ice conditions.

3.5.5 Streamwise ice geometry

The streamwise ice geometry, shown in Figure 3.1(c), is the resulting shape from a five-minute exposure to rime ice conditions (see Table 3.1). Small droplets accrete at the leading edge geometry

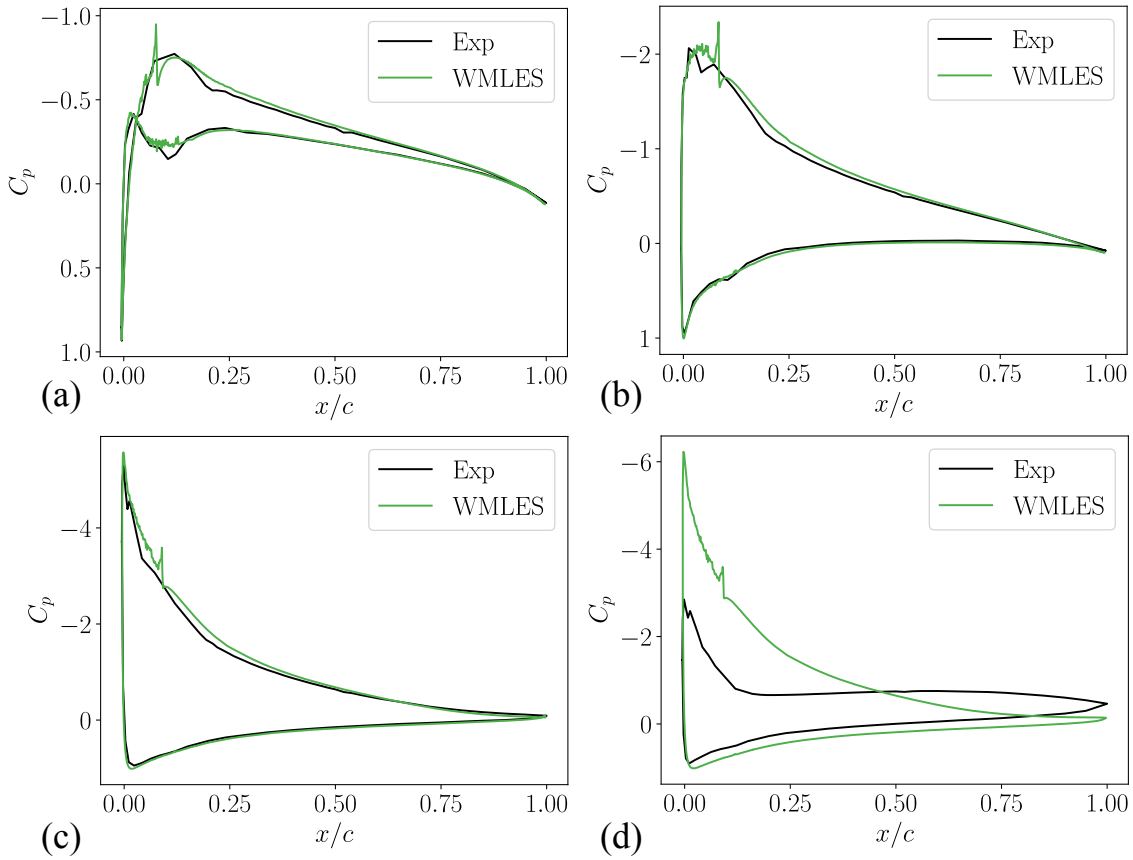

Figure 3.19: Pressure coefficient (C_p) comparison to experimental data for the rime ice geometry with angles of attack at (a) 0°, (b) 6°, (c) 12°, and (d) 13° [15].

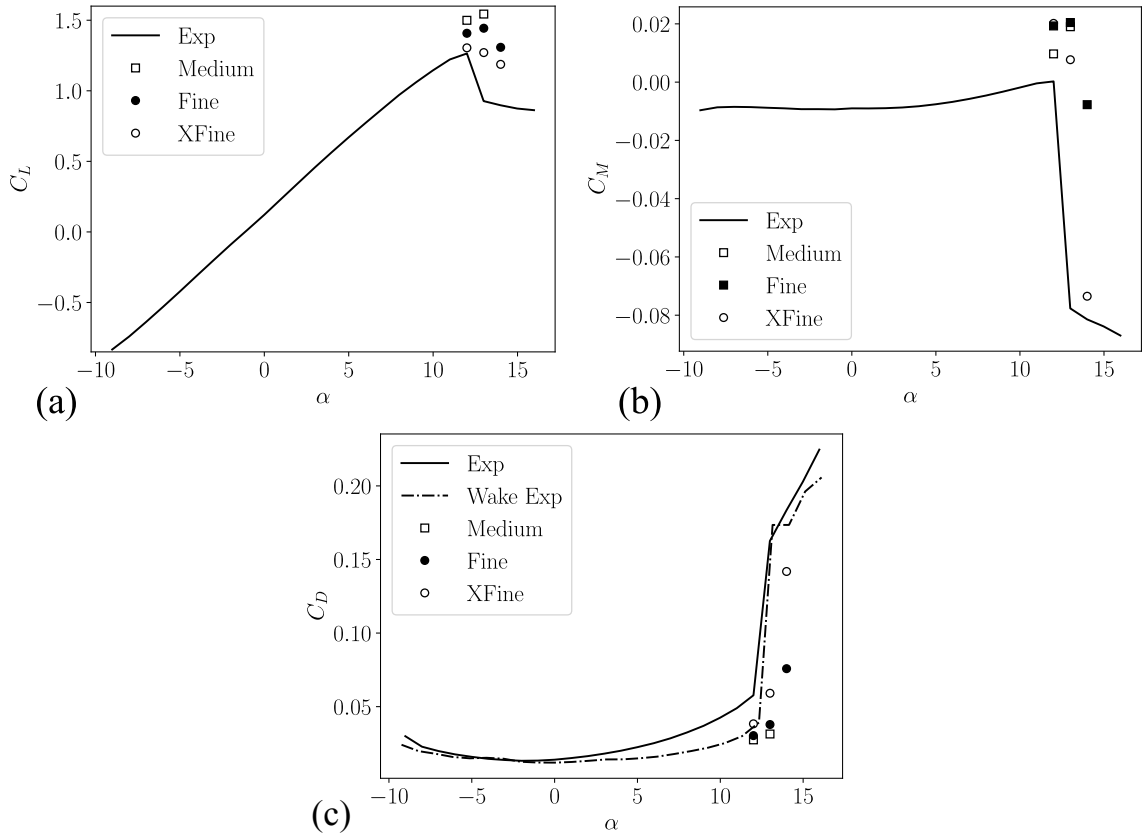

Figure 3.20: Sensitivity of (a) lift (C_L), (b) moment (C_M), and (c) drag (C_D) coefficients for the rime ice geometry with increasing grid resolution with comparisons to experimental wake (-···-) and force balance (——) measurements [15].

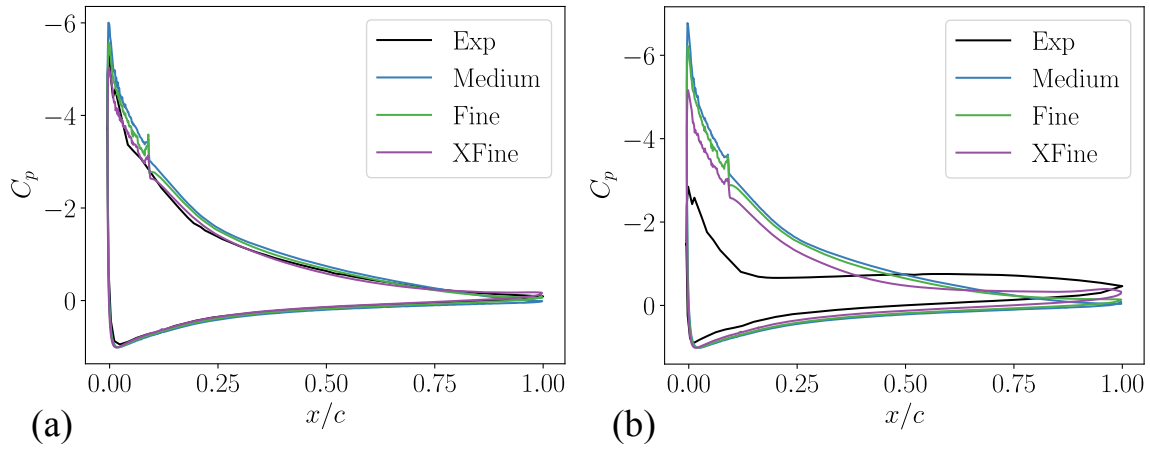

Figure 3.21: Sensitivity of pressure coefficients (C_p) for the rime ice geometry with increasing grid resolution with comparisons to experimental pressure measurements with angles of attack at (a) 12° and (b) 13° [15].

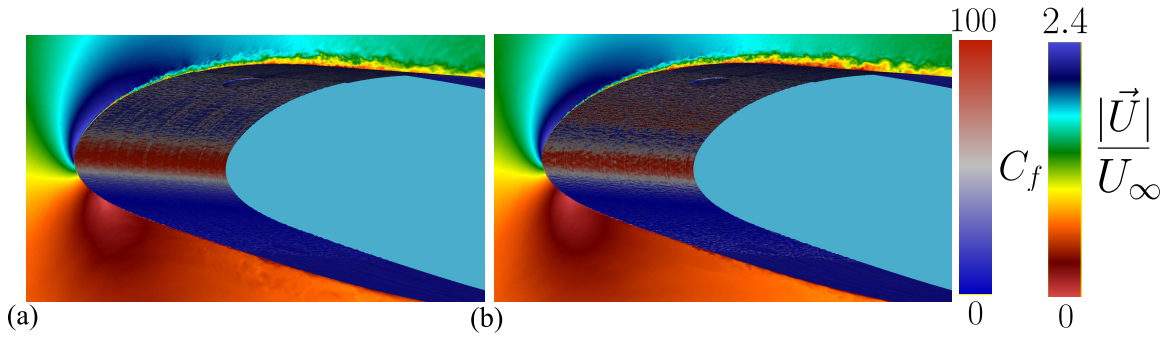

Figure 3.22: Center-line flow-field slice colored by velocity magnitudes with surface plot colored by wall friction coefficient of (a) fine and (b) extra-fine rime ice geometry at $\alpha = 12^{\circ}$.

and freeze before any run back can occur. This freezing process leads to so-called spear-like geometries where the blunt leading edge of the airfoil becomes sharper. Similar to the early-time rime ice shape, the roughness elements are distributed more uniformly across the leading edge of the airfoil. The roughness scales reach 2-4 times the size of the early-time rime ice geometry. This increases the number of grid points across a given roughness element. Small roughness elements close to the leading edge will still be highly under-resolved.

In Figure 3.23, lift, drag, and moment coefficients are compared to the experimental data. In the region prior to stall (here $\alpha \approx 11°$), both lift and drag coefficients have good agreement with the experimental results. In the post-stall region, the lift coefficient follows the downward slope of the experiment, which has a less abrupt stall behavior than the rime ice geometry. While the chosen grid resolution resolves the macroscopic effects of lift and drag (i.e., critical stall angle and $C_{L,max}$), it is still not sufficient to resolve many of the roughness scales which results in lower drag coefficient for post-stall angles. Pressure coefficients at four angles of attack are shown in Figure 3.24. We observe good agreement with the experimental measurements up to $\alpha = 11°$, which is representative of the location of $C_{L,max}$ for these conditions. In Figure 3.24(d), cancellation of errors between the leading edge and trailing edge pressure distribution explain our reasonable agreement with C_L, but overprediction of C_M in Figure 3.23(a). Additional resolution using the full span of the ice shape may be necessary to remove the errors in drag at the post-stall angles of attack.

3.5.6 Spanwise ridge ice geometry

The final ice shape we consider is the spanwise ridge geometry. This geometry mimics the use of a thermal-based icing protection system (IPS) for the leading edge of a wing. Specifically, the icing conditions and heater settings were determined to induce run-back of the water past the IPS. The inclusion of the IPS makes this geometry unique from the other four. This can be seen in Figure 3.1(e), which shows the outer mold line of the spanwise ridge shape. The leading edge is identical to the clean NACA23012 geometry, and at some distance downstream, just past the IPS, a prominent ridge of ice is formed [14]. For this Re_c, the primary adverse effect of the ridge is a significant increase in drag. The maximum lift coefficient differs by only 3-tenths of a lift coefficient compared to the clean geometry. Additionally, the stall is delayed by approximately 2°. According to [14], at increased Re_c, the spanwise ridge shape would result in much lower values of α_{crit} and $C_{L,max}$.

In Figure 3.25, we compare the integrated aerodynamic coefficients to the experimental data. We observe a delayed stall (higher critical α) for the spanwise ridge ice shape, similar to the experimental results. In contrast to the experiment, the critical angle of attack in the simulations occurs at approximately $1° - 2°$ larger than the experimental result. This shift is also observed in C_M. We overpredict the critical angle of attack for the fully clean geometry by approximately $1° - 2°$ as well. For both the clean and spanwise ice shape, the airfoil's leading edge is the same. In this region, we encounter turbulence transition and high-pressure gradients that stress the assumptions of the

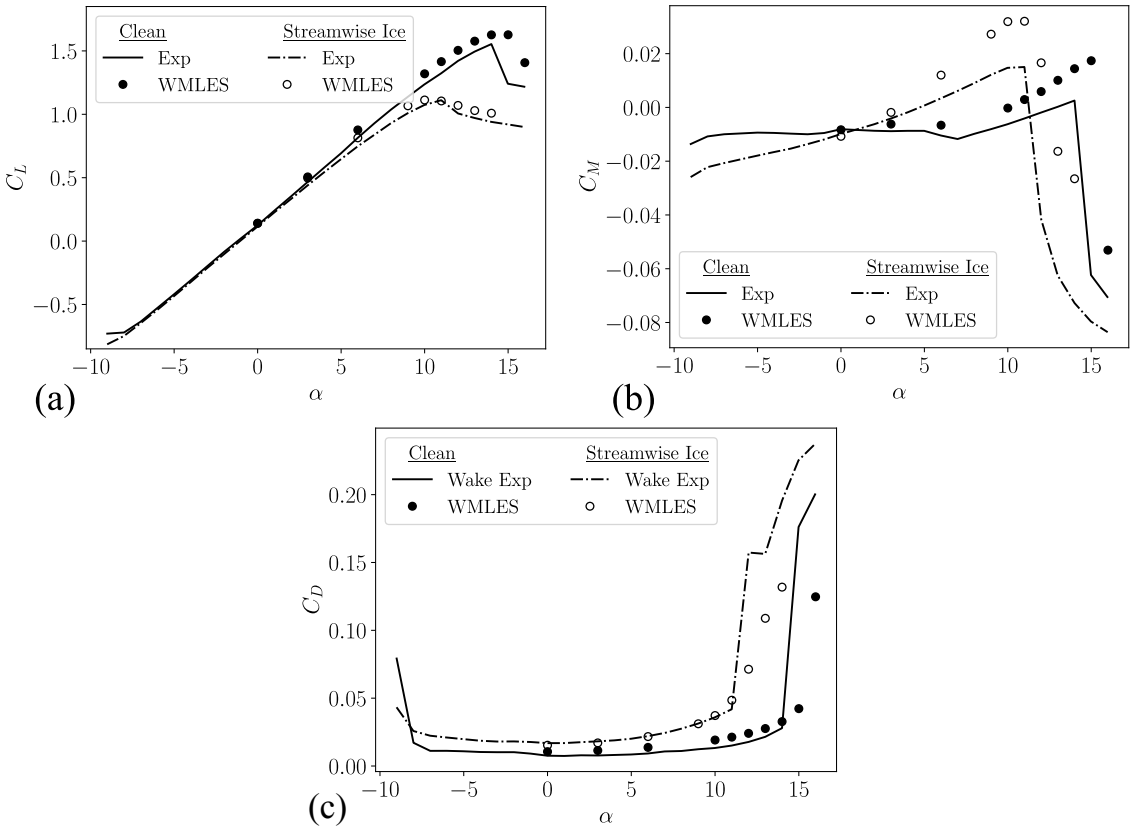

Figure 3.23: (a) Lift (C_L), (b) moment (C_M), and (c) drag (C_D) coefficients comparing the clean (closed symbols, ——) and streamwise ice (open symbols, -···-) geometries of the experimental [15] and present WMLES results.

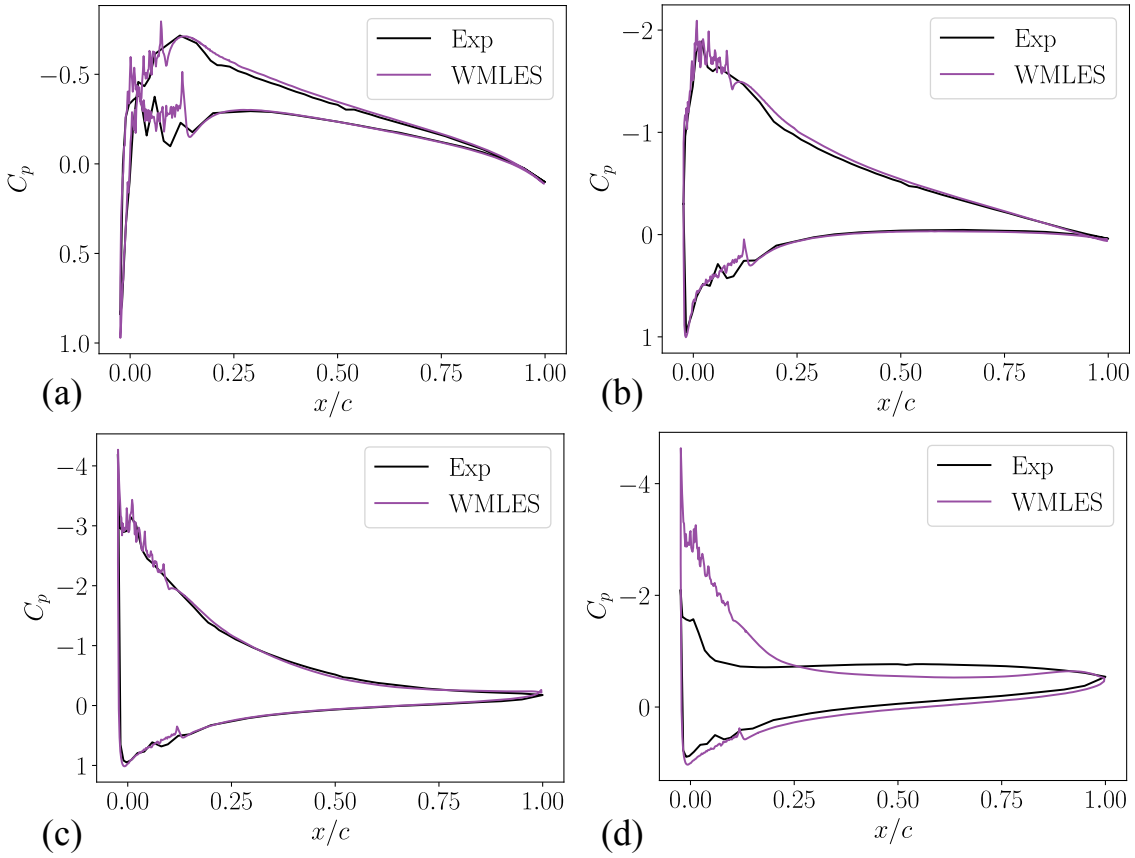

Figure 3.24: Pressure coefficient (C_p) comparison to experimental data for the streamwise ice geometry with angles of attack at (a) 0°, (b) 6°, (c) 11°, and (d) 14° [15].

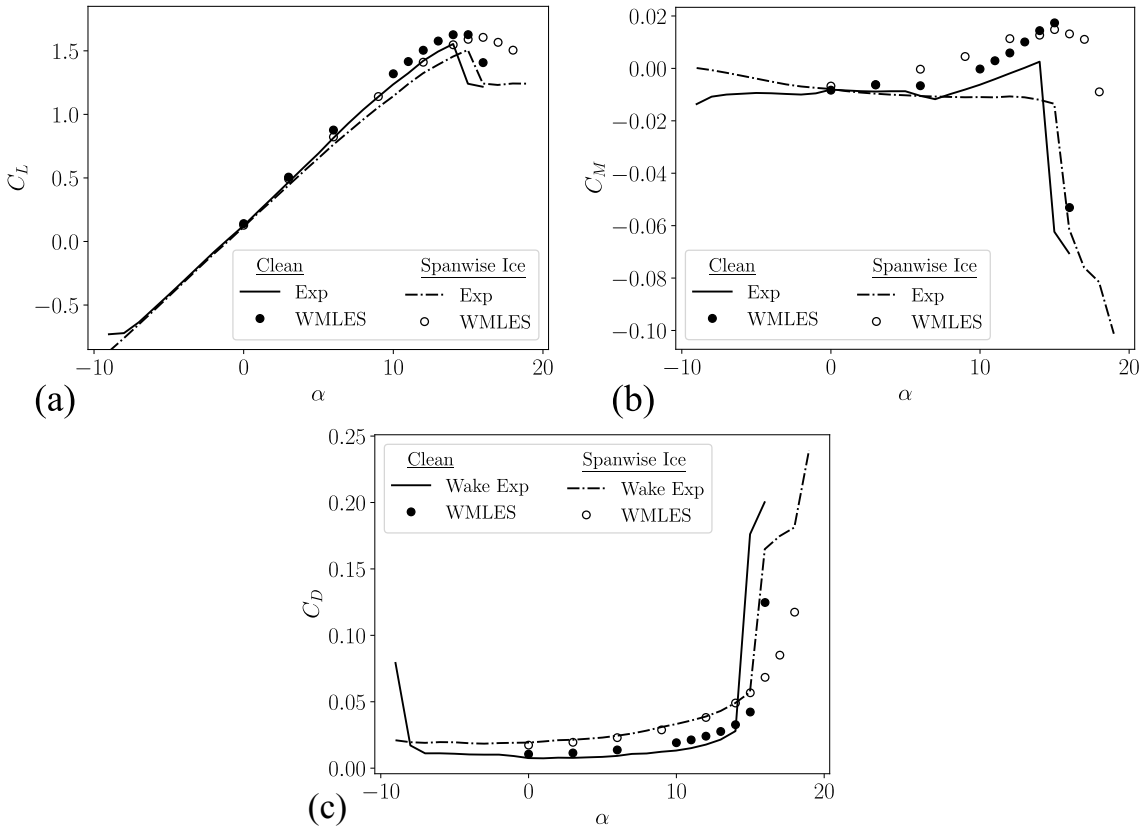

Figure 3.25: (a) Lift (C_L), (b) moment (C_M), and (c) drag (C_D) coefficients comparing the clean (closed symbols, ——) and spanwise ridge ice (open symbols, -···-) geometries of the experimental [15] and present WMLES results.

equilibrium wall model. Figure 3.25(c) shows the increased drag due to the ice shape. We observe good agreement with the wake drag measurements prior to stall. The wake drag in the post-stall region ($\alpha \approx 18°$) is underpredicted and the lift is overpredicted. The simulation in the post-stall region would benefit from additional spanwise representation of the surface, shown in Section 3.5.6. Pressure coefficients for $\alpha = 0°, 6°, 12°$, and $18°$ are plotted in Figure 3.26. Before stall, we find good agreement between the experimental and WMLES results. At the location of the ridge, an increase in pressure is observed, followed by a geometrically induced flow separation just downstream of the ridge line. This small separation bubble locally energizes the boundary layer, causing it to remain attached at higher angles than the fully clean case [116].

Wind tunnel effects

At high angles of attack, we observe an under prediction of drag and an overprediction of both the lift and moment coefficients. Based on the results of Section 3.5.2, we choose to conduct an

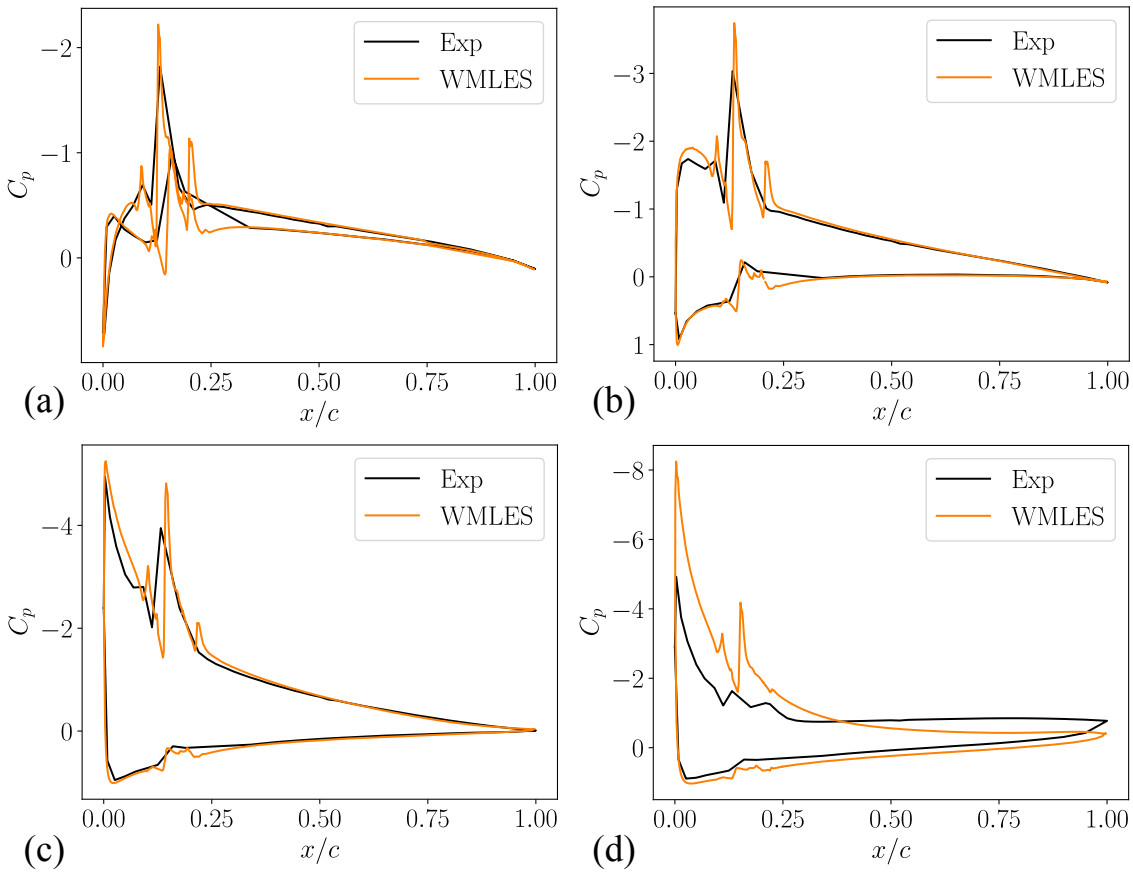

Figure 3.26: Pressure coefficient (C_p) comparison to experimental data for the spanwise ridge ice geometry with angles of attack at (a) 0°, (b) 6°, (c) 12°, and (d) 18° [15].

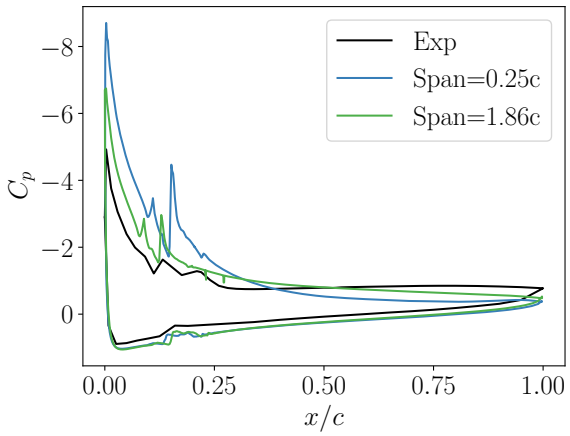

Figure 3.27: Pressure coefficient (C_p) comparison to experimental data for the spanwise ridge ice geometry at $\alpha = 18^\circ$ with changing spanwise extent [15].

additional spanwise extent study of the spanwise ridge ice geometry with the full dimensions of the wind tunnel. This results in $S_p = 1.86c$ where we apply a slip wall condition to both side walls. In Figure 3.27, pressure coefficients are compared between a reduced span and full span with wind tunnel side walls. We observe closer agreement with the experimental data as compared with the reduced span, but still observe overprediction of the leading edge suction. The percent error in lift dropped from 16.3% to 7.6% while the drag error decreased from 38.2% to 2.83%. Again, we recall that the leading edge is a transitional flow, which stresses the assumptions of the EQWM. This further emphasizes the need for additional spanwise inclusion for post-stall angles.

3.6 Transition sensitivity to grid resolution

In this work, the grid resolution utilized in all simulations (denoted as fine), other than where expressly noted, uses a resolution representative of a high-lift Common Research Model (CRM-HL) configuration with a total grid count of 1.5 billion CV [45]. To determine the appropriateness of this resolution, we conduct a grid resolution study for each ice shape at selected angles of attack. Figures 3.28 and 3.29 compare the convergence of pressure coefficients for each geometry at both a pre-stall and post-stall angle of attack. We observe reasonable grid convergence between the three resolutions for all pre-stall angles of attack across all geometries [Figures 3.28 (a,c,e) and 3.29 (a,c,e)]. Additionally, all geometries except the horn ice geometry are in good agreement with the provided experimental data of [15]. An overpredition of C_p at the leading edge of the horn ice geometry is observed in Figure 3.29(a). As suggested by Figures 3.7 and 3.28 (b,d,f), additional refinement is required to converge the integrated quantities at and beyond the stall angle. In larger ice structures, such as horn, streamwise, and spanwise ridge ice geometries, we note reduced sensitivity to grid

resolution at stalled angles depicted in Figure 3.29 (b,d,f). Specifically, the streamwise and spanwise ridge ice shapes overpredict leading edge pressures; however, they still yield a stalled airfoil in agreement with experimental data. With the current modeling approach, the transition is handled implicitly, meaning we do not employ an additional transition model for the leading edge region. In Figures 3.30 and 3.31, we plot the friction coefficient, C_f, against the streamwise coordinate for each geometry. We observe that the transition location is sensitive in the clean geometry [Figure 3.30 (a,b)], as increasing resolution leads to earlier transitions for both pre-and post-stall angles of attack. The convergence to the experimental data is slow for the clean and spanwise ridge cases and warrants the use of a better transition model.

In contrast, the early-time glaze [Figure 3.30 (c,d), horn [Figure 3.31 (a,b)], and streamwise [Figure 3.31 (c,d)] ice geometries show minor sensitivity to transition location with increasing grid resolution. This illustrates that the roughness elements act as a tripping mechanism for the boundary layer. This is not always the case. For early-time rime ice geometries, the scale of the roughness elements is small enough that at our medium and fine grid resolutions, we do not have enough points per roughness height to capture this roughness-induced transition. This is observed in Figure 3.30 (e,f), where increasing the grid resolution from fine to extra-fine moves the transition location closer to the leading edge. Similarly, the transition location of the spanwise-ridge ice shape shown in Figure 3.31 (e,f) moves further upstream with additional grid resolution. The transition region, positioned upstream of the ice shape, exhibits behavior more akin to the clean geometry.

3.7 Rectangular versus free-air configuration domain sensitivity study

A rectangular domain was employed in this study to minimize the introduction of points in the far field region of the flow due to code-specific imposed constraints of isotropic grid cells and a minimum of four points in the spanwise direction. To determine the efficacy of utilizing a rectangular domain, as opposed to a free-air configuration, we ran comparison studies between the two geometries at an angle of attack of 9.3° for the clean airfoil geometry. The free-air configuration is run with a cylindrical domain that extends fifty chord lengths away from the airfoil in the radial direction. In Figure 3.32, drag coefficients, C_D, are plotted with respect to the number of flow-through times in the simulation for both the free-air condition (with a 50 radial chord length boundary) and the tunnel geometry (as specified in Figure 3.5). The transparent data represents the instantaneous force data, while the solid lines are filtered using a moving average for approximately 2.5 flow-through times. It is observed that the free-air configuration requires many more flow-throughs before it becomes statistically stationary (approximately $60 - 70$ flow-through times for the free-air configuration in this case). This contrasts the tunnel configuration, whose usable statistics begin at approximately $20 - 25$ flow-through times.

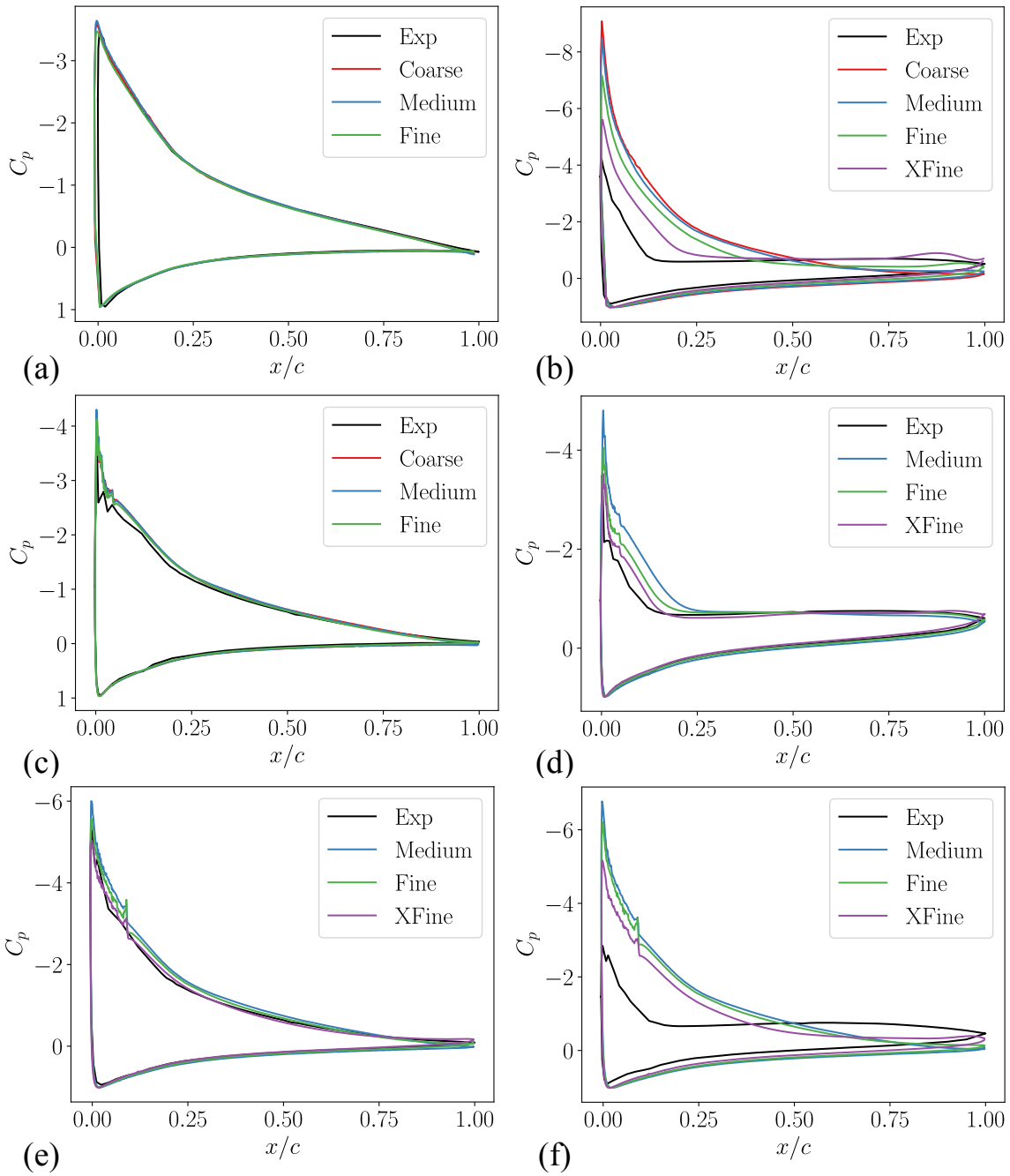

Figure 3.28: Grid sensitivity of pressure coefficients (C_p) for the clean geometry at (a) $\alpha = 9.3°$ and (b) $\alpha = 16°$ ($S_p = 0.125c$), early-time glaze ice geometry at (c) $\alpha = 9.3°$ ($S_p = 0.2c$) and (d) $\alpha = 14°$ ($S_p = 0.8c$), and early-time rime ice geometry at (e) $\alpha = 12°$ and (f) $\alpha = 13°$ ($S_p = 0.125c$).

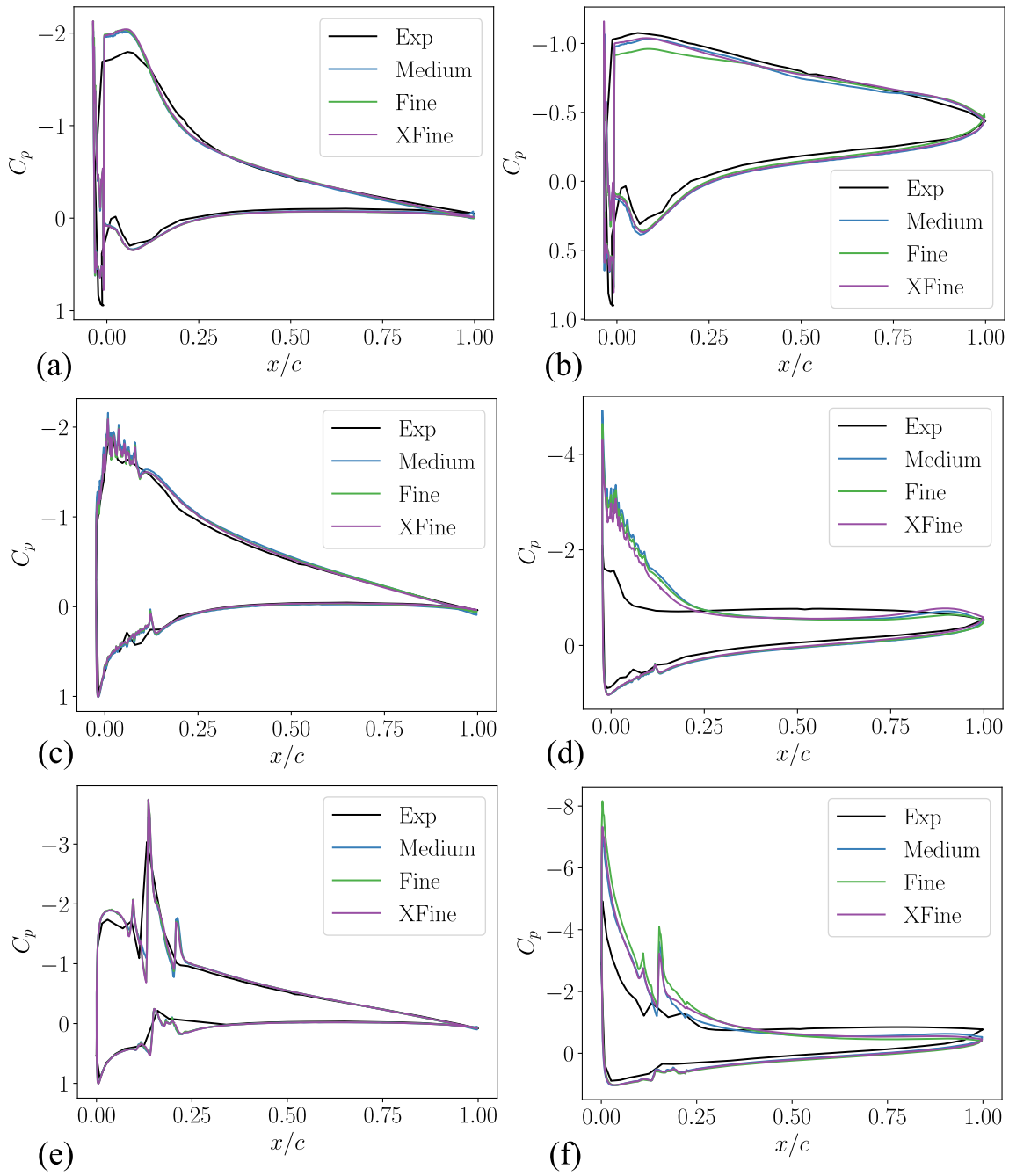

Figure 3.29: Grid sensitivity of pressure coefficients (C_p) for the horn geometry at (a) $\alpha = 6°$ and (b) $\alpha = 10°$ ($S_p = 0.8c$), streamwise ice geometry at (c) $\alpha = 6°$ and (d) $\alpha = 14°$ ($S_p = 0.25c$), and spanwise ridge ice geometry at (e) $\alpha = 6°$ and (f) $\alpha = 18°$ ($S_p = 0.25$).

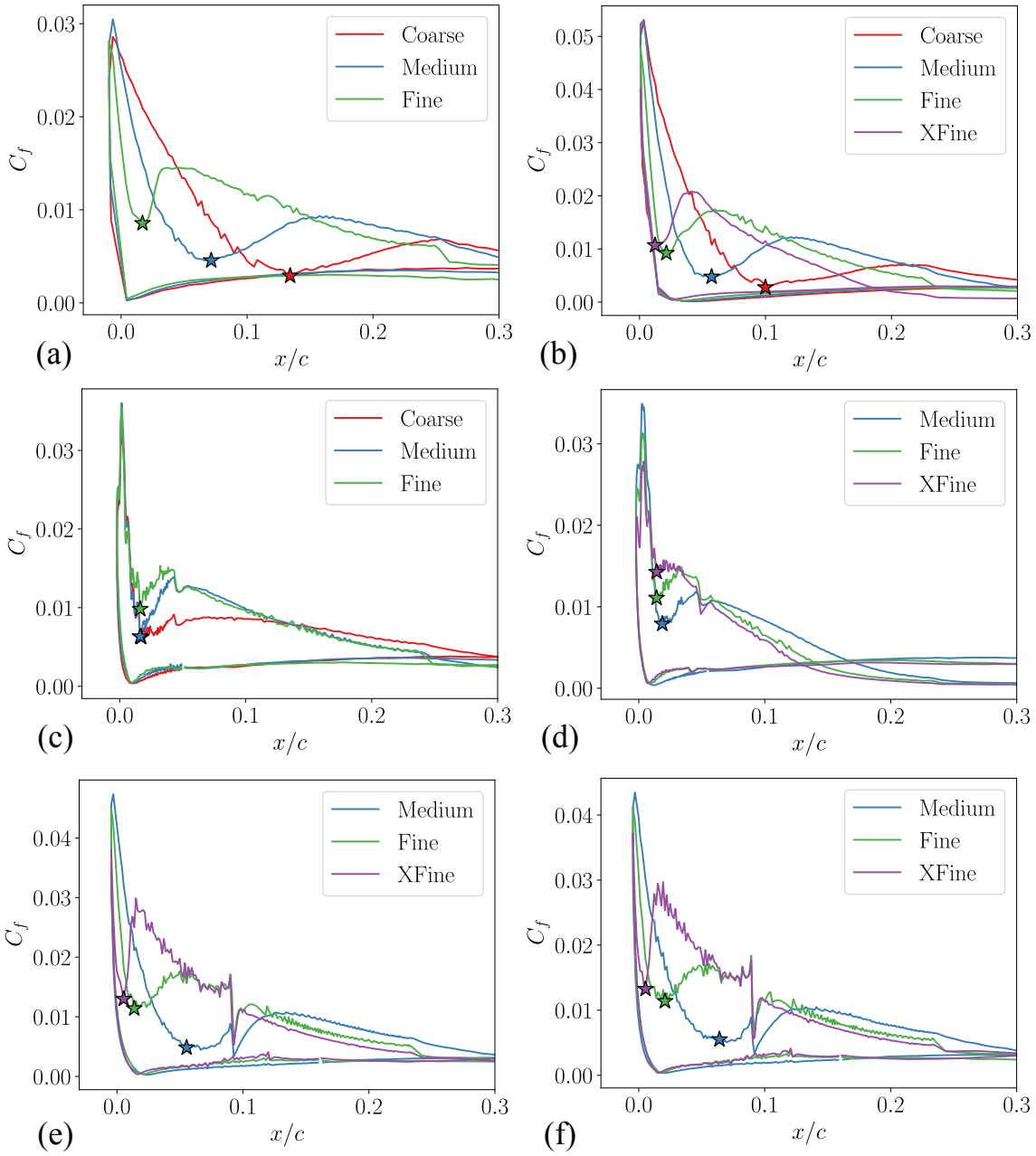

Figure 3.30: Sensitivity of friction coefficients (C_f) for the clean geometry at (a) $\alpha = 9.3^\circ$ and (b) $\alpha = 16^\circ$ ($S_p = 0.125c$), early-time glaze ice geometry at (c) $\alpha = 9.3^\circ$ ($S_p = 0.2c$) and (d) $\alpha = 14^\circ$ ($S_p = 0.8c$), and early-time rime ice geometry at (e) $\alpha = 12^\circ$ and (f) $\alpha = 13^\circ$ ($S_p = 0.125c$) with increasing grid resolution.

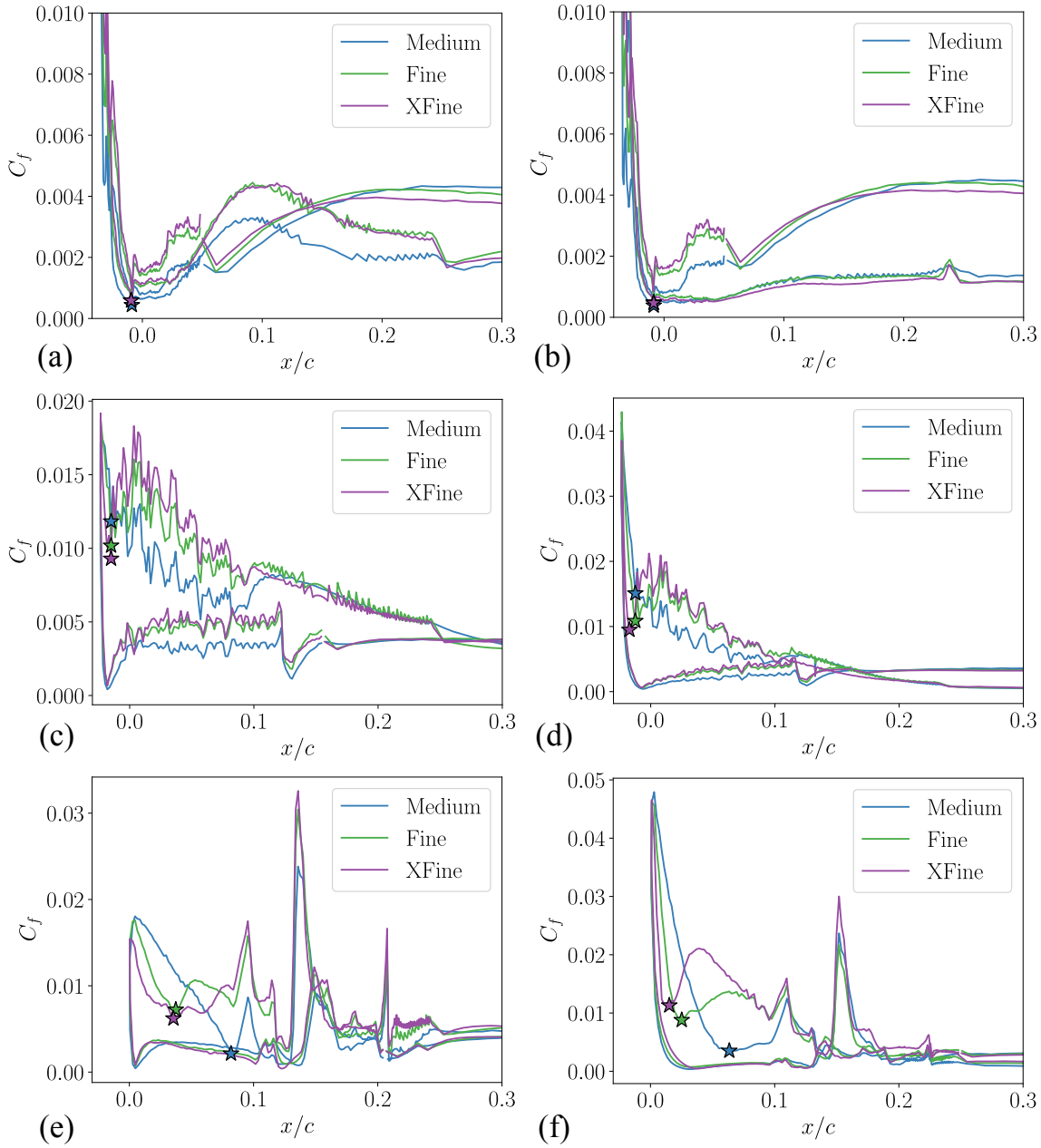

Figure 3.31: Sensitivity of friction coefficients (C_f) for the horn geometry at (a) $\alpha = 6°$ and (b) $\alpha = 10°$ ($S_p = 0.8c$), streamwise ice geometry at (c) $\alpha = 6°$ and (d) $\alpha = 14°$ ($S_p = 0.25c$), and spanwise ridge ice geometry at (e) $\alpha = 6°$ and (f) $\alpha = 18°$ ($S_p = 0.25$) with increasing grid resolution.

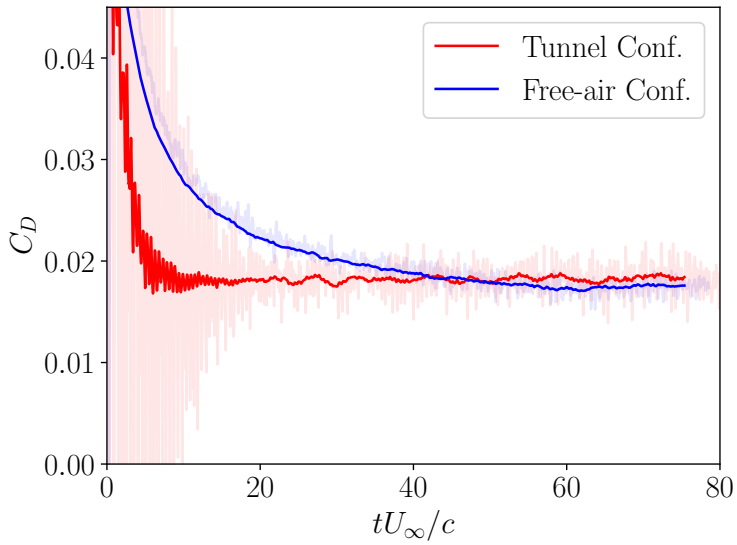

Figure 3.32: Drag coefficient versus flow-through times (tU_∞/c) for the free-air and tunnel configurations at $\alpha = 9.3°$.

3.8 Temporal convergence for various ice shapes

It is critical to evaluate how long to run simulations when using a WMLES approach. To this end, we plot the instantaneous lift coefficient in Figure 3.33 as a function of chord-based flow through times, tU_∞/c, for the (a) early-time glaze, (b) early-time rime, (c) horn, (d) streamwise, and (e) spanwise ridge ice shapes. Multiple α values are selected in each case, including at least one in the pre-stall and one in the post-stall regime. As can be observed, the post-stall α values consist of highly unsteady effects due to the large transient time scales of the massive separation occurring near the iced airfoil's leading edge. Therefore, the stalled angles require a minimum of 40 chord-based flow-through times compared to the pre-stalled angles for an accurate representation of the integrated forces. The simulations at post-stall angles require additional flow-through times to get fully converged loads. This is especially true for shapes such as the spanwise ridge and horn ice geometries of Figure 3.33(c,e), whose loads can exhibit low-frequency oscillations.

3.9 Impact of boundary condition selection for ice shapes

The EQWM assumes the presence of a fully developed turbulent boundary layer, which is not an accurate representation of flows with large obstructions, such as those simulated with ice shapes. Here, we test the sensitivity of utilizing a no-slip boundary condition instead of the EQWM boundary condition for each ice shape. The no-slip condition assumes zero velocity at the boundary, an appropriate condition in the $y^+ < 1$ limit. In this case, we use it as a sensitivity study on meshes

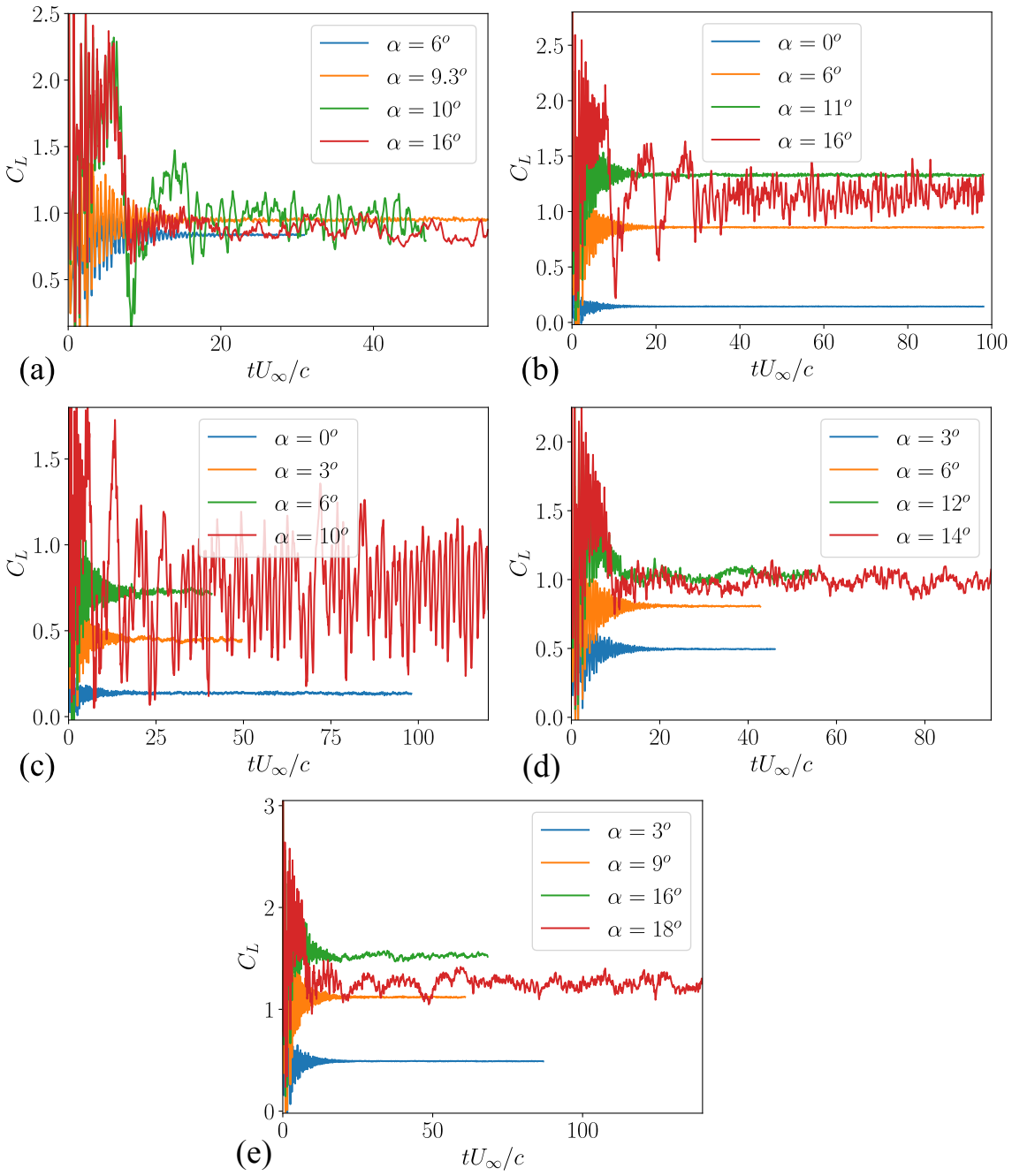

Figure 3.33: Instantaneous lift coefficients as a function of chord-based flow through times (tU_∞/c) at selected angles for the (a) early-time glaze, (b) early-time rime, (c) horn, (d) streamwise, and (e) spanwise ridge ice shapes.

Table 3.5: Comparison of fine grid integrated force errors between the EQWM and no-slip boundary conditions for each ice shape at a pre-stall α.

Ice shape	α	S_p	Lift counts - EQWM ($\lvert\Delta C_L\rvert = 0.01$)	Lift counts - No slip ($\lvert\Delta C_L\rvert = 0.01$)	Drag counts - EQWM ($\lvert\Delta C_D\rvert = 0.0001$)	Drag counts - No slip ($\lvert\Delta C_D\rvert = 0.0001$)
Early-time glaze	10°	0.2	5.5	9.3	22.9	20.1
Horn	6°	0.8	2.7	2.1	38.1	72.3
Early-time rime	6°	0.125	7.6	10.6	7.4	40.5
Streamwise	6°	0.25	5.4	7.8	8.2	45.2
Spanwise ridge	12°	0.25	5.8	12.8	12.4	85.3

whose $y^+ >> 1$. In Table 3.5, comparisons of lift and drag are made between each ice shape for a selected angle of attack in the pre-stall condition. For ice shapes with considerable geometric obstructions relative to the developing boundary layer (i.e., the horn ice shape), the EQWM is more accurate when comparing the total drag. The horn ice geometry's lift has minor sensitivity to the boundary condition. For the lift, the early-time glaze ice condition with the EQWM is four lift counts more accurate than the no-slip condition. The drag for the early-time glaze is insensitive to the choice in boundary condition. The early-time rime, streamwise, and spanwise ridge ice shapes significantly benefit from using an EQWM boundary condition. Improvements observed in these ice shapes are due to the development of a turbulent boundary layer whose height is larger than the size of the roughness. A lower wall shear stress from the no-slip condition results in lower drag relative to the experimental results of [15], yielding a larger underprediction in drag. The EQWM is generally a more accurate boundary condition as it either outperforms the no-slip condition or is minimally sensitive to the choice and, therefore, a generally more appropriate choice.

3.10 A discussion on resolutions for various ice shapes

In Section 3.6, grid resolution studies were shown for pre-stall and post-stall angle of attack for each ice geometry. To better determine the necessary grid resolution, we consider the grid points per k_{rms} and k_{max}, as shown in Figures 3.34 and f3.35, respectively, for the (a) early-time rime, (b) streamwise, (c) early-time glaze, and (d) horn ice shapes.

For the early-glaze ice shape, it was demonstrated that the fine grid resolution, suitable for a tractable simulation of a full-scale aircraft, produced reasonable results in terms of integrated forces and pressure distributions across the tested α values. However, as seen in Figure 3.34(c), this fine grid resolution offers fewer than two points per k_{rms}, which is significantly below the recommended 4-6 points per roughness height suggested by both [63] and [45]. To address this discrepancy, we refer to Figure 3.35(c), where the maximum roughness heights across the span of the domain per minimum cell size are plotted as a function of streamwise distance. Notably, the fine grid resolution has regions near the two horns with approximately 7 points per k_{max}. This is greater than the

recommended minimum values and contributes to the reasonable results obtained for this ice shape. These leading-edge roughness features are crucial for aerodynamic behaviors such as turbulence transition. We found that the transition location of this ice shape was insensitive to the tested grid resolutions (see Figure 3.30(c,d)), which aligns with the observation that these large roughness features, forcing geometrically induced transition, have at least 4 cells resolving them even at the coarsest grid tested. For the horn ice geometry, as illustrated in Figures 3.34(d) and 3.35(d), the leading-edge horns are even better resolved due to their larger scales from longer accretion times. Here, even the k_{rms} values are resolved with at least 4-6 cells at the medium resolution. The solution of the horn-ice shape was found to be more sensitive to the spanwise extent employed, as additional spanwise inclusion brought additional roughness scales into the simulation.

The resolution requirements differ significantly for the rime ice geometries. For the early-time rime ice shape, Figure 3.34(a) shows that even at the finest tested grid, there are fewer than 2 points per k_{rms}. Although the maximum value of the roughness height results in about 3-5 points per k_{max}, these features are not the dominant aerodynamic characteristics of the airfoil, where roughness is more homogeneously distributed compared to the localized geometry features of the glaze ice conditions. Therefore, even at these resolutions, errors due to the under-prediction of viscous drag from the rough surfaces were observed, as shown in Figure 3.20. This issue is alleviated at longer accretion times, as seen with the streamwise ice geometry. Figure 3.23 demonstrated good agreement with C_L as opposed to the rime ice cases for the same resolution. In Figure 3.34(b), the fine grid solution has approximately 4 points per k_{rms}, and the maximum roughness height has approximately 10 points per k_{max} as depicted in Figure 3.35(b). At these resolutions, little sensitivity to the transition location is shown in Figure 3.31(c,d). This contrasts with the early-time rime transition location shown in Figure 3.30(e,f), where significant sensitivities are observed with increasing grid resolution.

Overall, we highlight that the aerodynamics of glaze ice shapes are dominated by the largest roughness scales, and resolving these scales with more than 5 points per k_{max} results in reasonable aerodynamic predictions. In contrast, rime ice shapes, characterized by more heterogeneous roughness, require a higher overall resolution of k_{rms} to achieve similar accuracy, with $k_{rms}/\Delta_{min} > 4$ necessary throughout. Distinguishing the type of ice being simulated and understanding the relevant aerodynamic influence of the roughness scales is important in appropriately setting grid resolutions for the aerodynamic prediction of iced surfaces.

3.11 Summary

In this chapter, five NACA23012 ice geometries, along with a clean geometry, have been simulated using WMLES. These include early-time rime, streamwise (long exposure to rime), early-time glaze, horn (long exposure to glaze), and spanwise ridge (due to thermal protection system) ice shapes that

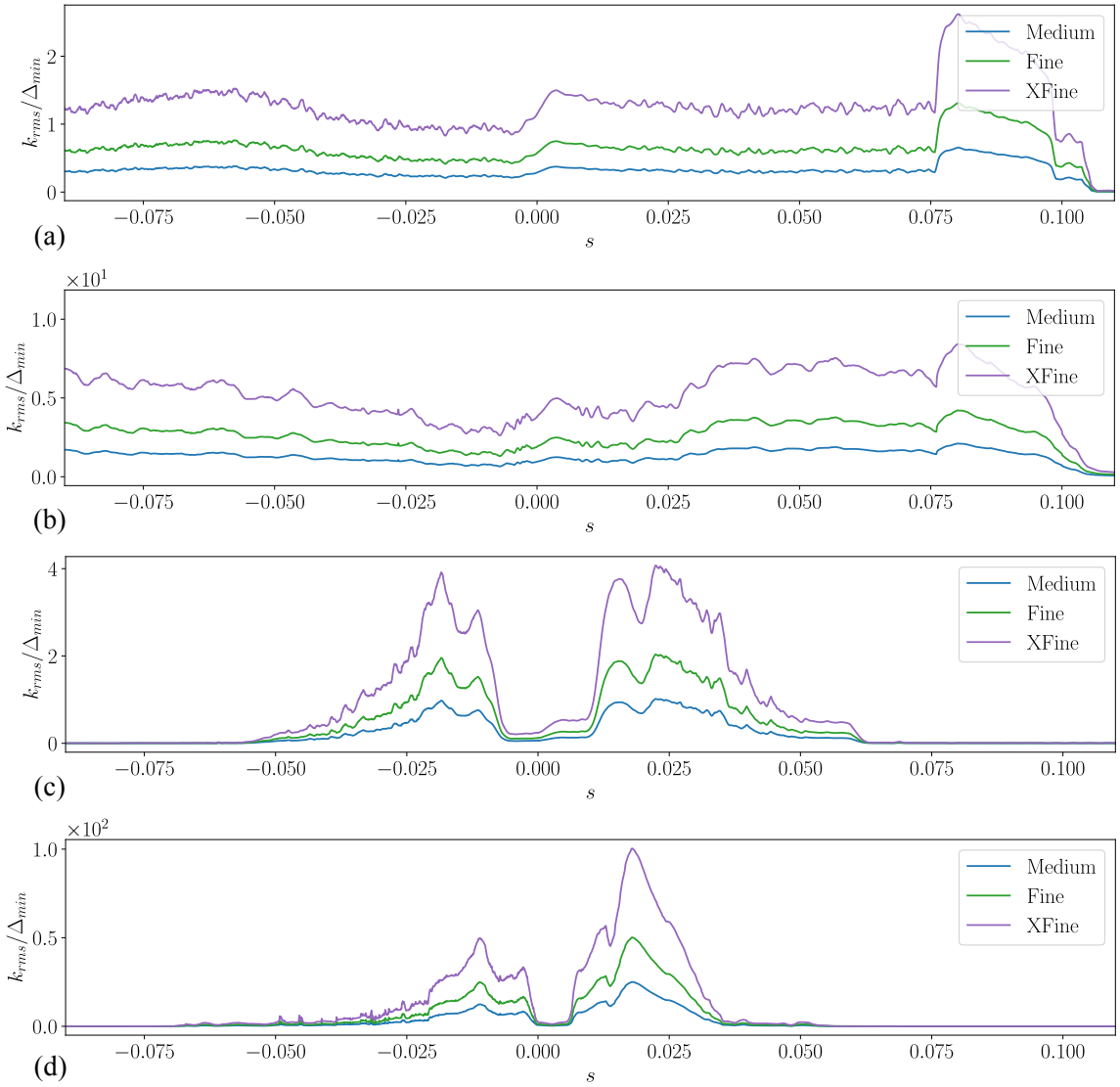

Figure 3.34: Spanwise integrated k_{rms}/Δ_{min} as a function of the streamwise coordinate for the (a) early-time rime, (b) streamwise, (c) early-time glaze, and (d) horn ice shapes at the Medium, Fine, and XFine grid resolutions (see Table 5.2 for further case details).

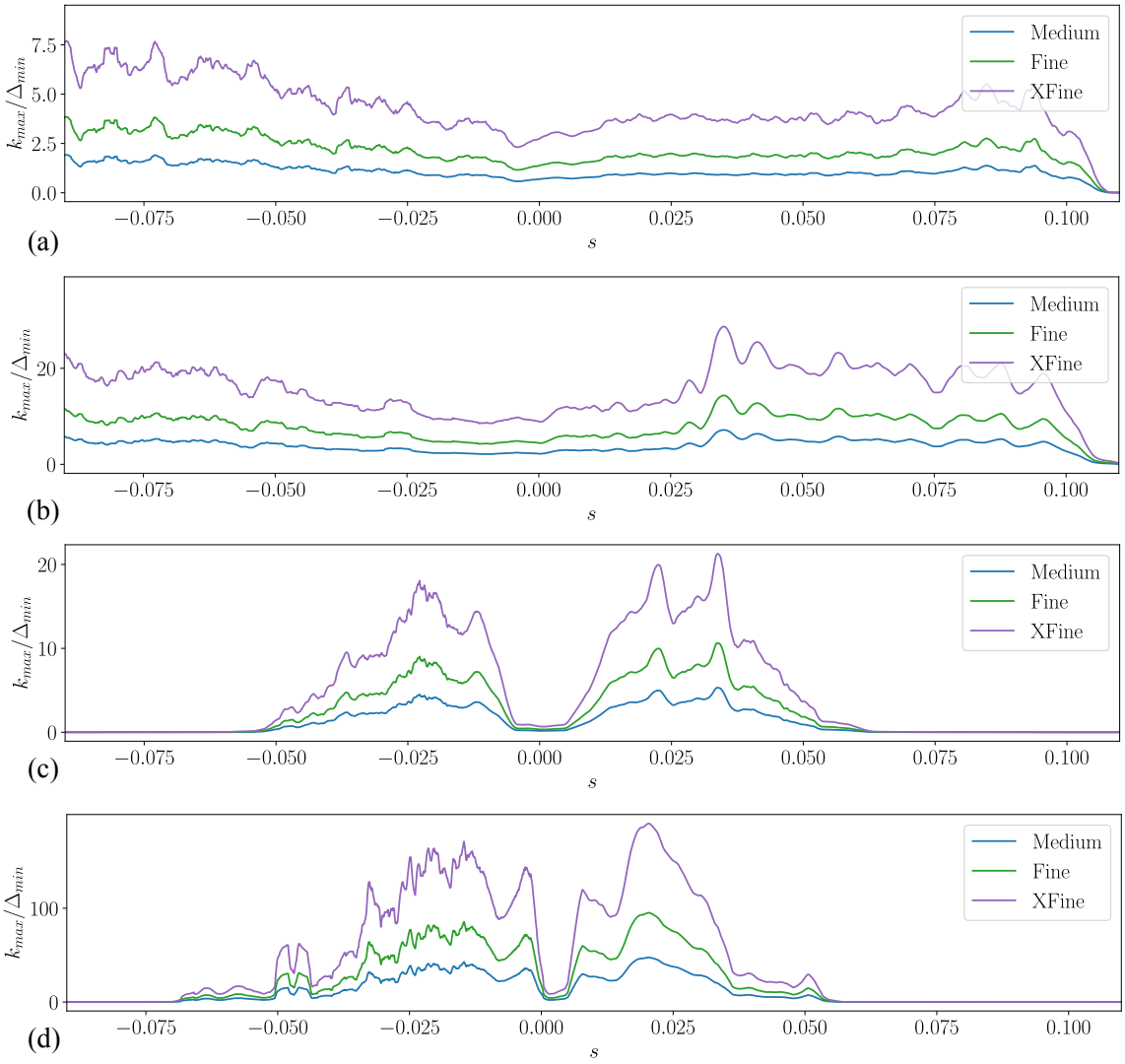

Figure 3.35: Maximum roughness height in the spanwise direction per minimum cell size, k_{max}/Δ_{min}, as a function of the streamwise coordinate for the (a) early-time rime, (b) streamwise, (c) early-time glaze, and (d) horn ice shapes at the Medium, Fine, and XFine grid resolutions (see Table 5.2 for further case details).

represent the most critical ice shapes encountered in icing conditions [11]. For each case, relevant comparisons are made to the available experimental and simulation results [15, 69] focusing on both integrated and surface quantities, such as lift, drag, moment, pressure coefficients, and wall shear stress. Ice geometries are classified using two length scales where the characteristic ice height, h, is separated from the local roughness height, k.

The baseline NACA 23012 clean geometry is simulated for a series of grid resolutions. We observed a good agreement in the linear regime across various grids, but we required an increased resolution to simulate stall successfully. Additional resolution increases, leading to a grid with 54 million cells, yielded increased accuracy in the lift, drag, and moment coefficients. It was determined to utilize a grid resolution with 14.25 million cells as the adequate resolution for the ice shapes as it is considered a tractable resolution for simulating more complicated aircraft-scale configurations of interest.

We observe improved results for the early-time glaze ice case compared to those established in the literature, such as the Lattice-Boltzmann method [69]. The WMLES results accurately capture the critical stall angle, observe the appropriate decrease in lift in the post-stall region, and yield good agreement with the rising drag coefficient at high angles of attack.

We performed a spanwise extent study for three angles of attack ($\alpha = 9.3^\circ$, $\alpha = 14^\circ$, and $\alpha = 16^\circ$). Longer span resulted in improvements for both the lift and moment coefficients in the post-stall regions. Minimal differences were observed at 9.3°. This highlights the need to simulate increased span at higher angles of attack to minimize any correlations in the flow caused by the reduced spanwise extent.

Similar results as compared to [69] were obtained for the horn ice geometry. It was shown that the increased spanwise extent was necessary to appropriately model the post-stall region. In contrast to the early-time glaze, larger differences are observed in the pre-stall angle of attack with an increased spanwise extent. This is primarily due to the inclusion of additional geometric, h, and roughness, k, length scales in the spanwise direction since the horn-ice geometry has more spanwise inhomogeneity compared to the early-time glaze ice shape. For both geometries, we observed good agreement in C_p at select angles of attack.

For the early-time rime geometry, it was observed that a 21 million cell resolution was inadequate to accurately simulate the critical angle of attack and $C_{L,max}$. The roughness scales are much smaller for this geometry. For this grid resolution, all the roughness scales are sub-grid. Therefore, additional grid resolution was required to accurately capture both α_{crit} and $C_{L,max}$. With this additional refinement, improvements were observed in both C_M and C_D coefficients. The rime ice geometry is a good candidate case for future wall modeling of rough surfaces because of the additional resolution requirements.

Compared to the early-time rime ice shape, better results are obtained for the streamwise ice geometry. The roughness scales of this geometry are larger, and therefore, the same grid resolution

results in a better representation of the roughness and how it affects the flow field. Reasonable agreement is observed for the C_L and C_M coefficients. The post-stall C_D is underpredicted but is accurate in the linear regime pre-stall.

The last geometry discussed is the spanwise ridge ice shape, which mimics the use of an ice protection system on the leading edge of the airfoil. This results in a region of clean airfoil followed by a ridge shape located downstream of the leading edge. At the simulated Re_c, the primary adverse effect of the ridge is the increased drag, which is accurately captured by the WMLES at the pre-stall angles. The stall angle is delayed due to a small geometrically induced separation bubble downstream of the ridge that locally energizes the boundary layer. The WMLES results capture the delay in the critical stall angle but overpredict it by approximately 1°.

The relevant comparisons to the experimental results of [15] show that qualitative and reasonable quantitative agreement with the experimental data is observed across all geometries. Better agreement is observed in the pre-stall region for each geometry. Additional grid resolution or modeling is required to achieve the same level of accuracy for the post-stall angles. This is particularly necessary for rime ice geometries whose roughness scales are smaller than glaze ice geometries. The combination of modeling choices: Voronoi grid generation that can resolve complex roughness elements, low-dissipation numerics, advanced wall models, and dynamic sub-grid models led to reasonable agreement with the experimental data.

Chapter 4

Near-wall modeling for LES of turbulent flows with rough walls

4.1 Background

This chapter addresses the gap outlined in Chapter 3.5.4, where the finest grid resolution when applying the EQWM to the early-time rime ice geometry still resulted in an overprediction of lift and an underprediction of drag. This was exacerbated at post-stall angles where the attempted resolutions did not result in a stalled airfoil (see Figure 3.21(b)) as expected based on the experimental work of [15]. On average, the number of points per roughness height, k_{rms}/Δ_{min}, for the Fine and XFine grids for the rime ice geometry is ~ 0.75 and ~ 1.5. This means that a significant portion of the stresses and drag forces caused by roughness are sub-grid.

This chapter introduces a new roughness wall model, the KES model, which stands for the roughness height, k_{rms}, streamwise effective slope, ES_x, and skewness, s_k. Based on these roughness parameters, first introduced in Chapter 3.3, a velocity transformation is obtained that not only provides a roughness function, ΔU^+, but also parameterizes the roughness sublayer (RSL) using a simplified linear velocity profile in the near wall region. This represents a new transform for the rough-wall boundary layer and the first comprehensive attempt at finding analogous fits to the RSL. Maintaining the RSL allows the use of the entire rough-wall boundary layer transformation with a marginally resolved rough surface. In this chapter, we first introduce the approach and optimization of the velocity transformation for rough-wall turbulent boundary layers in Section 4.2. Next, in Section 4.3, we integrate this transformation into an extension of the EQWM to include roughness effects. We then test the new model in the context of a rough channel (Section 4.3.1) and the early-time rime ice geometry first introduced in Figure 3.1(a) (Section 4.3.2). Finally, in Section 4.3.3, we compare the pre-stall angle of attack simulations to a reference WRLES (described in detail in

Appendix A).

4.2 A velocity transformation for rough-wall-bounded turbulent flows

The primary impact of various types of roughness on wall-bounded turbulent flows is the downward shift of the mean velocity profile (in semilogarithmic plots and scaled by inner boundary layer units, $y^+ = yu_\tau/\nu$ and $U^+ = U/u_\tau$, where u_τ is the friction velocity and ν is the kinematic viscosity), which indicates an increase in drag. This can be modeled by incorporating the offset in the mean velocity, known as the roughness function, ΔU^+ [30, 55]. Hama, [55], proposed the roughness function as a function of the equivalent sand-grain roughness height, k_s^+, where

$$\Delta U^+(k_s^+) = \frac{1}{\kappa}\ln(k_s^+) + B - B_r(k_s^+). \tag{4.1}$$

Here, $B = 5.2$ represents the log-law intercept for a smooth wall, and $B_r(\infty) = 8.5$ denotes the modification to the log intercept in the fully rough regime [65]. The equivalent sand-grain roughness height is a hydrodynamic quantity that represents "the grain size of uniform (monodisperse), close-packed sand grains on a hypothetical surface that would cause the same drag as the surface of interest if exposed to the same flow in the fully rough regime" [28]. It is important to note that Eq. (4.1) is applicable only to the fully-rough regime ($k_s^+ \gtrsim 80$) and necessitates knowledge of the underlying flow field [65]. For situations in the transitional rough regime, other proposed roughness functions provide modifications to Equation 4.1 fitted to a variety of rough-wall data. For instance, functions aligned with the traditional Nikuradse experiments [82] can be expressed as [34]

$$\Delta U^+(k_s^+) = \begin{cases} 0 & \text{if} \quad k_s^+ < 3 \\ \frac{1}{\kappa}\ln(0.26k_s^+) \times \sin\left(\frac{\pi}{2}\frac{\ln(k_s^+/3)}{\ln(5)}\right) & \text{if} \quad 3 < k_s^+ < 15 \\ \frac{1}{\kappa}\ln(0.26k_s^+) & \text{if} \quad k_s^+ > 15. \end{cases} \tag{4.2}$$

Other approaches, such as those fitting experimental data from [32] and [31], can be expressed as [54]

$$\Delta U^+(k_s^+) = \frac{1}{\kappa}\ln\left(1 + \frac{k_s^+}{e^{3.25\kappa}}\right). \tag{4.3}$$

In all these fits, either k_s^+ or ΔU^+ requires additional modeling to predict the impact of a rough surface on the boundary layer because of the use of k_s^+, which is a hydrodynamic quantity. In this study, we directly model the roughness function, ΔU^+, using geometrical roughness parameters, as it is conducive to modifying wall models for large-eddy simulations.

In addition to the shift in the log law, there are other modifications to the mean velocity profile

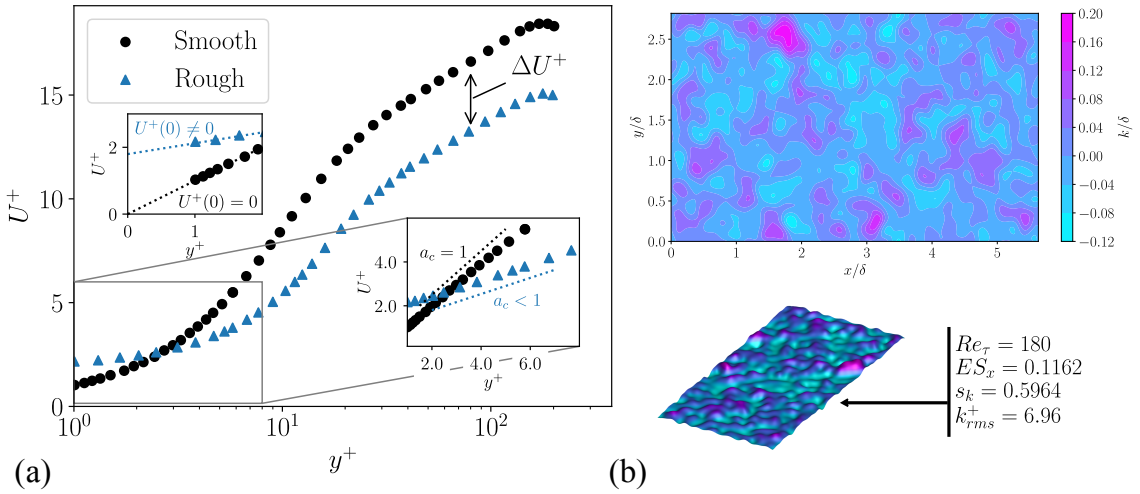

Figure 4.1: (a) Schematic highlighting the changes occurring in a smooth-wall boundary layer when bounded by a rough wall. Specific attention is paid to highlighting the modeling parameters of ΔU^+, a_c and $U^+(0)$. An example smooth-channel DNS result of [109] at $Re_\tau = 180$ is included as a reference in (a). (b) Examples of specific roughness geometry values [109].

in the viscous sublayer; for rough surfaces, this region is called the roughness sublayer (RSL). These additional modifications to the mean velocity profile include: (i) the change of slope (a_c, see Figure 4.1) in the RSL compared to the viscous sublayer in smooth-wall turbulent boundary layers, where the slope is unity; (ii) the mean velocity at $y^+ = 0$ near the wall ($U^+(0) \neq 0$, see Figure 4.1), which is otherwise zero for a smooth wall; and (iii) the extent of the RSL and where it transitions to the log-layer behavior. In Figure 4.1(a), we show an example of a mean velocity profile of a turbulent boundary layer for both a clean and rough surface at $Re_\tau = 180$ plotted in inner units. These are representative direct numerical simulations (DNSs) from the work of [109]. The two inset figures of Figure 4.1(a) illustrate the described modifications in the RSL.

Rough surfaces can be characterized using averaged geometric parameters with regards to roughness elements, such as (but not limited to) the average roughness height (k_a), root-mean-square (RMS) roughness height (k_{rms}), streamwise effective slope (ES), skewness (s_k), and kurtosis (k_{ku}). These values are defined as

$$k_a = \frac{1}{A_s} \int \int |k(x,z)| \, dxdz, \tag{4.4}$$

$$k_{rms} = \sqrt{\frac{1}{A_s} \int \int k(x,z)^2 dxdz}, \tag{4.5}$$

$$ES = \frac{1}{A_s} \int \int \left| \frac{\partial k(x,z)}{\partial x} \right| dxdz, \tag{4.6}$$

$$s_k(s) = \frac{1}{k^3_{rms}} \frac{1}{A_s} \int \int k(x,z)^3 dxdz, \tag{4.7}$$

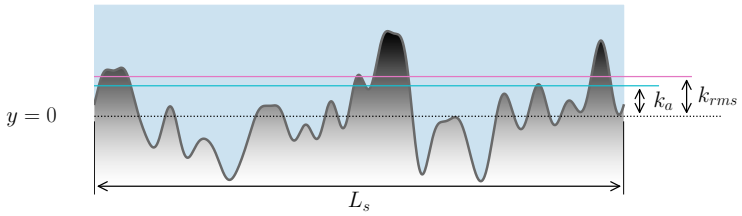

Figure 4.2: Roughness height examples with emphasis on the identification of $y = 0$, the arithmetic mean of the rough surface, k_a, the average roughness height, and k_{rms}, the root-mean-square roughness height along a reference length, L_s.

and

$$k_{ku} = \frac{1}{k_{rms}^4} \frac{1}{A_s} \int \int k(x,z)^4 dx dz \tag{4.8}$$

respectively, where A_s is the area of the rough surface and $k(x,z)$ is the local departure from the averaged rough surface, herein defined as $y = 0$. In Figure 4.2, different roughness heights and the $y = 0$ reference coordinate are illustrated. Additional discussion of these parameters and others can be found in [62], [65] and [28].

It has been shown that roughness requires at least two or more parameters to appropriately characterize its effect on near-wall turbulent flows [33, 40, 65]. Various correlations have been proposed to model roughness elements in different flow configurations [33, 39, 41, 64, 67, 74, 120]. However, the search for a universal roughness model is still an active area of research. A significant challenge in using the available correlations in the literature to develop a roughness subgrid model is that the correlations rely on the effective hydrodynamic roughness length scale instead of a geometric roughness length scale, which limits their predictive capability.

First, we gather a roughness database from available DNS datasets to construct a velocity transformation for rough-wall-bounded turbulent channel flows. We divide the mean velocity profiles into two regions: the RSL and the log layer. Within each region, we construct correlations that incorporate at least two roughness parameters for (i) the log-layer roughness function, (ii) the slope of the RSL (a_c), and (iii) the averaged velocity at the arithmetic mean location of the rough surface [$\Delta U^+_{RSL} \equiv U^+(y^+ = 0)$]. For ΔU^+, we propose an improved correlation compared to the existing correlations in the literature. In the RSL region, we propose the first parameterization of the velocity profile with respect to geometric characteristics of roughness features. A velocity transformation that uses these correlations is then computed and compared with the available DNS velocity profiles.

4.2.1 Construction of a DNS database

A DNS database containing turbulent rough-wall channel flows is constructed to study how various roughness parameters influence mean flow properties. Mean velocity profiles and roughness statistics

Paper	Number of cases	Symbol	Re_τ	k_a^+	k_{rms}^+	ES	s_k
[24]	14	▲	180–540	1.01–32.4	1.25–40	0.09–0.361	0
[25]	4	●	540	24	30	0.27–0.72	0
[109]	16	✚	180	4.37–7.42	5.7–9.17	0.06–0.32	–0.52–0.6
[110]	8	■	180–720	0.62–19.8	0.8–25.75	0.23	–0.52
[75]	2	◀	400–600	2.22	2.78	0.265	–0.053
[19]	7	✖	395	6.636–10.3885	9.243–13.035	0.198–0.209	–2.3–2.3
[64]	32	▶	1000	6.6–36.7	8.2–43.7	0.07–0.92	–0.22–2.37
Total	83		180–1000	0.62–36.7	0.8–43.7	0.06–0.92	–2.3–2.37

Table 4.1: Details of the constructed DNS database.

are extracted from available DNS data in the literature. A total of 98 rough-wall channel and pipe flows spanning both the transitional ($k_s^+ < 80$) and fully-rough ($k_s^+ > 80$) regimes are considered with various roughness topographies. We utilize 83 of these geometries to develop our model. The geometries excluded fall into one of three categories: (i) highly dense roughness where the predominant length scale changes the relevant Reynolds number to be defined by the gap between the peaks of the roughness, found in canopy-type roughness (here, we define these surfaces as $ES \geq 0.5$ and $s_k \leq -0.1$); (ii) surfaces with highly non-isotropic slopes, whose ratio of slopes (in the streamwise and spanwise directions) exceed 10; and (iii) geometries well within the wavy regime, where roughness topographies have large in-plane wavelengths, λ ($\lambda^+ > 800$). These surfaces require additional modeling, specifically in the buffer layer. Table 4.1 includes details of the various cases. In particular, we focus on the variations in the *RMS* height, k_{rms}^+, the streamwise ES, and the skewness, s_k, as critical parameters for our investigation. The variation in topography across the different rough surfaces results in a broad spectrum of velocity profiles. The values utilized in the database are representative of the relevant ice shapes. Specifically, for the rime ice shape, we obtain a range of roughness parameters where k_{rms}^+ ranges from 0-35, ES ranges from 0.2-0.4, and s_k ranges from -0.2-0.2. For the streamwise ice shape, we have ES ranges between 0.4-1.0 and s_k ranges from -2.0-2.0. In Figure 4.3, velocity profiles in inner units are plotted on a semi-log scale in (a) and in outer units in (b). This shows a drastic variation in velocity profiles between the surfaces.

4.2.2 Constant stress layer assumption in roughness sublayer

In Figure 4.3(b), velocity profiles in the near-wall region are plotted in outer units. We observe that in the near-wall region, the rough-wall velocities largely behave linearly. This observation has also been made in the rough-bed flow literature. Nikora *et al.* [81] postulated three models for the velocity based on (i) a constant profile, (ii) an exponential profile, and (iii) a linear profile for the roughness sublayer. These were tested against a data set of experimental rough-bed flows, and it was found that both the exponential and linear profiles were acceptable. In our rough-wall channel

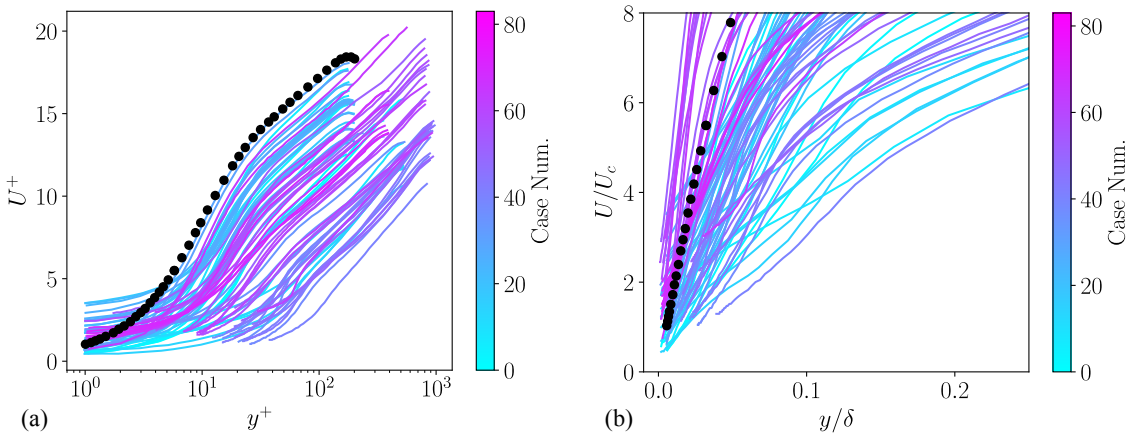

Figure 4.3: Extracted DNS rough-wall boundary layer profiles from the database in Table 4.1 plotted in (a) inner and (b) outer units. For reference, an example smooth channel DNS result from [109] at $Re_\tau = 180$, denoted by ●, is included. The case number corresponds to the order in Table 4.1, increasing from the top to the bottom of the table.

and pipe data set, where the wall shear stress, τ_w, is set from a prescribed pressure gradient forcing on the flow, we mainly observe a linear behavior, and therefore, we represent the RSL with a linear profile. We consider the space-time-averaged shear stress, where $\langle \tau_w \rangle$ represents the spatial average in the (x, z) plane, and $\overline{\tau_w}$ is the temporal average for a rough surface

$$\langle \overline{\tau(y)} \rangle = \nu_R \frac{d\langle \overline{U} \rangle}{dy}. \tag{4.9}$$

Here, ν_R is an effective roughness viscosity value explicitly dependent upon the form-induced stresses and form drag of the rough wall [$\nu_R = f(f_p, f_v)$] [80]. Given our linear profile assumption within the RSL, we have a constant stress layer leading to

$$\frac{\langle \overline{U(y)} \rangle}{u_\tau} = \frac{u_\tau y}{\nu_R} + \frac{\langle \overline{U(0)} \rangle}{u_\tau}. \tag{4.10}$$

Here, the model adjusts the viscosity within the RSL given a particular roughness topography where $\nu_R = (1/a_c)\nu$. With this, we arrive at

$$U^+_{RSL} = a_c y^+ + \Delta U^+_{RSL}. \tag{4.11}$$

In Eq. (4.11), $a_c \approx f(k^+_a, k^+_{rms}, ES, s_k, ...)$ represents the slope of the "modeled" velocity profile near the rough wall (which is unity for a smooth wall), and $\Delta U^+_{RSL} \approx f(k^+_a, k^+_{rms}, ES, s_k, ...)$ represents the averaged velocity evaluated at the arithmetic mean of the rough surface. Outside of the RSL, we model the logarithmic layer by the classical law of the wall shifted using a roughness function,

$\Delta U^+ \approx f(k_a^+, k_{rms}^+, ES, s_k, ...)$, where

$$U^+ = \frac{1}{\kappa}\ln y^+ + B - \Delta U^+. \tag{4.12}$$

To ensure a continuous velocity profile, we enforce C^0 continuity between Eqs. (4.11) and (4.12).

4.2.3 Roughness viscosity correlation

Understanding the behavior of the inverse of roughness viscosity, a representation of the slope in the RSL, is crucial for modeling the turbulent velocity profile. In this section, we investigate how a_c correlates with three important parameters: k_{rms}^+, ES, and s_k. In Figure 4.4, the relationship between a_c and these parameters and their combinations are illustrated. Figure 4.4(a) highlights a strong correlation between k_{rms}^+ and a_c. As the inner-scaled roughness height increases, the slope of the RSL decreases. A similar trend is noted with increasing ES in Figure 4.4(b). While s_k shows a weaker correlation, the higher skewness values appear to correspond to a smaller slope. However, this correlation might be influenced by the increased k_{rms}^+ for cases with high skew.

Figure 4.4(d) presents the slope of the RSL for a combination of k_{rms}^+ and ES. Many combinations of k_{rms}^+ and ES were conducted. A reasonable collapse is found where the best fit is achieved when using $k_{rms}^{+2}\sqrt{ES}$. An exponential decay of a_c as a function of $k_{rms}^{+2}\sqrt{ES}$ is shown in Figure 4.4(d). Based on this observation, we propose the following functional form for the a_c model

$$a_c = c_1 \ln(c_2 x + c_3), \tag{4.13}$$

where $x = 1/k_{rms}^{+2}\sqrt{ES}$ and c_1, c_2 and c_3 are constants yielding the best fit. This approach achieves an $r^2 = 90.3\%$ fit, where

$$r^2 = 1 - \left(\frac{\sum_{i=1}^{n}(a_{c,DNS} - a_c)^2}{\sum_{i=1}^{n}(a_{c,DNS} - \overline{a_c})^2}\right) \tag{4.14}$$

with n as the total number of data points. Busse *et al.* [19] found that the roughness function was related to s_k by a weighted hyperbolic tangent function. Following the work of [19], we modify Eq. (4.13) to include asymmetries introduced by s_k. The final proposed fit

$$a_c = c_1 \ln(c_2 x + c_3)[(c_4 - 1)\tanh(c_5 s_k) + 1] \tag{4.15}$$

improves the fit to 93.3%, shown in Figure 4.5, which is acceptable given the wide variety of roughness topologies considered.

4.2.4 Mean roughness velocity intercept correlation

Following a methodology similar to that in Section 4.2.3, we investigate correlations between roughness parameters and the mean roughness velocity intercept, ΔU_{RSL}^+. In Figure 4.6(a), a weak

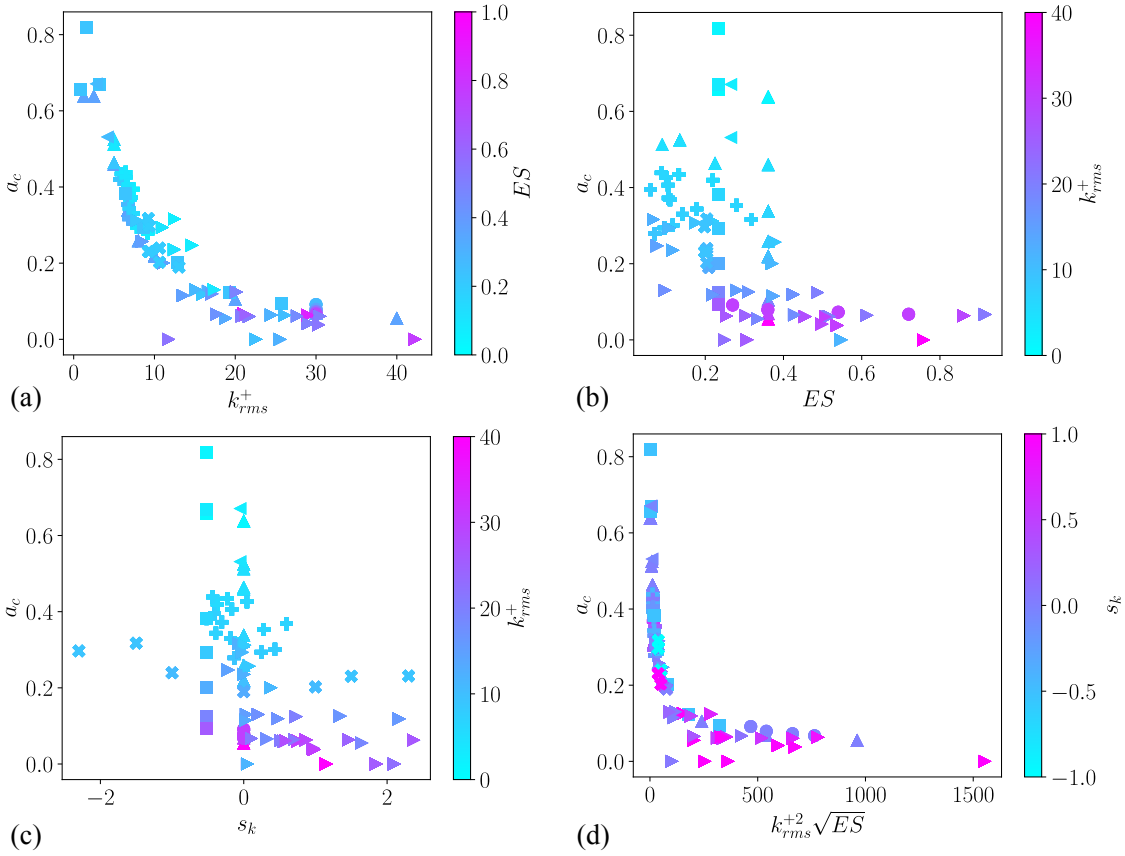

Figure 4.4: Dependence of the inverse roughness viscosity, a_c, on geometrical parameters: (a) k^+_{rms}, (b) ES, (c) s_k and (d) $k^{+2}_{rms}\sqrt{ES}$. Mappings of symbols to relevant studies can be found in Table 4.1.

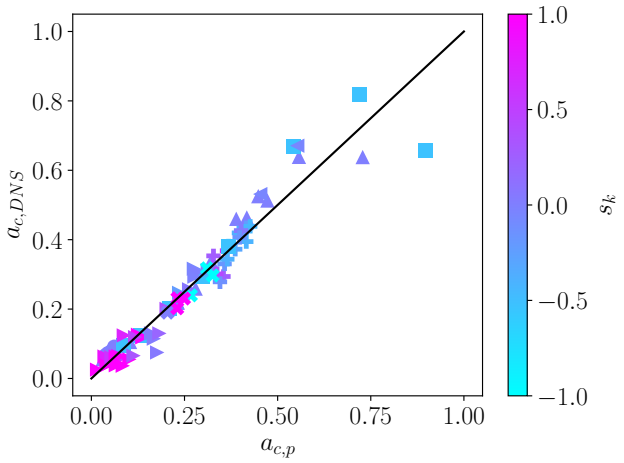

Figure 4.5: Dependence of the predicted linear coefficient, $a_{c,p}$ with respect to the DNS data linear coefficient, $a_{c,DNS}$, from Eq. 4.15.

correlation exists between ΔU^+_{RSL} and k^+_{rms}, where in general, ΔU^+_{RSL} increases with increasing k^+_{rms}. This can be seen by looking at individual symbol groups, such as those by [109] [✚, in Figure 4.6(a)] or [24] [▲, in Figure 4.6(a)], where increased roughness heights result in increased ΔU^+_{RSL}. Figure 4.6(b) reveals an inverse relationship between ES and ΔU^+_{RSL}, where increased slopes result in near-zero velocity at the arithmetic mean roughness height. Additionally, symbols colored by k^+_{rms} increase in value from the bottom left to the top right of Figure 4.6(b). This shows a direct relation between the roughness height and effective slope for the velocity at the arithmetic mean geometric location. Figure 4.6(c) shows little correlation with skewness. Therefore, we postulate that k^+_{rms} and ES are the critical parameters influencing the mean roughness velocity intercept correlation. In Figure 4.6(d), we explore the relationship between k^+_{rms} and ES as a ratio, considering it as a model for the average wavelength of the roughness topology. Weighting the effective slope in Figure 4.6(e) improves the best-fit correlation. Utilizing the same model form as Eq. (4.13), we propose the following expression for the ΔU^+_{RSL} model

$$\Delta U^+_{RSL} = c_1 \ln\left(c_2 x + c_3\right), \tag{4.16}$$

where $x = k^+_{rms}/ES^2$. This model results in a 81.0% fit, as depicted in Figure 4.7. While the overall fit may not be as accurate as the roughness viscosity correlation, Eq. 4.16 introduces less absolute error to the total velocity fit.

4.2.5 Roughness function correlation

Correlations for the roughness function, ΔU^+, or the equivalent sand-grain roughness, k^+_s, have been proposed by numerous research groups [39, 41, 64, 67, 74, 120]. Each correlation is based on the data

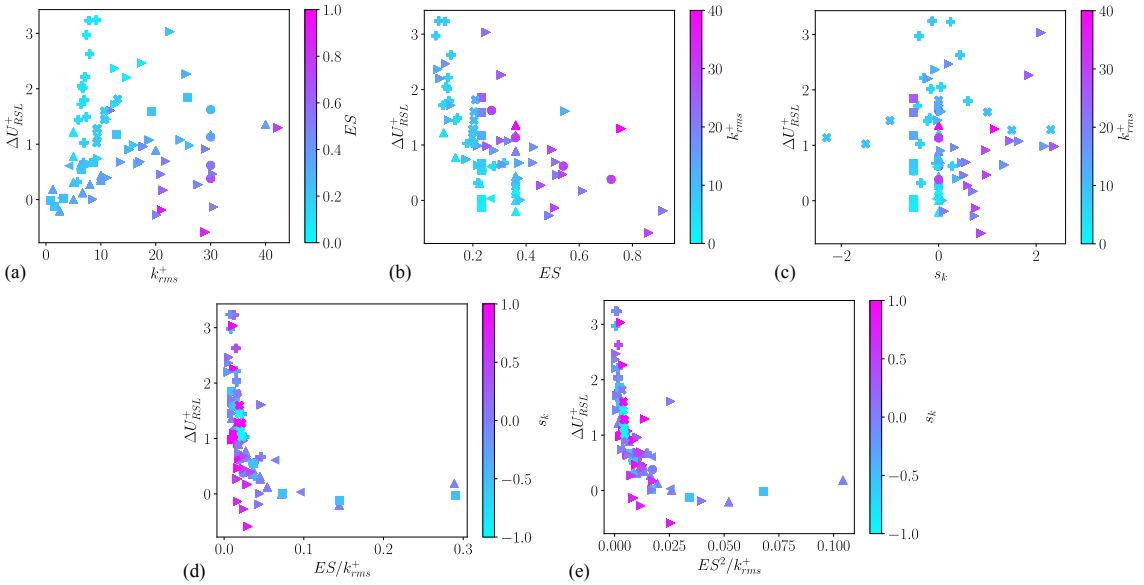

Figure 4.6: Dependence of ΔU^+_{RSL} on geometrical parameters: (a) k^+_{rms}, (b) ES, (c) s_k, (d) ES/k^+_{rms} and (e) ES^2/k^+_{rms}. Mappings of symbols to relevant studies can be found in Table 4.1.

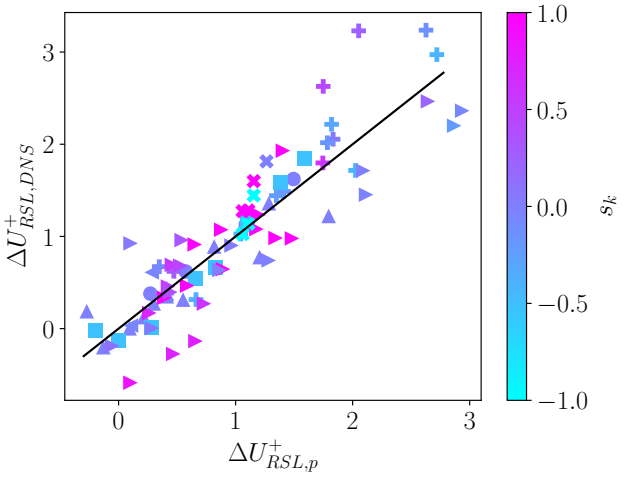

Figure 4.7: Dependence of $\Delta U^+_{RSL,DNS}$ with respect to the predicted value from Eq. 4.16, $\Delta U^+_{RSL,p}$.

available to the authors, making the model's performance contingent upon the specific roughness characteristics considered. Previous studies have developed their models by incorporating one, two, three, or more roughness parameters. Recent work by [40] consolidated these various approaches into a comprehensive table. Chung *et al.* [28] postulated that a predictive roughness function should incorporate at least three parameters: (i) the roughness height, (ii) a description of the frontal area and (iii) a description of the surface coverage. Here, we leverage the DNS database to develop a three-parameter model, incorporating k^+_{rms}, ES, and s_k, with improved performance compared to existing two-parameter models [24, 33, 39].

Figure 4.8 illustrates the behaviors of the roughness function concerning various roughness parameters and their combinations. A strong dependence of the roughness function on k^+_{rms} is evident in Figure 4.8(a) as larger roughness leads to increased drag on the surfaces. In Figure 4.8(b), we see a similar trend to that of [79], where a plateau in ΔU^+ occurs at high ES, and as ES goes to zero, there is a quick decay in the roughness function. Skewness exhibits a noticeable impact in specific studies, such as in [19] [✖ values in Figure 4.8(c)], where they fixed the roughness height and slope while varying the skewness parameter and showed that the roughness function behaved similarly to an asymmetric hyperbolic tangent function. Building on the insights of [33], we plot ΔU^+ with respect to $k^+_{rms}ES$ in Figure 4.8(d). Similar to their results, a strong logarithmic correlation is observed. Flack *et al.* [39] determined that additional considerations are likely necessary for surfaces approaching the wavy regime.

We explore an exponential response of ES for the roughness function in Figure 4.8(e) and find a notable correlation between the variables. Combining the ideas from Figure 4.8(d,e) in Figure 4.8(f) yields a reasonable collapse among the data.

We adopt the model form of Eq. (4.13) with three coefficients and set $x = k^+_{rms}ES$. In refining this model, we draw insights from Figure 4.8(c,e). Adjusting the model to accommodate skewness and account for surfaces with higher ES led us to propose the following modified model form for the roughness function

$$\Delta U^+ = c_1 \ln\left(c_2 k^+_{rms} ES\right)\left[(c_3 - 1)\tanh\left(c_4 s_k\right) + 1\right] e^{-c_5 ES^{c_6}}. \tag{4.17}$$

This final form of the roughness function yields a 95.4% fit with the available DNS database. Table 4.2 compares two-parameter models available in the literature by [39], [67], [24], and [33]. The models of [39] and [67] directly compute k^+_s as a function of k^+_{rms} and s_k. Therefore, we must apply a roughness function to compare these fits to ΔU^+. We use three roughness functions widely accepted in the literature to compute ΔU^+ given the modeled k^+_s: Hama type [[55], Eq. (4.1)], Nikuradse type [[34], Eq. (4.2)], and Colebrook type [[32], Eq. (4.3)]. Across all correlations, we find that both the proposed model and model of de Marchis *et al.* [33] best fit the current DNS database, with the proposed model being slightly improved at the cost of increased model complexity (see Section 4.2.7 for a further comparison of [33] and the present model). In Figure 4.9,

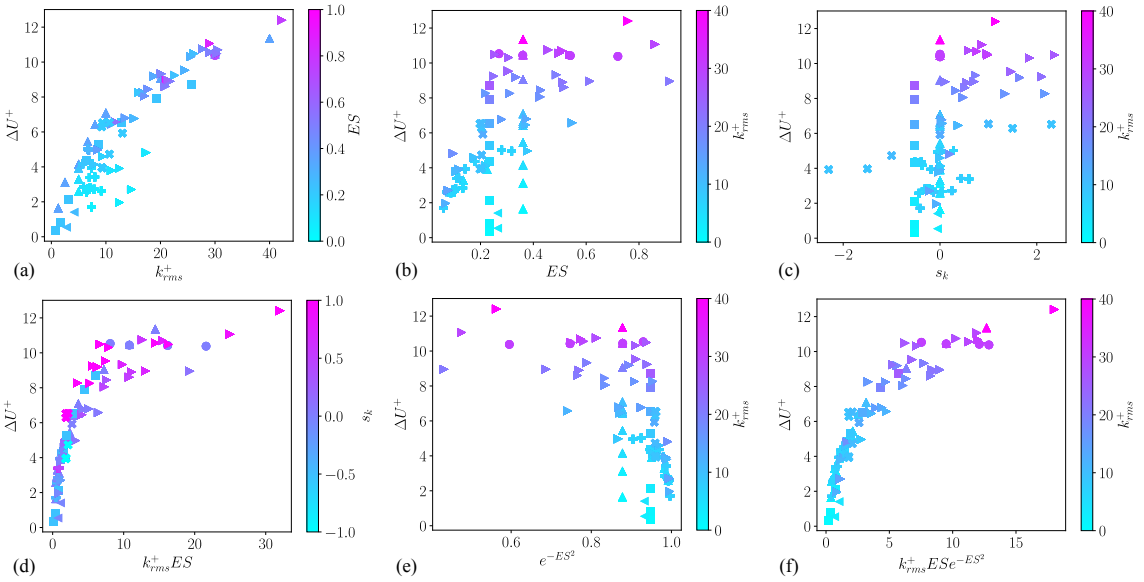

Figure 4.8: Dependence of the roughness function, ΔU^+, on geometrical parameters: (a) k^+_{rms}, (b) ES, (c) s_k, (d) $k^+_{rms}ES$, (e) e^{-ES^2} and (f) $k^+_{rms}ES e^{-ES^2}$. Mappings of symbols to relevant studies can be found in Table 4.1.

we compare the actual to predicted ΔU^+ values for each of the fits from Table 4.2. For [39], we see better agreement for lower values of ΔU^+, with increasingly overpredicted values at higher ΔU^+. The opposite issue is noticed in [24]. The trends of [67], [33], and the current model are similar, but the spread decreases drastically from [67] to [33]. These results suggest the newly proposed model better represents the roughness of the current DNS database.

4.2.6 Transformation of rough-wall turbulent channel flows

Utilizing the correlations for the three parameters, we develop a transformation to collapse rough-wall boundary layers to the classical smooth-wall boundary layer. In the smooth wall viscous sublayer, $U^+ = y^+$. Equation 4.11 is solved for y^+ and scaled by $y^{\dagger,s}/y^{\dagger}$, where $y^{\dagger,s}$ is the wall-normal location at the transition point between the viscous sublayer and log layer for the smooth-wall ($y^{\dagger,s} \approx 11$), and $y^{\dagger}$ is the transition location between the surface's RSL and log layer (see Figure 4.10). We define this transformed RSL velocity as U^*_{RSL}, where

$$U^*_{\mathrm{RSL}} = \left(\frac{U^+ - \Delta U^+_{RSL}}{a_c} \right) \frac{y^{\dagger,s}}{y^{\dagger}}. \tag{4.18}$$

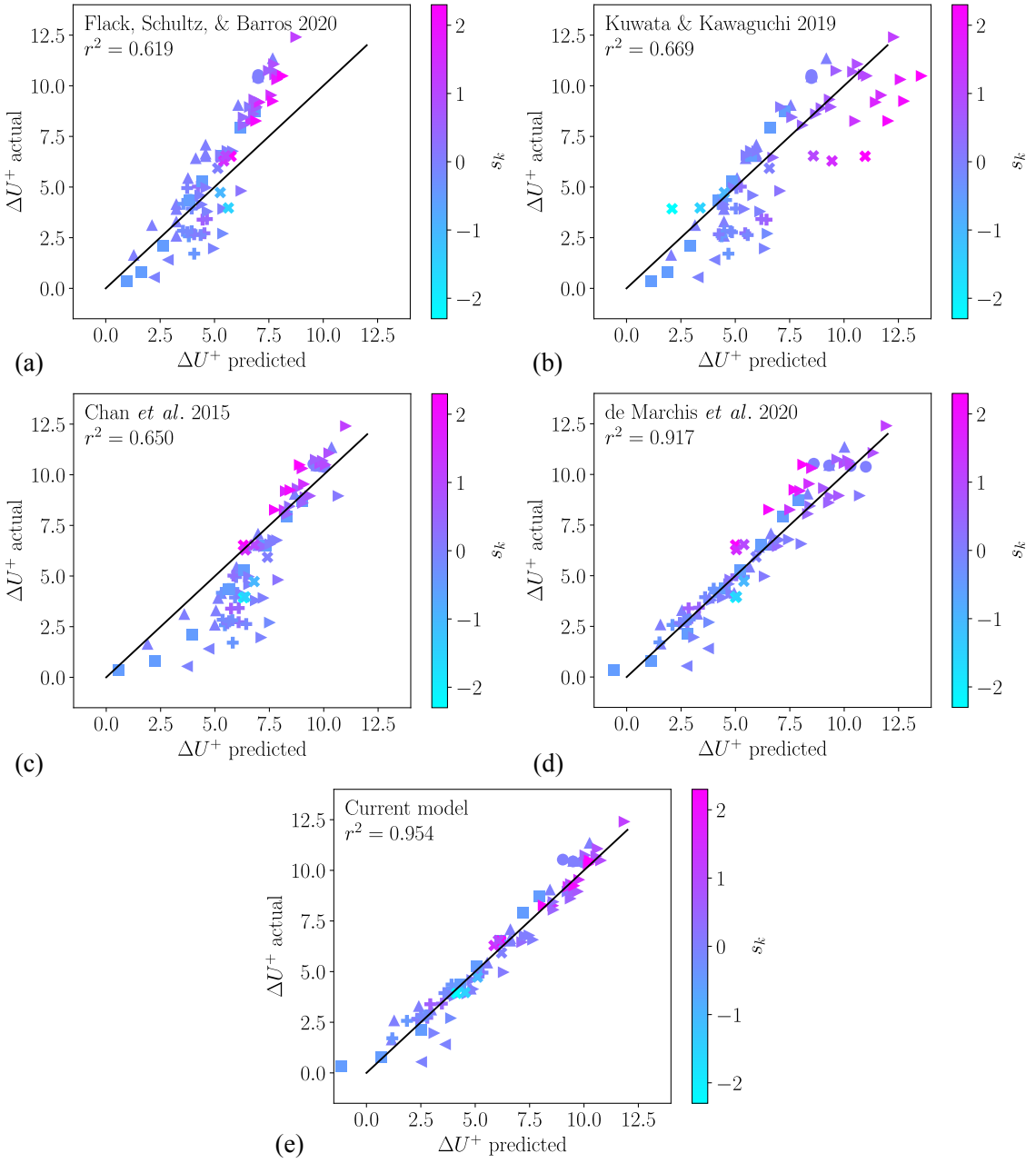

Figure 4.9: Comparison of actual ΔU^+ to predicted ΔU^+ using the DNS database with the following correlations: (a) Flack, Schultz, & Barros [39] (using Eq. 4.3 for $\Delta U^+ = f(k_s^+)$), (b) Kuwata & Kawaguchi [67] (using Eq. 4.3 for $\Delta U^+ = f(k_s^+)$), (c) Chan *et al.* [24], (d) de Marchis *et al.* [33], and (e) the current proposed model. Each figure includes a subset of r^2 also shown in Table 4.2.

Correlation	Model Form	Roughness Function	r^2
[39]	$k_s^+ = \begin{cases} 2.73k_{rms}^+ (2+s_k)^{-0.45} & \text{if} \quad s_k < 0.0 \\ 2.11k_{rms}^+ & \text{if} \quad s_k = 0.0 \\ 2.48k_{rms}^+ (1+s_k)^{2.24} & \text{if} \quad s_k > 0.0 \end{cases}$	Eq. (4.1) Eq. (4.2) Eq. (4.3)	0.540 0.536 0.619
[67]	$k_s^+ = \begin{cases} 4.0k_{rms}^+ (1+0.17s_k)^4 & \\ 2.48k_{rms}^+ (1+s_k)^{2.24} & \text{if} \quad s_k > 0.0 \end{cases}$	Eq. (4.1) Eq. (4.2) Eq. (4.3)	0.670 0.666 0.669
[24]	$\Delta U^+ = \frac{1}{\kappa}\log(k_a^+) + 1.12ES + 1.47$	N/A	0.650
[33]	$\Delta U^+ = \frac{1}{\kappa}\log(ESk_{rms}^+) + 3.5$	N/A	0.917
Proposed model	See Eq. (4.17)	N/A	0.954

Table 4.2: Comparison of the best-fit performance of selected roughness functions from the literature.

The corresponding wall-normal coordinate is then shifted by the difference in continuity locations between the smooth and rough walls, given by

$$y^* = y^+ + (y^{\dagger,s} - y^\dagger). \tag{4.19}$$

The log layer is shifted by the rough surface's roughness function ($U_{\log}^* = U^+ + \Delta U^+$), recovering the classical law of the wall function.

Figure 4.11(a) presents all the DNS data in inner units, highlighting the wide spread of profiles in the constructed database. In Figure 4.11(b), we apply the roughness transformation for the RSL as defined in Eqs. (4.18) and (4.19), and for the log layer, where $y_{\log}^* = y^+$ and $U_{\log}^* = U^+ + \Delta U^+$. The parameters a_c, ΔU_{RSL}^+, and ΔU^+ are directly extracted from the DNS database's mean velocity profiles. This represents the most optimal transformation that can be achieved based on the two-layer model form given in Eqs. (4.11) and (4.12). Given the collapse of the transformed velocity profiles with the coefficients directly extracted from the DNS, this also verifies the assumed form of the two-layer model.

Figure 4.11(c) demonstrates the complete model's effect, where velocity profiles are transformed using model fits from Eqs. (4.15), (4.16), and (4.17) with coefficient values detailed in Table 4.3. The only inputs to the model that yield the collapse in Figure 4.11(c) are the three geometric values and the Reynolds number (k_{rms}^+, ES, and s_k). Comparing Figure 4.11(b) and (c) shows only a minor spread of the velocity profiles in the log layer. The RSL spread is wider, but any inaccuracies in the modeled ΔU_{RSL}^+ will shift the profile. Nonetheless, there is good agreement with the slope

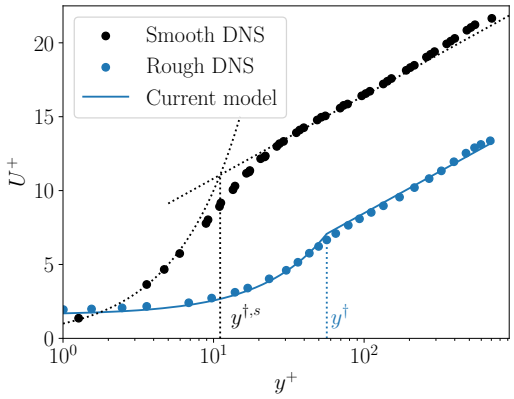

Figure 4.10: Schematic showing the example locations of the transition point between the viscous sublayer and log layer for a smooth wall, $y^{\dagger,s} \approx 11$ and the transition location between the rough-wall RSL and log layer, $y^{\dagger}$. Example channel DNS results of [110] along with the viscous sublayer profile ($U^+ = y^+$) and the log layer profile [$U^+ = (1/\kappa)\ln y^+ + B$] are included for reference.

Term	Coeff.	Value	Term	Coeff.	Value	Term	Coeff.	Value
ΔU^+	c_1	3.026	a_c	c_1	0.123	ΔU^+_{RSL}	c_1	0.799
	c_2	3.444		c_2	318.15		c_2	0.0143
	c_3	28.56		c_3	1.124		c_3	0.574
	c_4	0.0031		c_4	0.144			
	c_5	0.353		c_5	0.114			
	c_6	0.894						

Table 4.3: Fitting coefficients for the model functions.

of the profiles matching that of the smooth wall viscous sublayer. Overall, we show that the DNS data directly applied to the model form in Figure 4.11(b) provide a good collapse to the smooth-wall data, indicating that the simple model form can effectively represent this complex set of rough surfaces. Despite increased spread when applying modeled values of ΔU^+, a_c, and ΔU^+_{RSL}, a general collapse to the smooth-wall boundary layer profile is still evident. This model's ability to collapse the rough-wall boundary layer can be used to better approximate the drag on rough surfaces and can be adapted as a wall model for use in simulations of rough-wall turbulent flows.

4.2.7 Further comparison of roughness functions

In predicting ΔU^+ for the 83 rough configurations in Table 4.2.1, we only observed a small improvement using the proposed model in Eq. 4.17 compared to the one by de Marchis *et al.* [33] (Figure 4.9(d) and (e)). However, to demonstrate the proposed model's generality, we include the previously excluded 15 rough cases (excluded due to additional modeling requirements in the buffer layer, which is unrelated to the roughness function in the log layer) when comparing the present

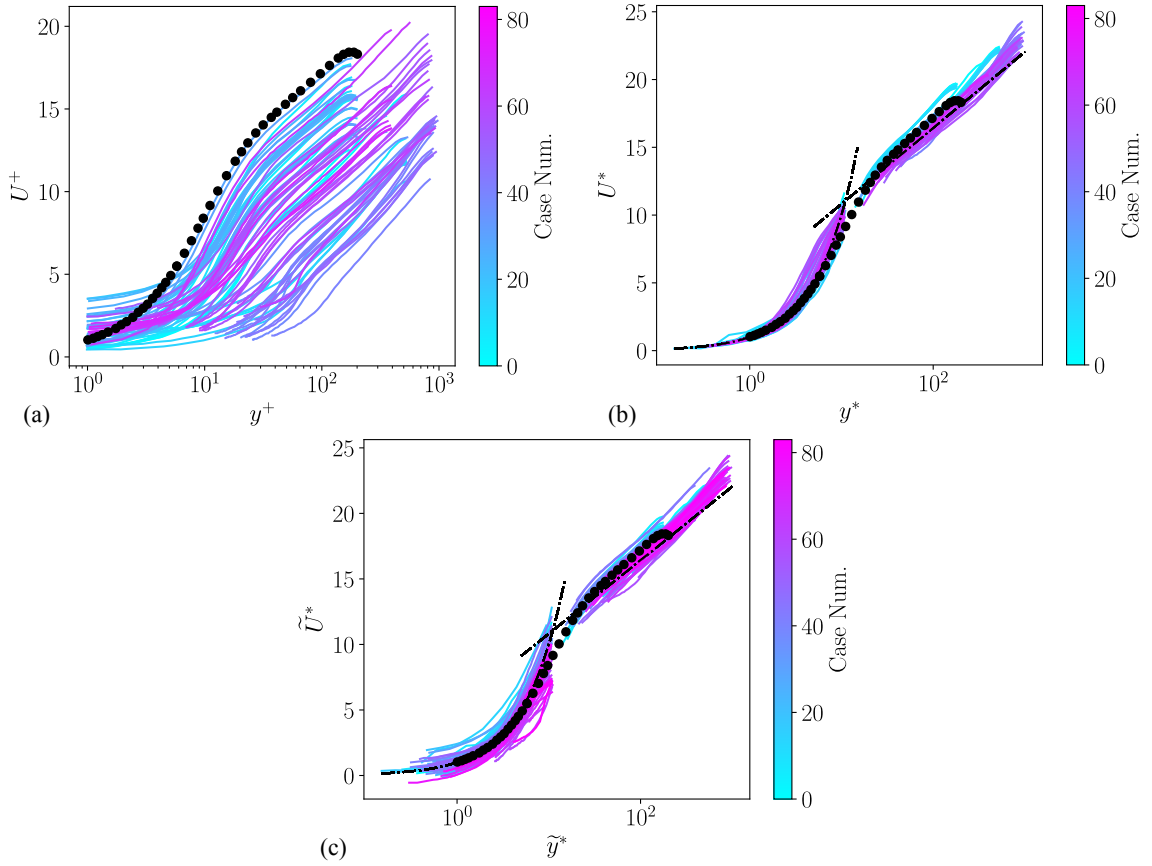

Figure 4.11: Velocity profiles for rough-wall boundary layers are presented in (a) as extracted DNS profiles, (b) as model form values obtained from DNS data for model fits and (c) as modeled data using Eqs. (4.15), (4.16), and (4.17). Additionally, we include an example smooth-channel DNS result from [109] at $Re_\tau = 180$ (denoted by ●), along with the viscous sublayer profile ($U^+ = y^+$) and the log layer profile [$U^+ = (1/\kappa)\ln y^+ + B$] for reference.

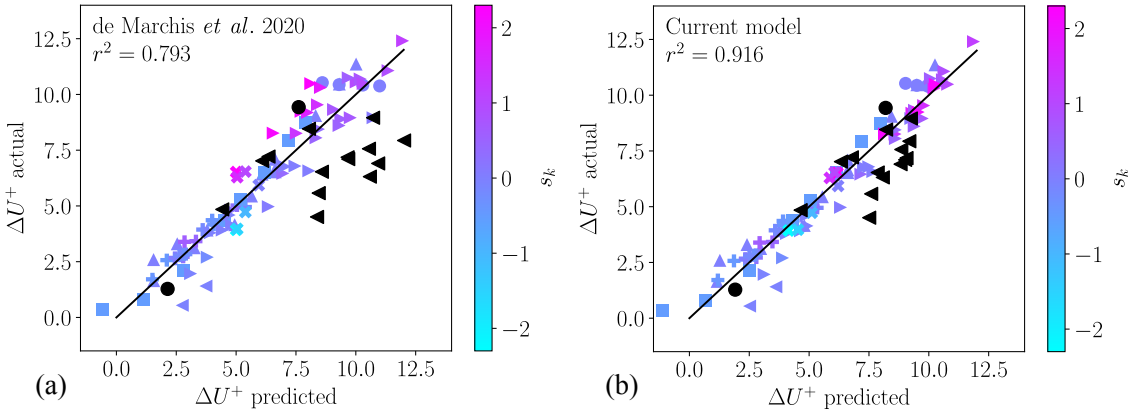

Figure 4.12: Comparison of actual ΔU^+ to predicted ΔU^+ using all 98 rough-wall cases from the DNS database comparing (a) de Marchis *et al.* [33], and (b) the current proposed model. The black symbols represent the additional cases excluded from the RSL model. Each figure includes a subset of r^2; note the difference from the values shown in Table 4.2.

model to the model of de Marchis *et al.* [33]. We directly utilize the model coefficients from Table 4.3, which were fitted without these 15 configurations.

In Figure 4.12, we plot the actual vs predicted ΔU^+ values for both the (a) de Marchis [33] and (b) present models. The inclusion of the additional configurations (shown as black symbols in Figure 4.12) alters the best fit of the de Marchis model from 0.917 to 0.793, while the best-fit correlation for the present model only drops from 0.954 to 0.916. This provides further evidence of the generality and robustness of the proposed roughness function (defined in Equation 4.17).

4.3 The KES roughness wall-model extension to the equilibrium wall model

We incorporate our new velocity transformation directly into a modification of the equilibrium wall model. We represent the mean velocity profile within the boundary layer using a two-zone approach: the first being the RSL (see Eq. 4.11) and the second being the modified logarithmic layer (see Eq. 4.12). We restate the equations in Eq. 4.20 here for clarity.

$$U^+(y^+, k^+_{rms}, ES_x, s_k) = \begin{cases} a_c y^+ + \Delta U^+_{RSL} & \text{for } y < y^* \\ \frac{1}{\kappa}\ln(y^+) + B - \Delta U^+ & \text{otherwise} \end{cases} \tag{4.20}$$

Here, a_c, ΔU^+_{RSL}, and ΔU^+ are defined by Eqs. 4.15, 4.16, and 4.17, respectively using the coefficients of Table 4.3, $\kappa = 0.41$, and $B = 5.2$. The value of y^* is then obtained through forcing C^0 continuity of the velocity profile. Enforcing C^0 continuity results in a non-linear equation for the

value y^*, where

$$\frac{1}{\kappa}\ln(y^*) + B - \Delta U^+ - a_c y^* - \Delta U^+_{RSL} = 0. \tag{4.21}$$

In contrast to the EQWM, where y^* is a derivable constant, the KES-modified EQWM requires the additional non-linear solution of Eq. 4.21 to obtain y^* at each iteration of the EQWM. From this, the height of the matching location within the first boundary adjacent element is compared to y^*, and the appropriate zone of Eq. 4.20 is applied.

The implementation of the present model solves the non-linear algebraic relation of Eq. 4.20 using a Newton-Raphson method, given an initial guess of the local shear stress. During each sub-iteration, an additional non-linear solution of Eq. 4.21 is conducted to determine whether the matching location is within the RSL or logarithmic region of the model. The model assumes that the boundary layer is larger than the roughness height, where the data from Section 4.2.1 has $\delta/k \geq 6$.

4.3.1 *A posteriori* WMLES result of a rough-wall turbulent channel flow

In this section, we simulate a rough-wall turbulent channel flow to provide validation for the KES model approach. Specifically, we employ the geometry of [110], an irregular industrial grit-blasted surface scanned using a variable focus microscope. The surface is then filtered to remove the smallest length scales (where the filter length does not modify k_{rms} by more than 8% [20]) and forced to be periodic in the streamwise and spanwise directions. Additional details of the geometry preparation can be found in [20] and [109]. An example image of the rough topology can be seen in Figure 4.1(b). We denote the streamwise, spanwise, and wall-normal directions as x, z, and y, respectively. The friction-based Reynolds number, $Re_\tau = u_\tau \delta/\nu = 720$, where δ represents the channel half height. This Re_τ results in a value of $k^+_{rms} = 25.776$. Additionally, $ES_x = 0.2339$ and $s_k = -0.519$. The scaled roughness height results in $k/\delta = 1/6$, which was shown to be small enough to collapse the mean flow of the outer layer in [20]. Streamwise, L_x, and spanwise, L_y, lengths are 5.63δ and 2.815δ respectively. For all accompanying plots, $y = 0$ is the location of the average roughness height of the rough surface. A series of grid resolutions are simulated where each grid has uniform spacing where the cell size, $\Delta = 2\delta/(N_p\sqrt{3})$, ensures that the packing is ideal in the periodic directions where N_p/δ is the number of points in the channel half height. While mean profiles are provided in [110], Reynolds stresses remain absent. Therefore, a precursor simulation is conducted at the DNS limit to facilitate comparisons of the Reynolds stresses. In Figure 4.13, we compare the newly acquired DNS profiles to those obtained in [110]. We observe excellent agreement with the previous DNS results. The average y^+ along the roughness surface is less than one everywhere with 320 points per channel half height, leading to $1800 \times 900 \times 640$ cells in the streamwise, spanwise, and wall-normal direction respectively ($\sim 1B$ total control volumes). In contrast to [110], this is done with isotropic hexagonally close-packed body-fitted meshes with no grid stretching.

A comparison of the mean velocity profiles between the EQWM and KES models for a series of

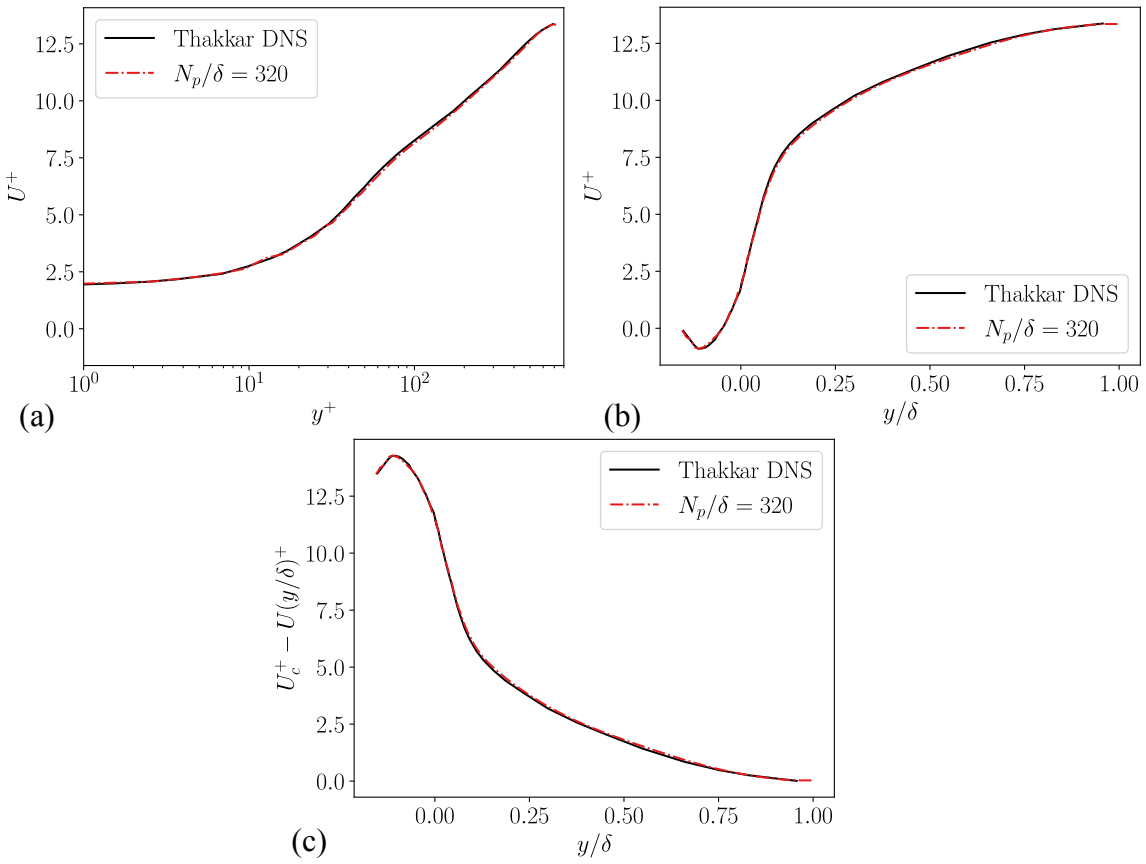

Figure 4.13: Comparison of (a) mean inner-scaled velocity profile, (b) outer-scaled velocity profile, and (c) velocity defect profile of the DNS rough channel surface (red line, where N_p/δ is the number of points per channel half height) to the previous work of [110] (black line).

grid resolutions is shown in Figure 4.14. The data is plotted using three approaches: inner-scaled, $y^+ = yu_\tau/\nu$ (Figure 4.14(a,b)), outer-scaled, y/δ (Figure 4.14(c,d)), and velocity defect (Figure 4.14(e,f)). The three left figures (a,c,e) are the results with the EQWM, and the three right figures (b,d,f) are the results with the KES model. It is observed that at each grid resolution, the KES model is closer to the DNS data. Specifically, good agreement is achieved at very coarse resolutions with unresolved roughness features. Even at $N_p/\delta = 20$, the number of elements per roughness height is approximately one. The additional sub-grid stress applied from the KES model assists in achieving better representations of the velocity profile at coarse resolutions. Indeed, we even observe an improved response in the Reynolds stress and turbulence intensities. Figure 4.15(a) and 4.16(a) plot the Reynolds stress for the EQWM and KES models, respectively. The finest resolution underpredicts the stress in the region of the flow above the roughness elements. This underprediction is removed after applying the additional stress from the KES model (Figure 4.16, indicating an indirect improvement for the fluctuations. Although the KES model improves turbulent intensity values (Figures 4.15(b,c,d) and 4.16(b,c,d)), the discrepancy compared to the DNS results persist, highlighting a limitation in capturing turbulence characteristics beyond mean flow properties, as is often observed in wall-modeled approaches.

4.3.2 *A posteriori* WMLES result of a NACA23012 airfoil under rime ice conditions

In Figure 3.20, it was shown that using the standard practices established in Chapter 3 resulted in a large over-prediction of the early-time rice ice geometry's (see Figure 3.1(a)) lift coefficient and a prediction of a delayed stall angle. Using an additional level of refinement improved the results but still incurred an overprediction of lift and delayed stall angle. Here, we revisit the early-time rime ice condition to test the effectiveness of the KES model for this geometry both in a pre- and post-stall angle of attack. For the pre-stall angle of attack, the chord normalized span is $S_p = 0.15c$. At the post-stall angle, we choose to simulate the entire span of the wind tunnel, where $S_p = 1.86c$, given the conclusions for non-physical stall behaviors in both Figures 3.12 and 3.16(d) when using a restricted span. Therefore, at the post-stall angle ($\alpha = 13^\circ$), the side walls are modeled with inviscid wall conditions, which is equivalent to the treatment of the top and bottom walls in Chapter 3. Other than where stated, the setup from Section 3.4 is used. A series of grids are used to simulate the rime ice geometry. The details of each grid are described in Table 4.4. When applying the KES model, an averaged value for the roughness properties is applied to the entire rough region with $k_{rms} = 1.22 \times 10^{-4}$, $ES_x = 0.19$, and $s_k = 0.027$. The rest of the airfoil uses the standard EQWM. It is necessary to delineate between specifying the EQWM and KES model, as the KES model is only valid at rough surfaces and does not recover the smooth wall limit exactly at $k_{rms} = 0$ or ES=0.

In Figure 4.17, we compare the series of grids for both the EQWM and KES model at $\alpha = 8^\circ$ and

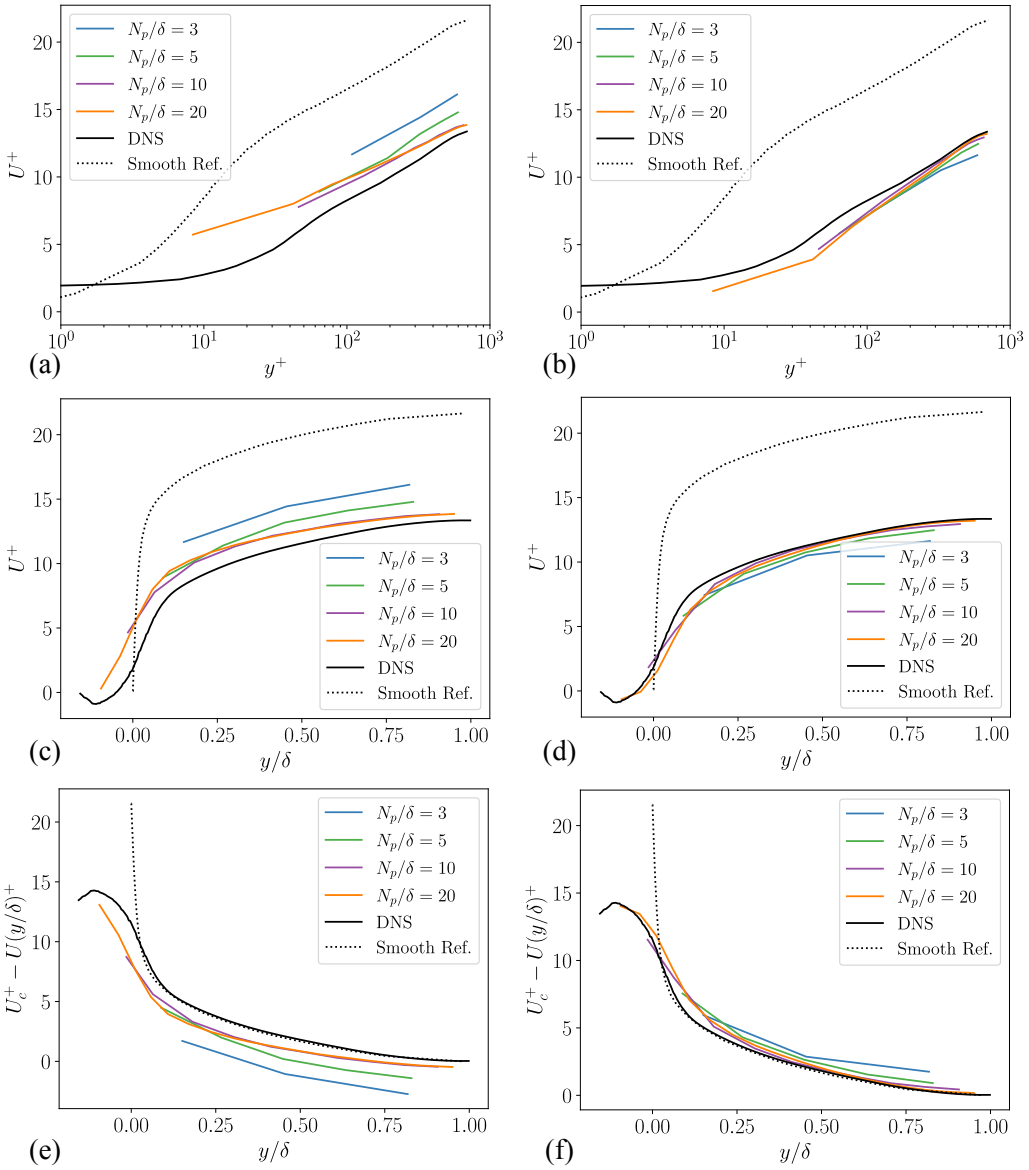

Figure 4.14: Mean velocity profiles plotted in inner-units (a,b), outer-units (c,d), and defect-units (e,f) for the EQWM (a,c,e) and the KES model (b,d,f) for grid resolutions, $N_p/\delta = 3, 5, 10,$ and 20, compared to DNS and a reference smooth wall DNS [60]. The *RMS* roughness height per cell size, k_{rms}/Δ, are approximately 0.093, 0.16, 0.31, and 0.62 respectively for the 3, 5, 10, and 20 points per channel half height respectively.

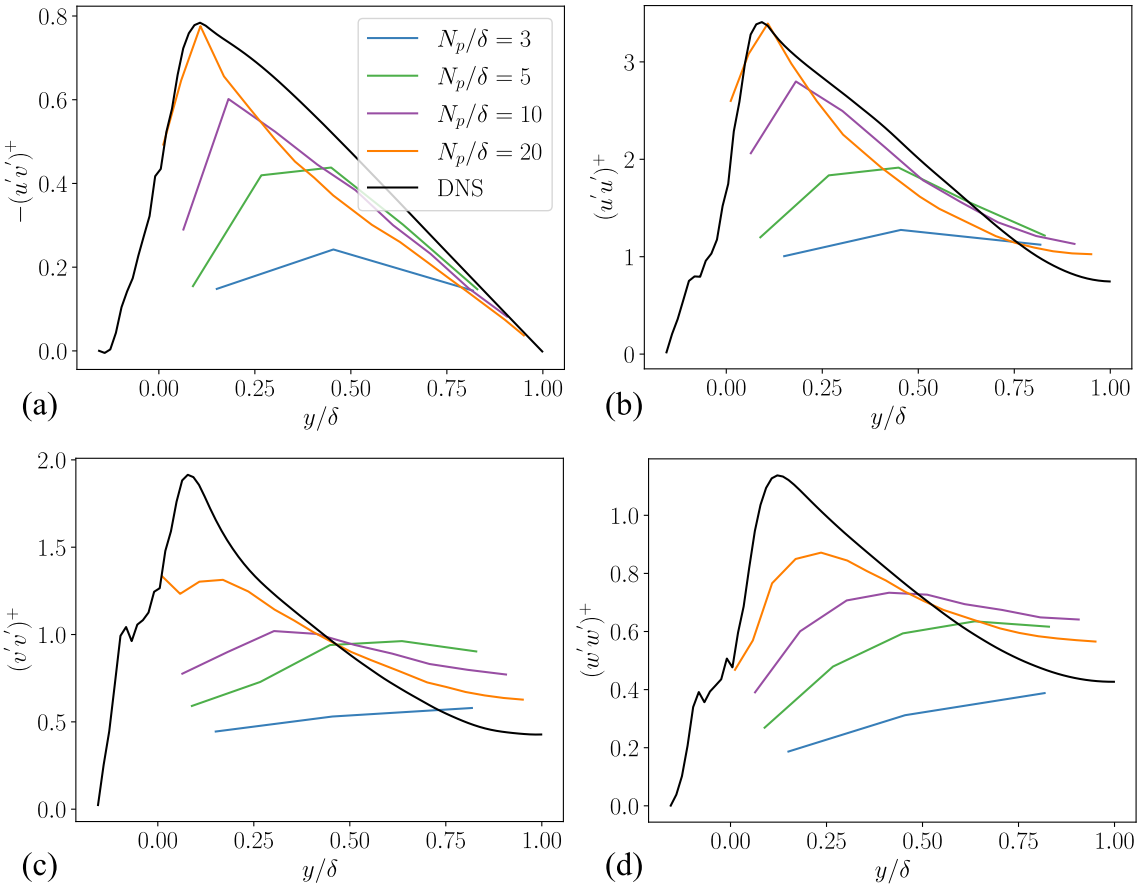

Figure 4.15: Reynolds stress and turbulence intensities for different grid resolutions, $N_p/\delta = 3, 5, 10,$ and 20, compared to DNS for the EQWM.

Angle of attack (α)	Ref. Level	Cell count (M CV)	S_p	k_{rms}/Δ_{min}
8°	Coarse	1.3	0.15	0.16
	Medium	4.6		0.32
	Fine	17.4		0.63
13°	Coarse	18.7	1.86	0.16
	Medium	69.9		0.32
	Fine	270		0.63

Table 4.4: Grid refinement details for the rime ice geometry at two angles of attack comparing refinement levels; cell counts in millions of control volumes (M CV); chord normalized spanwise extent (S_p); points per root-mean-square roughness height (k_{rms}/Δ_{min}), where Δ_{min} is the minimum grid length scale.

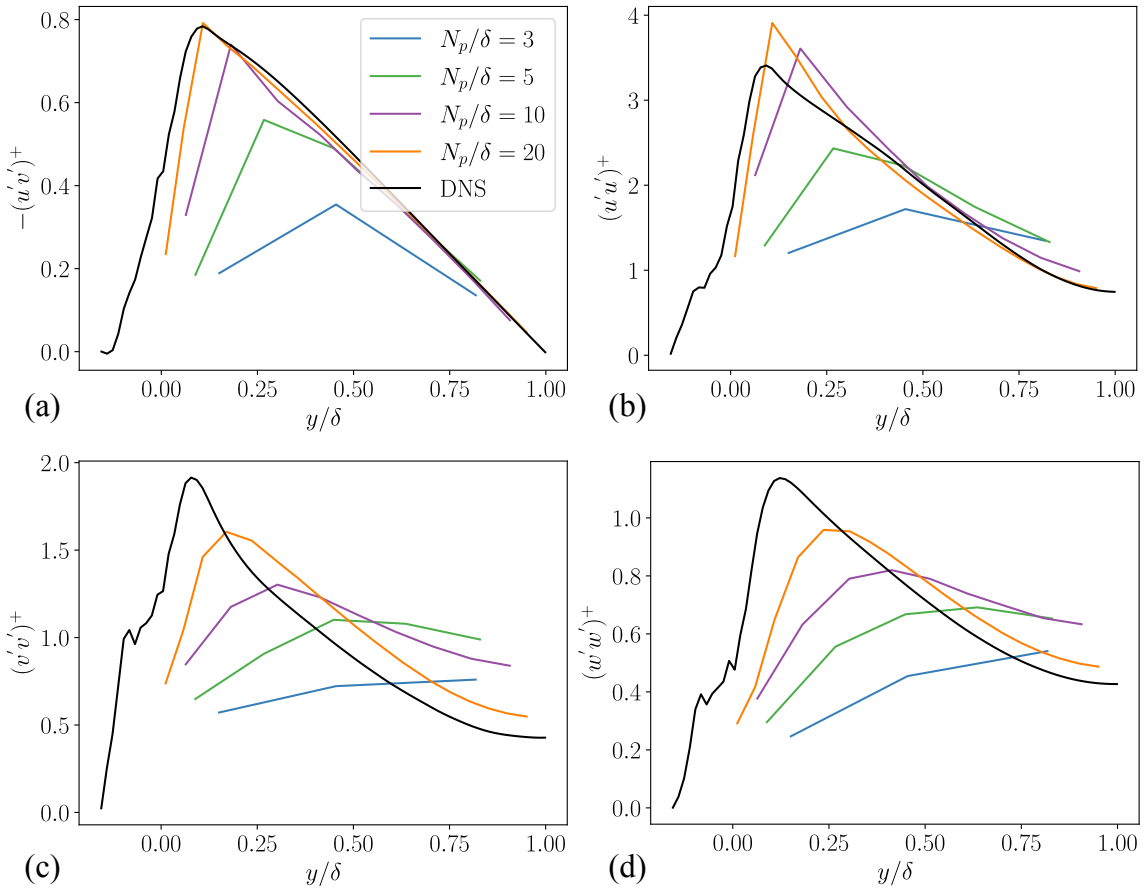

Figure 4.16: Reynolds stress and turbulence intensities for different grid resolutions, $N_p/\delta = 3, 5, 10,$ and 20, compared to DNS for the KES model.

α	Model	ΔC_L	$\epsilon_L(\%)$	ΔC_D	$\epsilon_D(\%)$
8°	EQWM	0.051	5.25	0.0038	19.21
	KES	0.021	2.12	0.0014	7.26
13°	EQWM	0.473	51.1	0.1381	79.63
	KES	0.042	4.56	0.0340	19.59

Table 4.5: Error reduction for integrated forces comparing EQWM and KES models.

$\alpha = 13^\circ$ by comparing values of C_p to the experimental data of [15]. For $\alpha = 8^\circ$ (Figure 4.17(a,b)), we observe minimal variation in C_p with increasing grid resolution. The inclusion of the KES model results in only slight modifications to the C_p curve. Still, it does improve upon the integrated quantities as shown in Table 4.5 through the improved prediction of viscous drag, which defines the error in lift and drag coefficients for both approaches. In contrast, we observe a marked difference in the solutions between the EQWM and KES model at $\alpha = 13^\circ$. With the EQWM, regardless of mesh resolution, no solution results in a stalled airfoil. This is in contrast to the experimental results of [15], where this angle is the first post-stall angle of attack. When the KES model is applied, the solution is found to stall at the medium and fine grid resolutions.

Further refinement leads to even more improvement. In Figure 4.18, C_p profiles for both the EQWM and KES model at the fine grid resolution are compared for both the pre-and post-stall angles of attack (Figure 4.18(a) and (b) respectively). Again, only minimal changes are observed in the pre-stall α, but at post-stall, we observe a large reduction in the overprediction of suction near the leading edge as well as a flattening of the C_p curve downstream of $x/c = 0.25$ indicative of a stalled airfoil.

Instantaneous snapshots of iso-surfaces of Q-criterion colored by streamwise velocity are shown in Figure 4.19 near the leading edge of the airfoil. The application of the KES model results in additional turbulent structures as well as an upstream shift in the transition location. This is reflected in Figure 4.20, where a zoomed-in look at the friction coefficient, C_f, reveals a local increase in the near wall stress. This increase in stress is representative of the sub-grid stress contribution added via the KES model. The small discontinuity seen in the KES model results of Figure 4.20 is due to the local change in the boundary condition, which modifies the post-processing of the C_f curve. Figure 4.21 shows the response of the integrated forces to the KES model. Minimal improvements are observed at $\alpha = 8^\circ$ in both lift and drag coefficients. The moment coefficient is slightly over-predicted as compared to the EQWM result. This can occur with slight deviations of where the lift is generated across the airfoil. The significant improvements observed at $\alpha = 13^\circ$ underscore the potential of the KES model to accurately represent challenging post-stall conditions for iced airfoils.

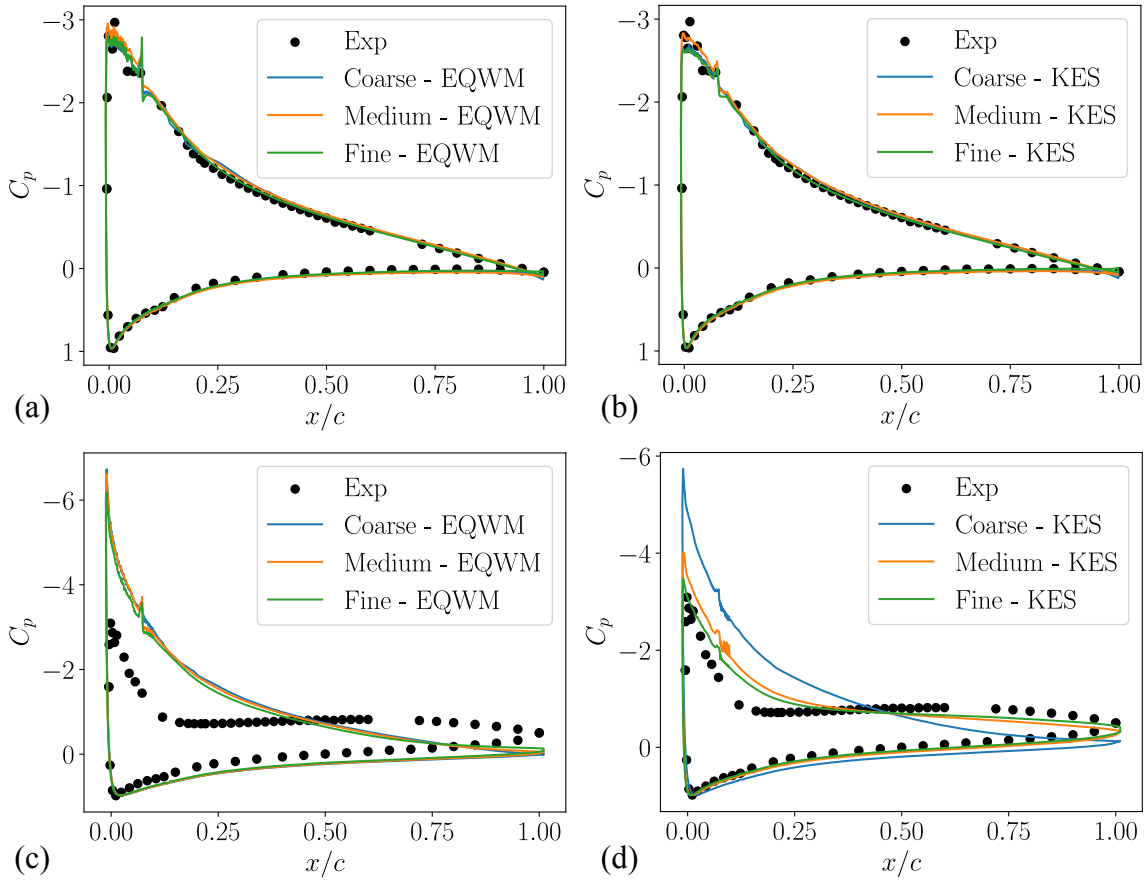

Figure 4.17: Comparison of pressure coefficients, C_p at $\alpha = 8^{\circ}$(a,b) and $\alpha = 13^{\circ}$(c,d) between the EQWM (a,c), KES model (b,d), and experimental results of [15].

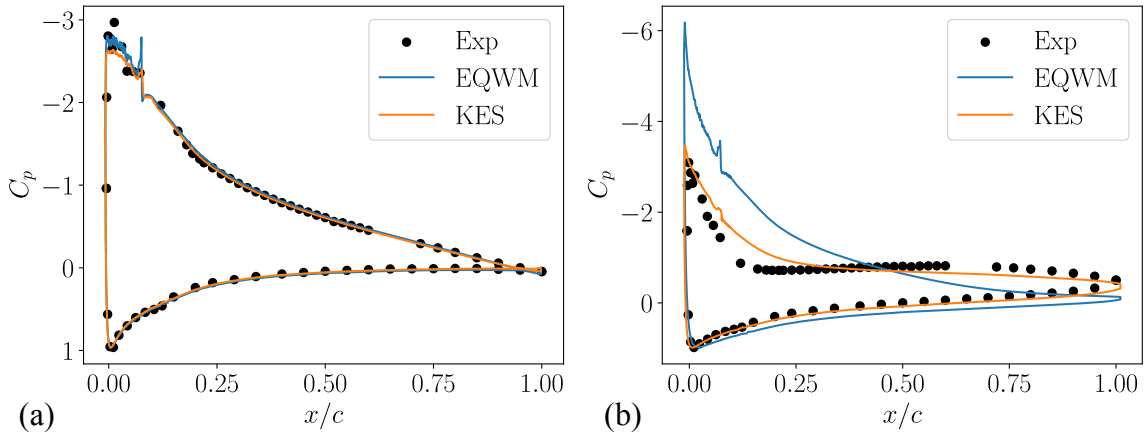

Figure 4.18: Comparison of fine grid pressure coefficients, C_p at $\alpha = 8^{\circ}$(a,b) and $\alpha = 13^{\circ}$(c,d) between the EQWM (a,c), KES model (b,d), and experimental results of [15].

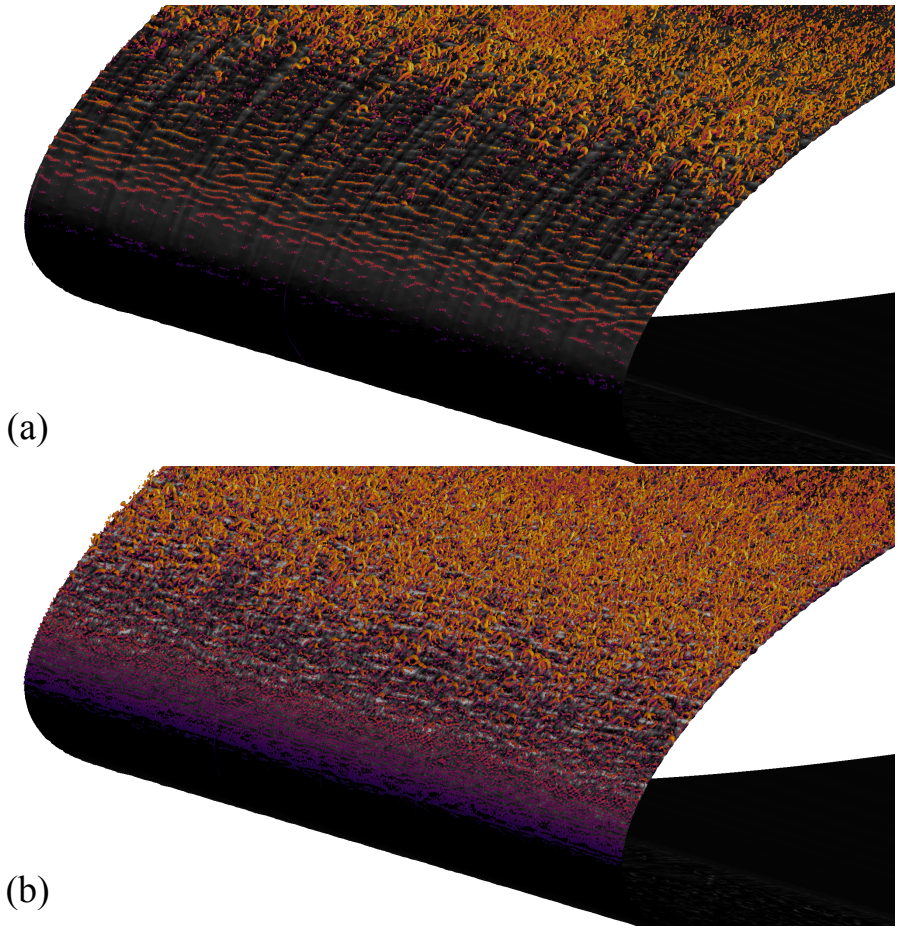

Figure 4.19: Iso-surface of Q-criterion colored by streamwise velocity for the $\alpha = 8^{\circ}$ rime ice condition with the (a) EQWM and (b) KES models at the fine grid resolution.

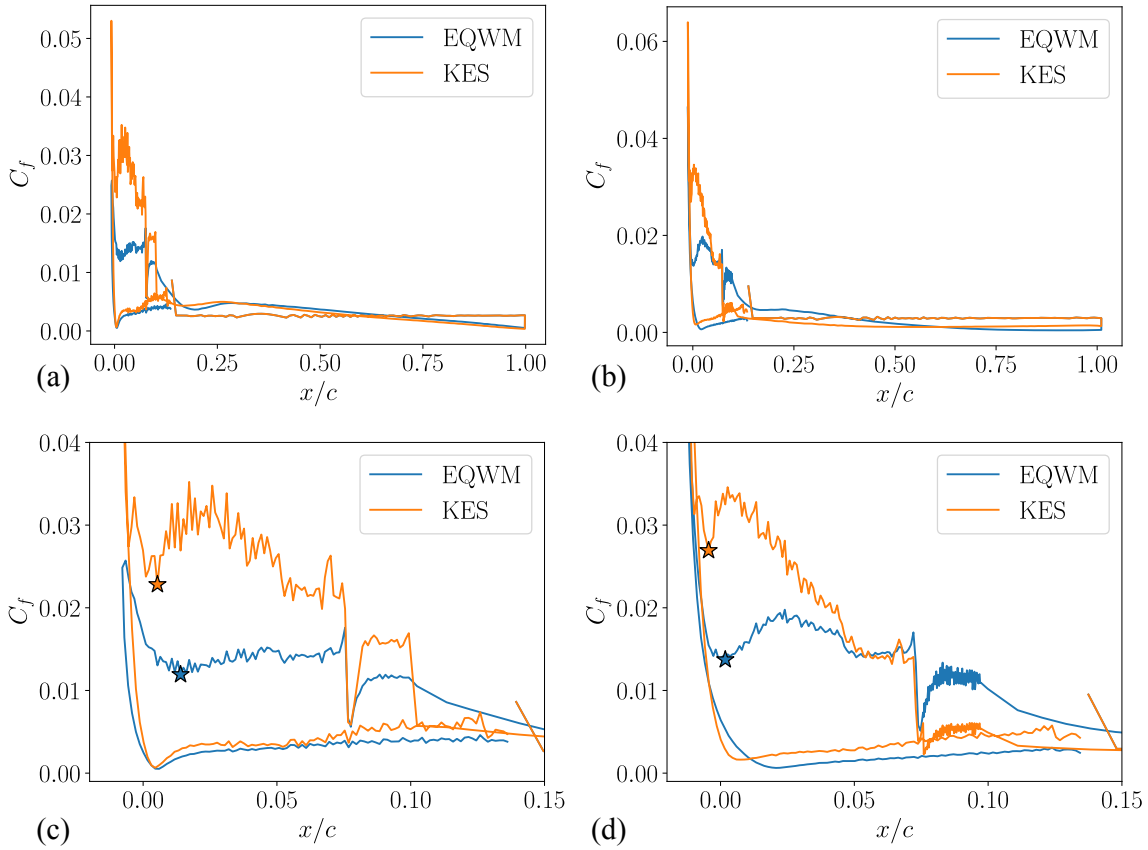

Figure 4.20: Friction coefficient comparison (C_f) at $\alpha = 8^\circ$ (a, c) and $\alpha = 13^\circ$ (b, d) using the EQWM and KES model. Panels (a, b) include the full geometry, while panels (c, d) focus on the leading edge of the airfoil.

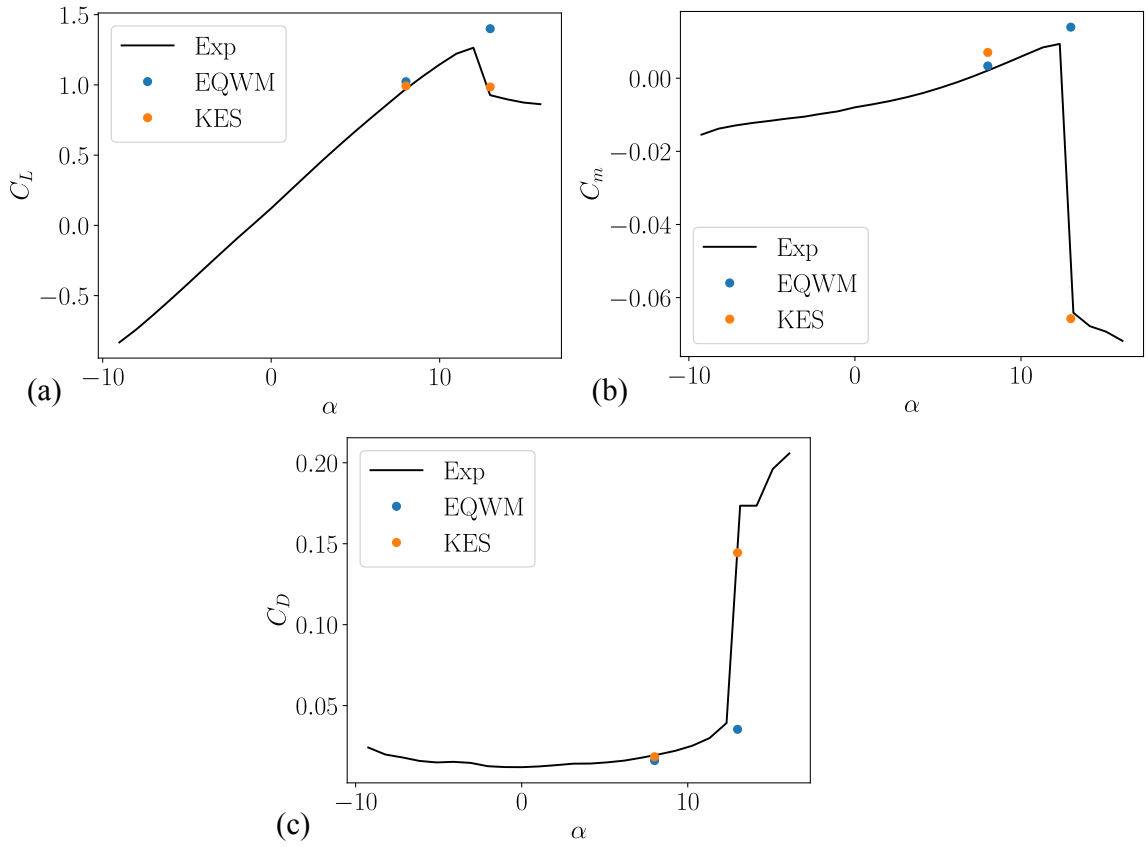

Figure 4.21: (a) Lift (C_L), (b) moment (C_M), and (c) drag (C_D) coefficients comparing the EQWM and KES model at the fine grid resolution for the rime ice geometry to the experimental data of [15].

Surface	k_{rms}	ES	s_k
Suction side	1.046×10^{-4}	0.179	-0.021
Pressure side	1.341×10^{-4}	0.258	0.175

Table 4.6: Averaged roughness parameters for surface sections of the KES model applied to the rime ice geometry.

4.3.3 Comparison to WRLES data with boundary condition sensitivities

In addition to the experimental data of [15], we have run a single angle of attack WRLES of the $S_p = 0.15c$, $\alpha = 8^\circ$ condition. Details of this WRLES and its comparison to a WRLES calculation of the clean NACA23012 airfoil are included in Appendix A. Here, we utilize it to compare the validity of three different modeling approaches for the rime ice case: the EQWM, the KES model with averaged properties over the whole ice shape, and the KES model with averaged properties in sections of the ice shape. The first two are repeated cases from Section 4.3.2 while the latter introduces additional geometric information from the rime ice shape itself. In Figure 4.22, we delineate four different boundary condition regions, namely, the suction (upper) rime ice surface, the pressure (lower) rime ice, the leading-edge, where the slope of the roughness is near zero and therefore, treated as smooth with the EQWM, and the fasteners used to mount the leading edge also modeled with the EQWM. In this configuration, the suction and pressure sides of the roughness each have their own averaged roughness properties, as shown in Table 4.6. In the modeled cases, we compare using the fine grid reported in Table 4.4.

Figure 4.23 compares C_p data between the different cases. Only minimal differences can be observed in Figure 4.23(a), but when zoomed into the leading edge [Figure 4.23(b)], we observe that both the KES and KES with split boundary conditions are in closer agreement to the WRLES as well as the experimental data [15], and have little sensitivity between themselves.

We then compare the C_f values zoomed into the leading-edge of the airfoil in Figure 4.24. In comparing the models to the WRLES, we observe that both KES approaches have an earlier transition event (denoted by the stars), which is closer to the WRLES result. The leading-edge peak is much higher for the two KES approaches which is to be expected as our model is tuned to augment a turbulent boundary layer. After transition, both the KES approaches slightly overpredict the peak C_f but follow the appropriate shape (i.e., the increase followed by a decrease in C_f) of the C_f profile. This is not unexpected as we have not tuned this model to the specific ice in this shape but rather to a large database of roughness, making it applicable to a broader range at the cost of individual surface accuracy. In contrast, the EQWM does not have a local peak in the leading edge. The KES with split BCs provides slight improvements compared to the fully averaged properties of the KES approach. This is important as it shows that the inclusion of additional surface information does indeed improve the model's response. We observe this, particularly at the fastener location ($s/c > 0.075$ and $s/c < 0.1$), where the split BC approach is much closer to the WRLES. While

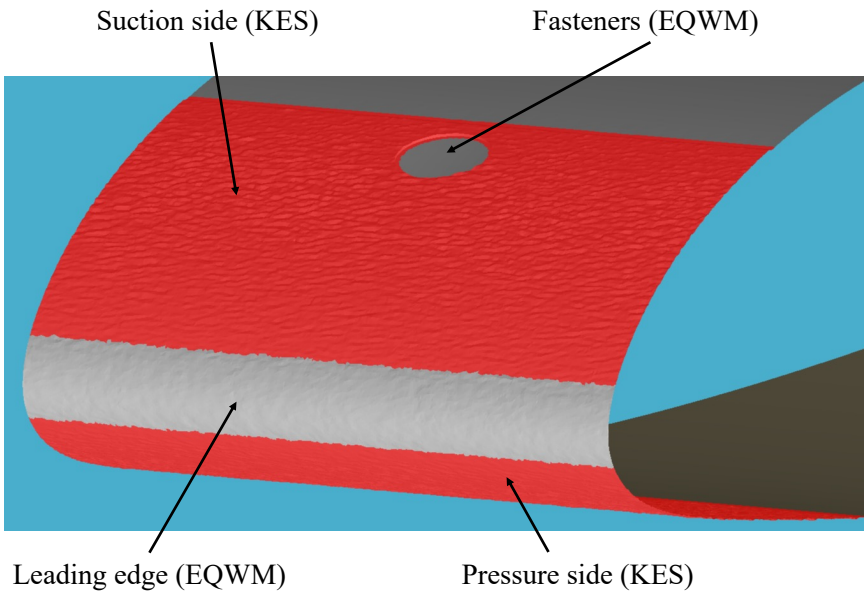

Figure 4.22: Schematic showing the boundary condition assignment for the rime ice geometry using both the EQWM and KES models. Roughness parameters for the KES model on the suction and pressure sides are listed in Table 4.6.

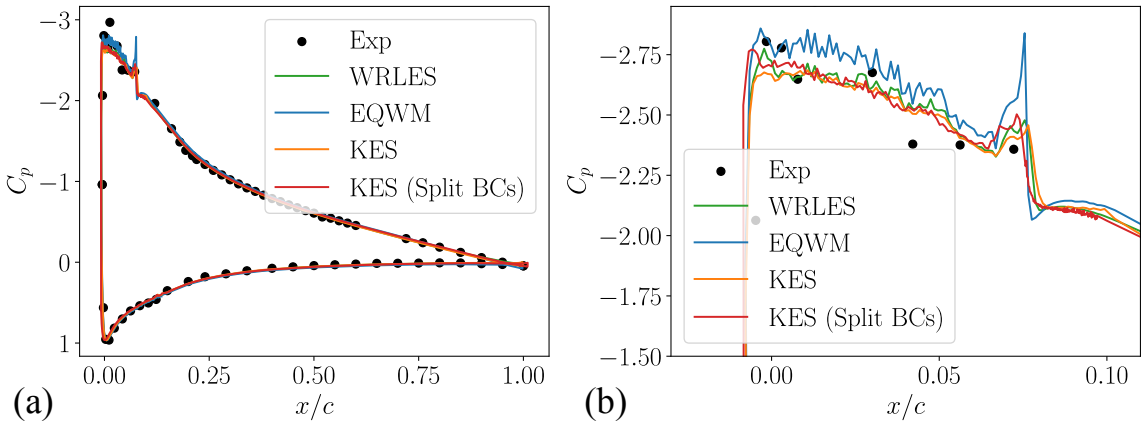

Figure 4.23: Comparison of pressure coefficients, C_p at $\alpha = 8^{\circ}$ between the WRLES, EQWM, KES, KES with split boundary conditions, and experimental results of [15]: (a) full airfoil (b) zoomed in at leading-edge.

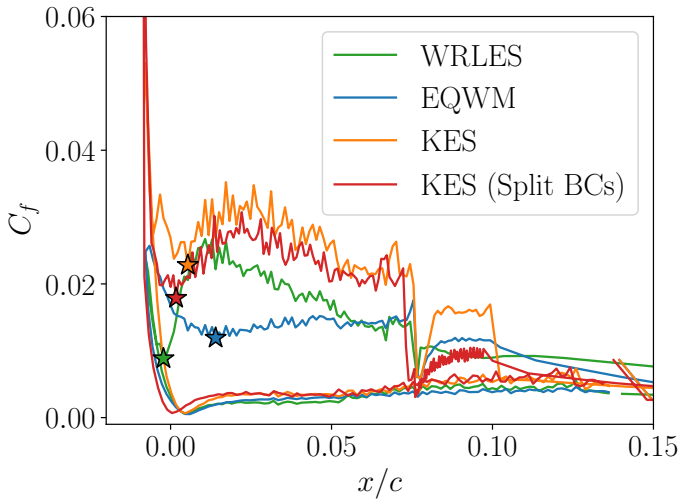

Figure 4.24: Sensitivity of friction coefficients (C_f) for the rime geometry at $\alpha = 8°$ with the WRLES, EQWM, KES, and KES split boundary condition models.

the modeling of the rime ice is a local event, we expect the flow to respond downstream to these different approaches. In Figure 4.25, we plot velocity profiles extracted from the centerline of the airfoil at several s/c positions. Each case uses uniform sampling in the normal direction of the wall and is plotted with the streamwise velocity normalized by U_∞. For all profiles, we observed improvements when utilizing either KES model approach. In regions closer to the wall, the increase in local shear stress has an increased drag effect that can be visually observed in the viscous layer for Figure 4.25(a) and persists into the outer layers further downstream on the airfoil as seen in Figure 4.25(b).

In Section 4.3.2, we observed a marked improvement in the prediction of stall. While running the full span high angle of attack with WRLES is computationally prohibitive, we can extract information on incipient separation in the current $\alpha = 8°$ results via the Clauser parameter ($\beta = \delta/\tau_w dP/ds$) [30]. As the Clauser parameter grows, the more likely the flow is to separate, therefore capturing features such as stall require an accurate prediction of β. In Figure 4.26, we compare the local streamwise value of β between the WRLES, the EQWM, and both KES model approaches. We observe an overall improvement when using the KES models throughout the region downstream of the roughened rime ice surface. At the trailing edge, we observe errors of 6.8%, 5.9%, and 1.5% for the EQWM, KES, and KES split BC models. This observation shows that obtaining the accurate upstream behavior from the rough surface has history effects on the overall flow field, which are captured through the use of the KES model.

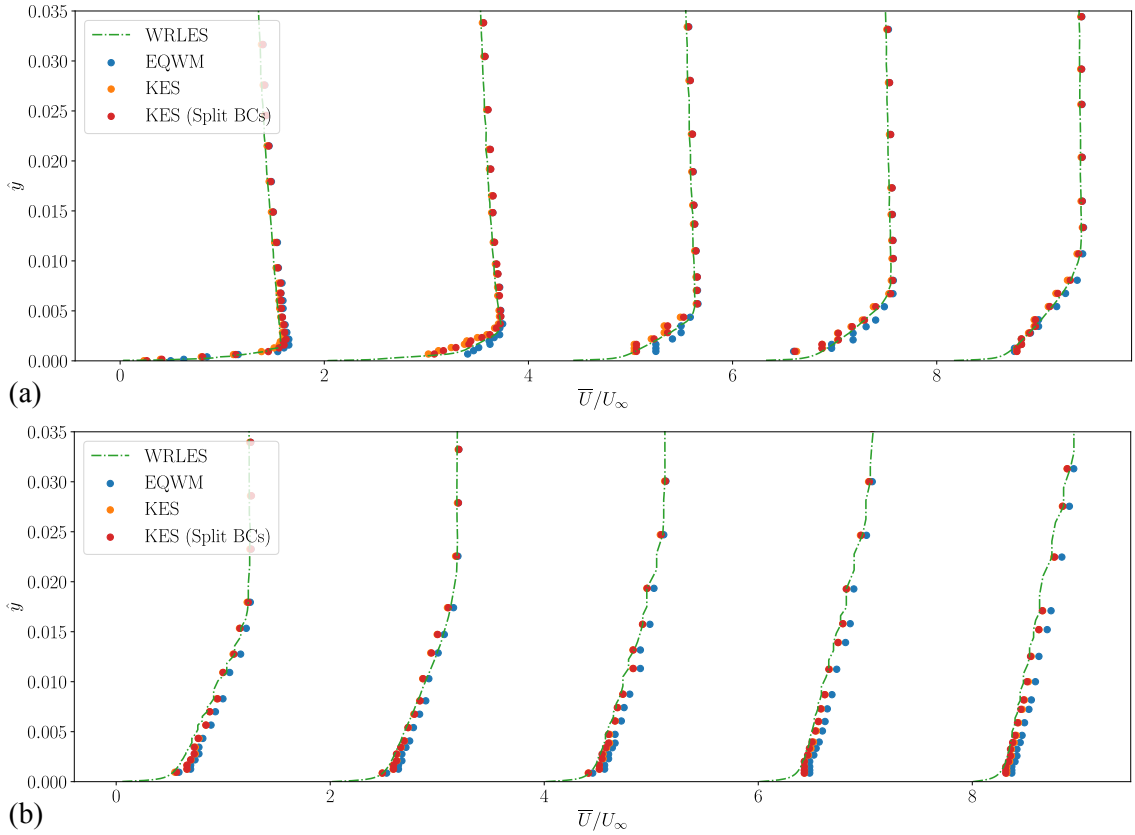

Figure 4.25: Profiles of mean streamwise velocity plotted normal to the wall ($\hat{y}$) at (a) $s/c = 0.05, 0.1, 0.15, 0.2, 0.3$ and (b) $s/c = 0.5, 0.6, 0.7, 0.8, 0.9$ with an offset of two for each profile.

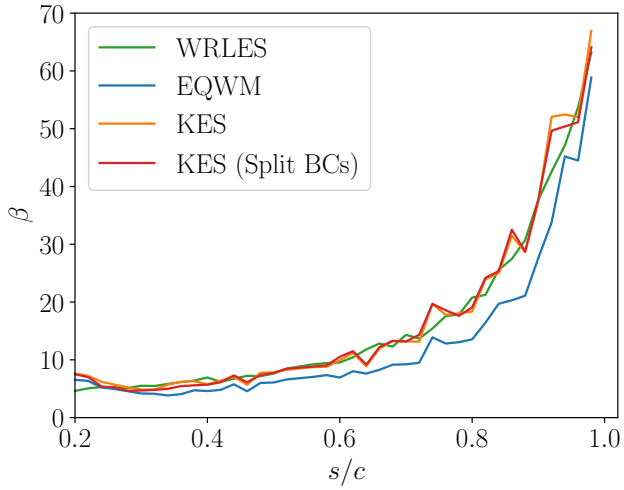

Figure 4.26: Comparison of the Clauser parameter ($\beta = \delta/\tau_w dP/ds$) as a function of streamwise coordinate between the WRLES, EQWM, and both KES model approaches.

4.4 Summary

In this chapter, we present a novel velocity transformation for turbulent flows over rough walls and its extension as a wall model for *a posteriori* simulations, leveraging a set of rough-wall geometric parameters: k^+_{rms}, ES and s_k. We construct a DNS database to characterize the modification to the classical smooth-wall boundary layer. In the roughness sublayer (RSL), we adopt a constant shear stress approximation motivated by the observed linearity in most roughness sublayers. This model, coupled with the log-layer shift, enables the parameterization of the rough-wall boundary layer profile using three key terms: the log-layer shift or roughness function, ΔU^+, the slope of the velocity in the near-wall RSL, a_c, and the velocity at the arithmetic mean of the rough surface, ΔU^+_{RSL}. We parameterize each of these terms using a minimal set of geometrical roughness characteristics. Correlations between the variables are identified and used to construct model functions to fit the available data. Comparisons between the spread in the DNS data, the model form, and the modeled transformation demonstrate a reasonable collapse across all considered roughness configurations. The transformation is then used as a modification to the EQWM, called the KES model, and is tested on a rough-wall turbulent channel flow and the early-time rime iced airfoil. Lastly, we introduce a pre-stall angle WRLES to provide additional comparisons between the tested models. In particular, it was shown that the KES approaches were able to accurately represent downstream effects, such as the Clauser parameter (β), that govern the separation behaviors of this airfoil. This approach provides a practical and effective means to predict turbulent flows over a range of rough-wall surfaces and, for the first time, demonstrates the RSL collapse across a wide variety of roughness topologies.

Chapter 5

On the use of an artificial ice shape for WMLES in aircraft icing[1]

5.1 Background

Recent experimental campaigns conducted in the Icing Research Tunnel (IRT) at the NASA Glenn Research Center have created a database of complex ice shapes for three-dimensional (3D) lifting bodies such as swept wings [16]. The introduction of wing sweep can lead to additional 3D ice shapes such as "scallops" or "lobster tails." Figure 5.1(a) shows example ice structures from the IRT, which includes wing sweep. In [18], wind-tunnel testing for the 8.9% and 13.3% scale semispan wing model based on the common research model (CRM) airplane configuration [91, 92, 113, 114] was conducted with several variations of ice shapes, both real (shapes constructed directly from laser-scanned data) and artificial (modeled ice shapes to mimic the real ice shapes' aerodynamic effects). In artificial ice shapes, simplifications to the real ice shapes are made to remove any small-scale roughness effects. For swept-wing geometries, this also includes the removal of large-scale features, such as the individual ice "scallops". Figure 5.1(b) and (c) show an example of the CRM swept wing in the Wichita State University and ONERA F1 wind tunnels, respectively. This study found that the artificial ice shapes could replicate integrated quantities, such as lift (C_L), drag (C_D), and moment (C_M) coefficients, of the real ice shapes. However, it was noted in [18] that while integrated forces are representative of the real-ice shape, large differences in the pressure coefficients (C_P) indicate different flow patterns. A cancellation of differences between the two flow fields' pressure profiles led to a match in the integrated quantities (e.g., lift and drag). The flow field for lower angles of attack had large regions of streamwise vorticity in the real ice geometry, which was absent in the artificial

[1] This Section contains previously published work, adapted here with modifications, from the following reference: Bornhoft, B., Jain, S. S., Bose, S. T., & Moin, P. (2024). "Large-eddy simulations of the CRM65 swept wing under real and artificial icing conditions", In AIAA SCITECH 2024 Forum, 1336.

ice shapes. These ice shapes and wind tunnel results act as a database for validating computational models and tools, such as those described in this work.

In addition to validating WMLES for both real and artificial ice shapes, we identify additional complexities introduced to the modeling framework when using smoothed artificial ice shapes. These ice shapes are, in part, designed to accommodate the gridding practices of a majority of CFD solvers. Using the Voronoi meshing method, we simulate both ice shapes and investigate the robustness of the simulation's accuracy to both grid resolution as well as appropriate local boundary conditions. This work underscores the challenges of modeling artificial ice shapes using state-of-the-art simulation approaches. We emphasize the importance of incorporating appropriate roughness scales into artificial or predicted ice shapes to ensure practical computational costs for the application of WMLES in iced aircraft configurations.

In this chapter, two ice shapes are considered: a detailed laser-scanned geometry constructed from the IRT data (hereafter referred to as 'real-ice') and a smoothed version of the real ice, derived by constructing the maximum combined cross-section of the 3D ice accretion along spanwise sections of the wing to mimic the effects of the real ice with a simpler geometry (hereafter referred to as 'artificial-ice'). The objectives of this study include: (a) validate WMLES approaches for the simulation of both the real and artificial ice shapes through comparison to experimental C_L, C_D, C_M, and C_P, (b) compare the flow structures, and (c) evaluate the effectiveness of using artificial-ice shapes as a surrogate for real-ice shapes in the context of WMLES.

The chapter is organized as follows. Section 5.2 details the setup for the simulations. A discussion of the computational results for the real and artificial ice shapes using the established best practices of Chapter 3 is provided in Sections 5.3.1 and 5.3.2. We then detail the difficulties of using artificial ice shapes with WMLES in 5.3.3 where we show the necessary steps to accurately represent the artificial ice shapes. A brief exploration into these ideas as we push to flight Reynolds numbers is then provided in 5.3.4. Lastly, a summary of the study and important conclusions are discussed in Section 5.4.

5.2 Computational Setup

The cases simulated are based on the CRM65 geometry first designed and tested by [91, 92, 113, 114]. To construct the relevant ice shapes, three IRT models for the inboard, mid-board, and outboard sections were tested with ice accretion by [23]. These were then laser-scanned, reconstructed, and combined to create the ice shape for the entire wing [23]. This was done as the entire swept wing could not be scaled appropriately within the IRT while maintaining correct accretion behavior. In addition to the laser-scanned real ice shape, a 3D smooth artificial ice shape was constructed to mimic the outer profiles of the real ice accretion. This was done to simplify the geometry. In this work, we choose to simulate both real and artificial ice shapes. Specifically, the experiments

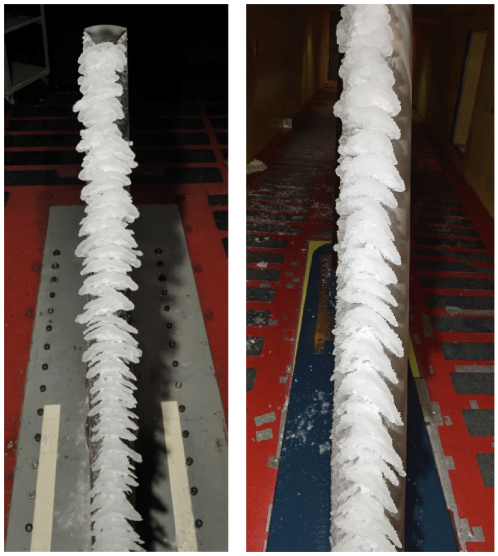

(a)

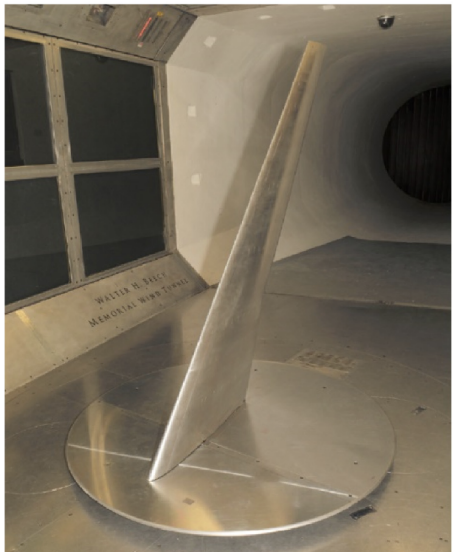

(b)

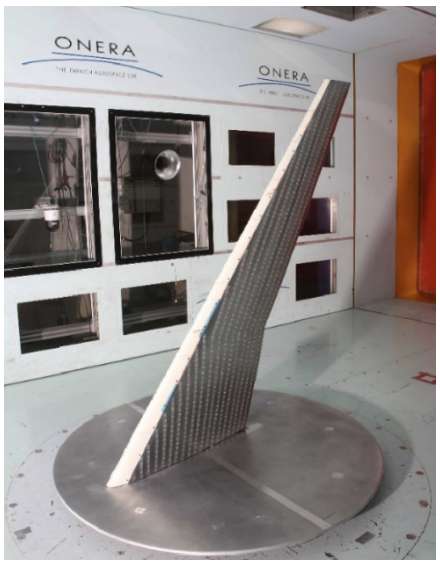

(c)

Figure 5.1: (a) Examples of 3D ice structures generated in the NASA IRT due to swept-wing geometries. (b) 8.9% subscale CRM65 swept wing model installed in the Wichita State University wind tunnel test section and (c) 13.3% subscale CRM65 swept wing model installed in the ONERA F1 pressurized wind tunnel test section [16].

Table 5.1: Details of the 8.9% and 13.3% scale CRM65 semi span wing geometry parameters at the Wichita State University (WSU) and ONERA F1 wind tunnels [18].

Wing Parameter	8.9% Scale (WSU Model)	13.3% Scale (ONERA Model)
Span, b	60.0 in. (1.524 m)	90.0 in. (2.286 m)
MAC	16.67 in. (0.423 m)	25.01 in. (0.635 m)
Area	865.3 in.^{2} (0.558 m^2)	1,051.0 in.^{2} (0.678 m^2)
Taper ratio	0.23	0.23
Root chord	27.0 in. (0.686 m)	40.50 in. (1.029 m)
Tip chord	6.19 in. (0.157 m)	9.28 in. (0.236 m)
Root α	4.4°	4.4°
Tip α	−3.8°	−3.8°
1/4-chord sweep angle	35°	35°
Leading edge sweep angle	37.2°	37.2°
Location of rotation center*	x = 19.37 in., y=0, z=0	x = 29.05 in., y=0, z=0
Location of $0.25 \times MAC$*	x = 17.49 in., y=0, z=0	x = 26.23 in., y=0, z=0

*Referenced to $(0, 0, 0)$ at the wing root leading edge at zero angle of attack.

corresponding to both the 8.9% scale model tested at the Wichita State University Beech wind tunnel and the 13.3% scale model tested at ONERA F1 pressurized wind tunnel [18] are selected (see Figure 5.1(b)). Geometric parameters for both wind tunnel models are detailed in Table 5.1. Example sections of the two ice shapes are shown in Figure 5.2. The flow field is characterized by a free-stream Mach number (M_∞) of 0.18 and a mean aerodynamic chord (MAC) based Reynolds number (Re_{MAC}) of 1.6 million (M), 2.7 M, and 9.6 M. A set of angles of attack (α) are simulated by altering the incoming velocity vector. The geometries are modeled in a hemispherical domain whose radius is 100 MAC lengths. Inflow conditions are specified using the free-stream pressure, density, and Mach number ($P_\infty = 101,325$ Pa, $\rho_\infty = 1.225$ kg/m^2, and $M_\infty = 0.18$). The outflow boundary is modeled with the non-reflecting characteristic boundary condition of [85]. The bottom wall of the domain, intersecting with the wing root, is prescribed as a free-slip boundary condition to best compare against wind tunnel-corrected experimental data. An algebraic equilibrium wall model is applied at the wing surface [22]. Statistics are gathered and averaged after reaching a statistically steady-state condition.

Water-tight geometries of the wing are used as the surfaces for generating a Voronoi diagram following the algorithm proposed by [35]. The complex roughness near the leading edge can be resolved by seeding Voronoi points, leading to a series of body-fitted unstructured meshes. The far-field resolution is chosen to be equal to the MAC. A number of refinement levels are then selected to determine the near-wall grid resolution. Each additional level adds ten cells in the wall-normal direction and isotropically refines the elements in the other two directions. This leads to grid cell counts of approximately 24 M control volumes (CV) for the coarse, 85 M CV for the medium and 320 M CV for the fine cases. This corresponds to 591, 1182, and 2365 points per MAC, respectively. Details of each ice shape and its grid resolution are indicated in Table 5.2 including the number

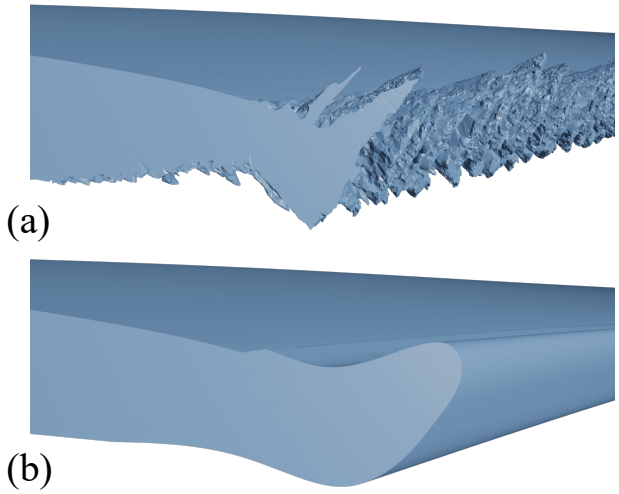

Figure 5.2: Representative sections of (a) real and (b) artificial ice shapes from the CRM65 swept wing geometry with ice.

of cells per reference scallop length, radius of curvature, R, and leading-edge laminar boundary layer, δ_{99}. An additional grid resolution was deemed necessary for the artificial-ice shape. This grid resolution, denoted 'xxfine', reduced the cell size in the smooth leading edge horn shape by a factor of 4 in each direction. This results in a grid with a total of 1.2 B CVs. This case's setup and simulation details are further described in Section 5.3.3. Examples of the structure of the coarse grid are shown in Figure 5.3 for the real-ice geometry. It can be seen that some of the smallest scales are highly under-resolved (i.e., less than one CV representing a roughness element). Still, the larger structures from the scallops have approximately 7 points across them (as referenced in Table 5.2. This is consistent with the grid resolution requirements determined by [8] when simulating glaze ice conditions for 2D laser-scanned airfoils.

In each case (see Table 5.2), comparisons are made to the integrated aerodynamic coefficients (C_L, C_D, and C_M) at a set of angles of attack. Pressure profiles are extracted along the streamwise and leading edge normal directions at several spanwise locations. In Figure 5.4, rows with pressure measurements are specified. C_P data is then compared for a series of spanwise locations for both geometries at three angles of attack: $\alpha = 8°$, $\alpha = 16°$, and $\alpha = 24°$. Locations of the spanwise measurements are detailed in Table 5.3.

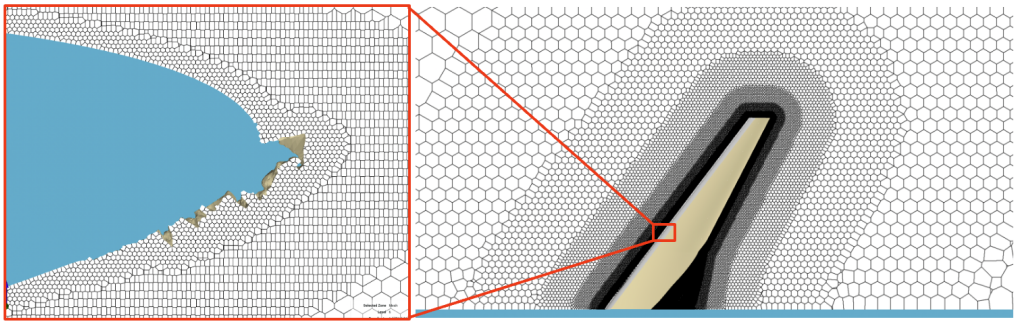

Figure 5.3: Example of the hexagonally packed elements of the coarse mesh with additional focus on the leading edge ice resolutions.

Table 5.2: Details of the simulated cases.

Ice shape	Grid name	Grid res. (M CVs)	Cells/MAC	Cells/ref. scallop length*	Cells/$R^{\dagger}$	Cells/$\delta_{99}^{\ddagger}$
Real	Coarse	24	591	7	–	–
Real	Medium	85	1182	14	–	–
Real	Fine	320	2365	28	–	–
Artificial	Coarse	24	591	–	4.5	0.2
Artificial	Medium	85	1182	–	9	0.4
Artificial	Fine	320	2365	–	18	0.8
Artificial	XXFine§	1200	3311	–	72	3.25

*Reference scallop height of 0.005 meters measured from the real ice condition [83].

† Reference radius of curvature, R, is calculated by extracting a streamwise slice of the artificial ice shape at row 10 (see Figure 5.4) and evaluating the curvature at the tip of the horn shape by fitting a third-order polynomial using a 10 point stencil about the evaluation point ($x = 40.57$ in., $y = 54.0$ in., $z = 0.08725$ in.).

‡ Reference laminar boundary layer height, δ_{99}, is calculated by extracting the boundary layer on the XXFine artificial ice grid near the leading edge of the horn ($x = 40.57$ in., $y = 54.0$ in., $z = 0.08725$ in.) at row 10 (see Figure 5.4) and determining the boundary layer thickness using the method of Griffin *et al.* [53].

§ Refinement is targeted at the leading edge only (see Figure 5.14) where each 'X' represents a halving of the near wall grid spacing.

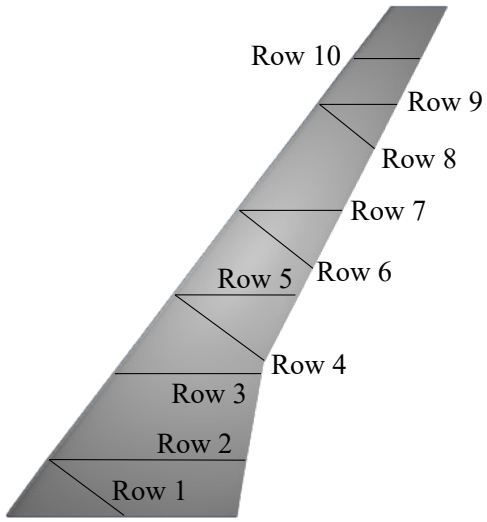

Figure 5.4: Representation of pressure profiles in the streamwise and leading edge normal direction.

Table 5.3: Details of the pressure profile spanwise locations.

Row Number	Orientation	Spanwise Location* (y/b)
1	Normal	0.11
2	Streamwise	0.11
3	Streamwise	0.28
4	Normal	0.44
5	Streamwise	0.44
6	Normal	0.60
7	Streamwise	0.60
8	Normal	0.81
9	Streamwise	0.81
10	Streamwise	0.90

*The spanwise location provided for the rows with normal orientation is from the leading edge.

Table 5.4: Fine grid (320 M CVs) errors for the integrated forces of the real ice geometry. Experimentally, the relative (and absolute) uncertainty for C_L, C_D, and C_M was found to be 0.272% (0.137 lift counts), 3.15% (6.8 drag counts), and 9.01% ($\Delta C_M = 0.0006$) respectively given a reference condition of $\alpha = 4^\circ$ and $Re_{MAC} = 2.4 \times 10^6$ [118].

α	Lift counts ($\lvert\Delta C_L\rvert = 0.01$)	$\epsilon_L(\%)$	ΔC_M	$\epsilon_M(\%)$	Drag counts ($\lvert\Delta C_D\rvert = 0.0001$)	$\epsilon_D(\%)$
2°	0.2	0.83	0.0047	4.86	15.2	-5.68
5°	1.4	-2.89	0.0161	9.98	24.9	-5.85
8°	1.0	-1.6	0.0159	8.39	7.7	1.00
16°	0.9	1.16	-0.01778	-10.56	29.3	1.10
24°	2.6	3.24	-0.00078	-0.30	126.2	-3.09

5.3 Results

5.3.1 Real Ice Shape

The real ice geometry was simulated across a set of α values ranging from 2° to 24°. In Figure 5.5, (a) lift (C_L), (b) moment (C_M), and (c) drag (C_D) coefficients are compared for the three grid resolutions to the experimental measurements. Good agreement is found for all coefficients compared to the force balance data of [18]. For the three grids, only minor changes are shown in these coefficients. In all the simulations, the results are within three lift counts (defined as $\Delta C_L = 0.03$) of the experimental results. This value was suggested as an accuracy requirement for high-lift aircraft configurations in [29]. A summary of the percent error and absolute errors in each coefficient for the fine grid is included in Table 5.4. We see the largest errors in C_M, with a maximum error of 10.56%. The maximum percent error for drag occurs at 2° and is 5.68%. The absolute largest difference in drag is shown to be well past the wing's stall angle at 24°. However, it should be noted that the experimental data has non-negligible uncertainties. For example, at a given reference condition of $\alpha = 4^\circ$ and $Re_{MAC} = 2.4 \times 10^6$ the relative uncertainty for C_L, C_D, and C_M was found to be 0.272%, 3.15%, and 9.01% respectively [118].

To better understand the flow features, comparisons are made to oil flow visualizations. In Figure 5.6, oil flow visualizations (a) are compared to both averaged (b) and instantaneous (c) wall shear stress values from the finest simulation at $\alpha = 8^\circ$. We find similar flow patterns to those of the experimental work, namely, the inboard regions of high and low shear stress due to the specific scallop ice shape geometries indicative of the local streamwise vortices. Similarly, we observe a region of high shear stress running diagonally across the wing, starting near the leading edge opposite of the Yehudi break. Generally, the patterns between the two geometries are consistent.

We select three angles ($\alpha = 8^\circ$, $\alpha = 16^\circ$, and $\alpha = 24^\circ$) and look at the streamwise pressure distributions (Figures 5.7, 5.8, and 5.9). Similar to the integrated quantities, we find minimal differences between the three grid levels. For each figure, the increasing Row number corresponds

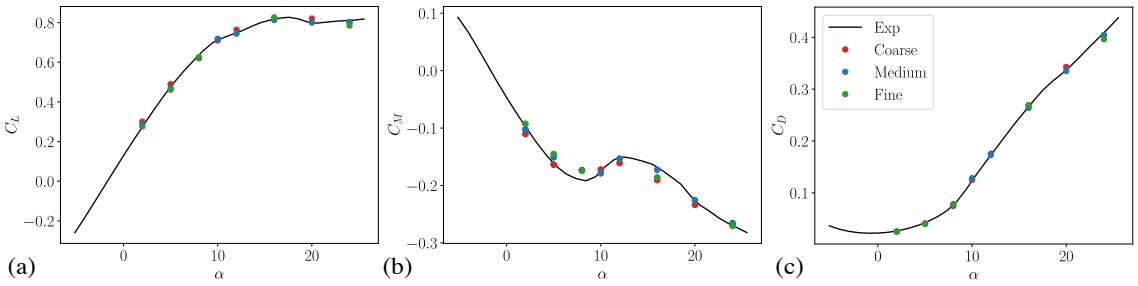

Figure 5.5: Comparison of the integrated quantities, such as (a) Lift (C_L), (b) moment (C_M), and (c) drag (C_D), to the experimental data of [16] for the real ice geometry at the coarse (24 M CVs), medium (85 M CVs), and fine (320 M CVs) grid resolutions.

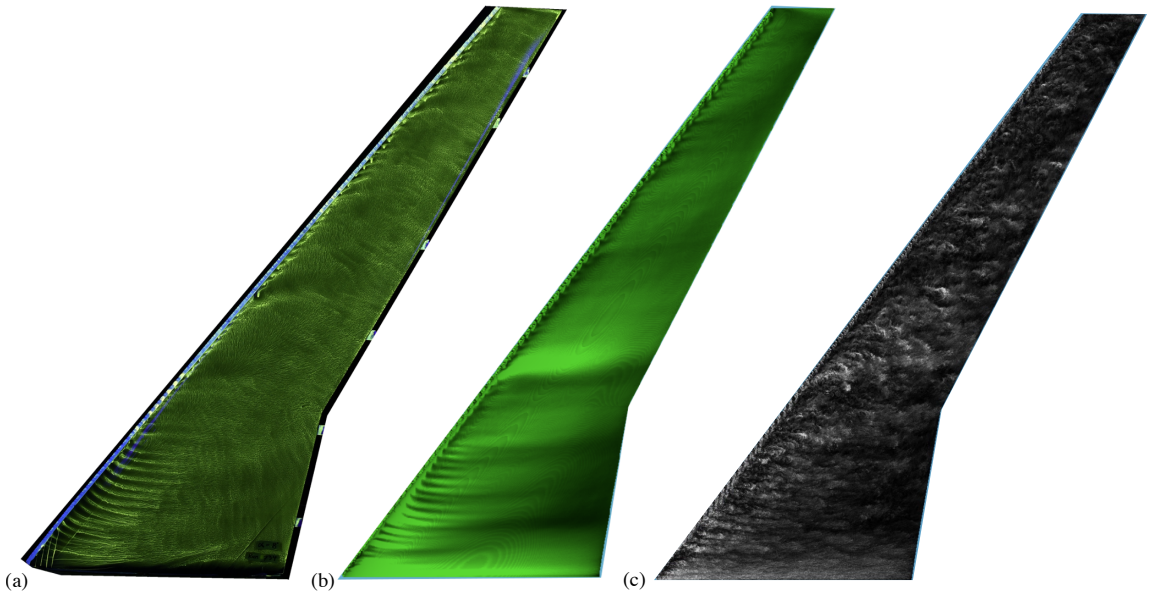

Figure 5.6: (a) Oil flow visualizations compared to simulation results of both (b) averaged and (c) instantaneous wall shear-stress values on the surface of the real ice geometry on the finest grid at $\alpha = 8°$.

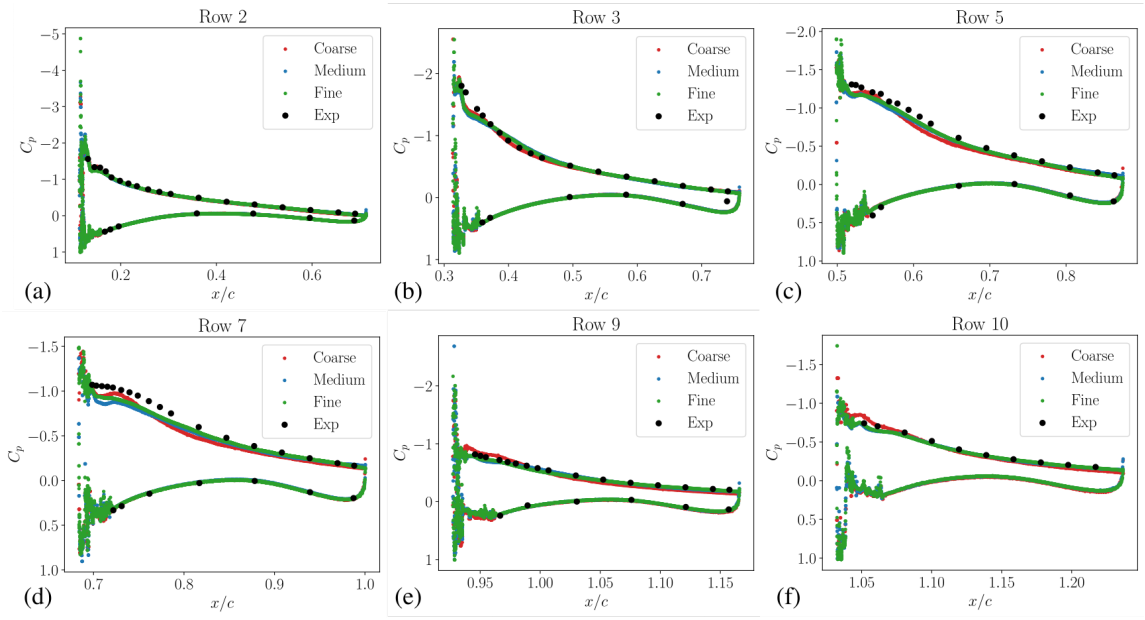

Figure 5.7: Streamwise pressure profiles for the spanwise locations of (a) row 2, (b) 3, (c) 5, (d) 7, (e) 9, and (f) 10 at $\alpha = 8°$ compared to [16] with the coarse (24 M CVs), medium (85 M CVs), and fine (320 M CVs) resolutions.

to moving from the wing's inboard to the outboard section as illustrated in Figure 5.4. In each C_P plot of Figure 5.7, a high leading edge suction event is followed by a region of adverse pressure gradient. In all cases (a)-(f), good agreement is observed compared to the experimental data. There is a slight under-prediction on the suction side for Figure 5.7(d), which is at the transition between the mid-board and outboard sections of the wing.

We show good agreement with the experimental data in Figure 5.8 and 5.9. These higher angles have massive flow separation caused by the large leading edge ice accretion. These chosen cases bound the stall region of this wing. It is interesting to note that for the clean geometry described in [18], the critical stall angle is approximately 12°. Here, we note a delayed critical stall angle, but the rapid shift in the direction of the moment renders the lift unusable [18]. Because of this, the value at $\alpha = 16°$ is considered outside of the usable range of this wing while it is still prior to the critical angle of attack.

5.3.2 Artificial Ice Shape

We simulate the artificial ice geometry with three angle's of attack (α): 8°, 16°, and 24°. These correspond to the α values used to evaluate the pressure coefficients of the real ice geometry (see Section 5.3.1). In Figure 5.10, (a) lift (C_L), (b) moment (C_M), and drag (C_D) coefficients are compared for the three baseline grid resolutions equivalent to the real ice cases. These coefficients

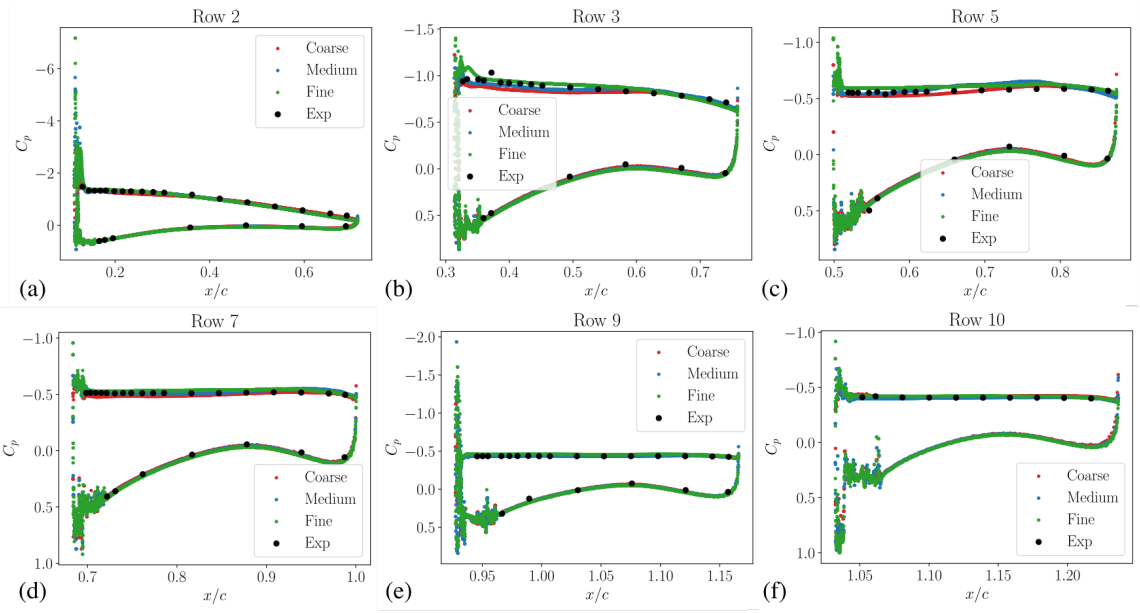

Figure 5.8: Streamwise pressure profiles for the spanwise locations of (a) row 2, (b) 3, (c) 5, (d) 7, (e) 9, and (f) 10 at $\alpha = 16°$ compared to [16] with the coarse (24 M CVs), medium (85 M CVs), and fine (320 M CVs) grid resolutions.

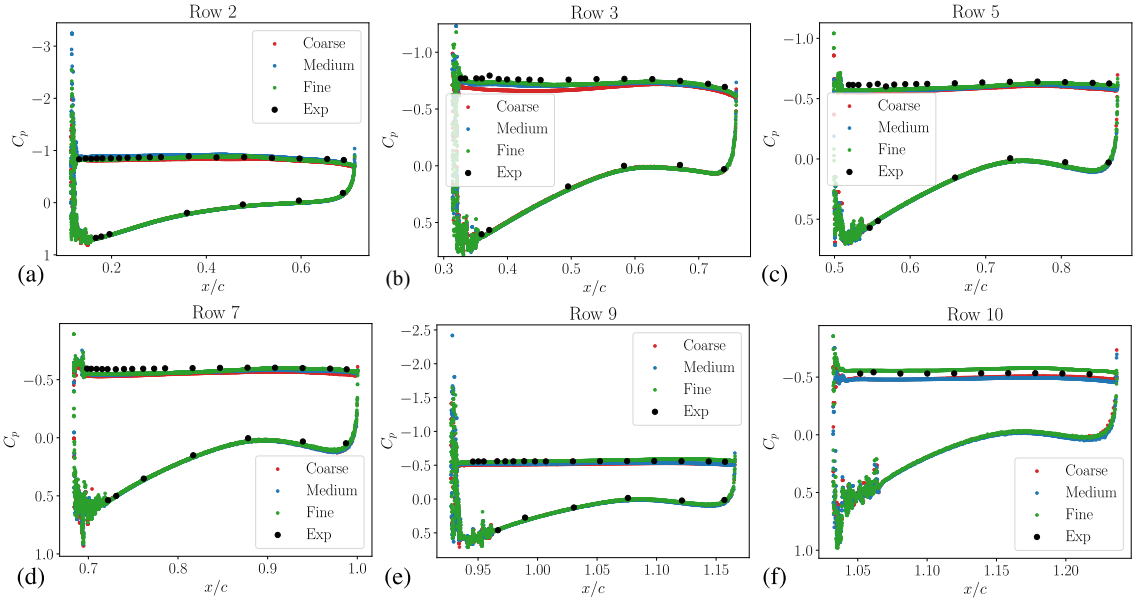

Figure 5.9: Streamwise pressure profiles for the spanwise locations of (a) row 2, (b) 3, (c) 5, (d) 7, (e) 9, and (f) 10 at $\alpha = 24°$ compared to [16] with the coarse (24 M CVs), medium (85 M CVs), and fine (320 M CVs) grid resolutions.

Table 5.5: Fine grid (320 M CVs) errors for the integrated forces of the artificial ice geometry. Experimentally, the relative (and absolute) uncertainty for C_L, C_D, and C_M was found to be 0.272% (0.137 lift counts), 3.15% (6.8 drag counts), and 9.01% ($\Delta C_M = 0.0006$) respectively given a reference condition of $\alpha = 4^\circ$ and $Re_{MAC} = 2.4 \times 10^6$ [118].

α	Lift counts ($\lvert\Delta C_L\rvert = 0.01$)	$\epsilon_L(\%)$	ΔC_M	$\epsilon_M(\%)$	Drag counts ($\lvert\Delta C_D\rvert = 0.0001$)	$\epsilon_D(\%)$
8°	1.0	1.6	-0.01908	9.71	274	33.51
16°	2.4	2.64	-0.02329	14.03	148	5.53
24°	8.5	9.1	-0.01062	4.26	475	10.62

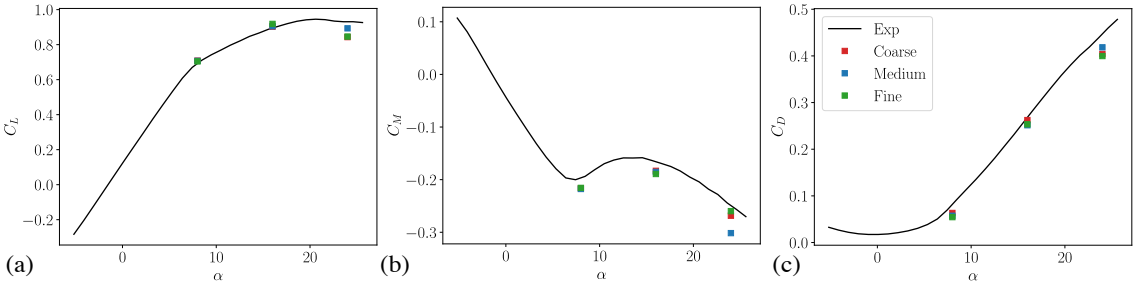

Figure 5.10: Comparison of the integrated quantities, such as (a) Lift (C_L), (b) moment (C_M), and (c) drag (C_D), to the experimental data of [16] for the artificial ice geometry at the coarse (24 M CVs), medium (85 M CVs), and fine (320 M CVs) grid resolutions.

are then compared to the experimental force balance data of [18]. Notably, while we have reasonable agreement with the lift coefficient, there is an under-prediction with respect to both the moment and drag coefficients. Table 5.5 delineates both the percent and absolute errors associated with the fine grid resolution for each of the three α values. We observe much higher errors than the results with the real ice geometry. This is most pronounced in C_D, whose error is 274, 148, and 475 drag counts for α at 8°, 16°, and 24°, respectfully. Additionally, we show little sensitivity to grid resolution while exhibiting large errors in drag and moments. To better understand the deterioration of the predictive accuracy of the artificial ice shape compared to the real ice shape, we examine the pressure coefficients along the spanwise direction.

In Figure 5.11, pressure coefficients are plotted at various spanwise locations from the inboard to outboard sections of the artificial iced wing at $\alpha = 8^\circ$. We notice good agreement at the furthest inboard station (Figure 5.11(a), but increasingly poor performance with the further outboard stations. This is contrary to the results shown in the integrated quantities of Figure 5.10 where good agreement is achieved in C_L. While the overall lift is accurately captured, the distribution of lift is inaccurate. Therefore, we only achieved reasonable results for the lift due to errors in the pressure profiles being canceled. In particular, the leading edge region of the outboard stations all drastically overpredict the leading edge suction. These then undergo a rapid adverse pressure gradient not

present in the experimental data.

In Figure 5.12, we compare oil flow images from [18] with the wall shear stress data obtained through simulations conducted with real and artificial ice shapes on the fine grid resolution. A notable difference is observed in the flow structures for the two shapes. The real ice shape displays strong channeling effects due to the local leading-edge ice topology. There is a breakdown to a turbulent flow immediately following the roughness. We find similar flow patterns to the experimental work in the simulation results for the real ice shape, namely, the inboard regions of high and low shear stress due to the specific scallop ice shape geometries. Similarly, we observe a region of high shear stress running diagonally across the wing, starting near the leading edge opposite the Yehudi break. For the artificial ice shape, the present simulations do not fully replicate the flow patternation measured in the experiment. Notably, the experimental results do not exhibit the progression of high and low wall shear stress regions along the span, as seen in the simulation. Additionally, it is unclear how transition behaves when looking only at the oil flow results. A reattachment line downstream on the artificial horn shape indicates flow separation of the horn. This separation pattern is not found in the simulation results. Referencing the experimental pressure profiles of Figure 5.11, one can observe leading edge separation events. These occur at the leading edge horn prior to the flow transitioning. When comparing the real and artificial ice shapes, it is apparent that they exhibit very different flow fields, emphasizing the challenge of employing artificial ice shapes as surrogates for real-world geometries. Additionally, the current modeling approach does not consider laminar boundary layers or laminar separation, leading to poor results when using WMLES approaches for the artificial ice shape.

5.3.3 Additional resolution and boundary condition discussion for the artificial ice shape

While satisfactory results are achieved across all resolutions for the real ice case, convergence to the experimental results for the artificial ice shape remains difficult even at the fine grid resolution (approximately 320 M CVs). Our hypothesis attributes this inaccuracy to an incorrect assumption of the existence of a turbulent boundary layer at the leading edge of the smooth horn shape. We locally apply a no-slip boundary condition to the leading edge horn ice shape to further explore this issue. This boundary condition extends up to the point of flow reattachment, as shown in the experimental oil flow data of [18]. The pink line in Figure 5.13 indicates the approximate reattachment location. Additionally, we reduce the cell size at the wall by a factor of 4 in each direction to provide better resolution for the flow structures around the rounded horn (see Figure 5.14). This results in a grid with a total of 1.2 B CVs. We apply this procedure in attempting to resolve laminar flow at the horn shape, including developing laminar boundary layers, transition, and laminar separation bubbles.

In Figure 5.15, pressure coefficients are compared between experimental results [18] and simulations using the previous fine grid resolution (320 M CVs) and the updated xxfine resolution (1.2

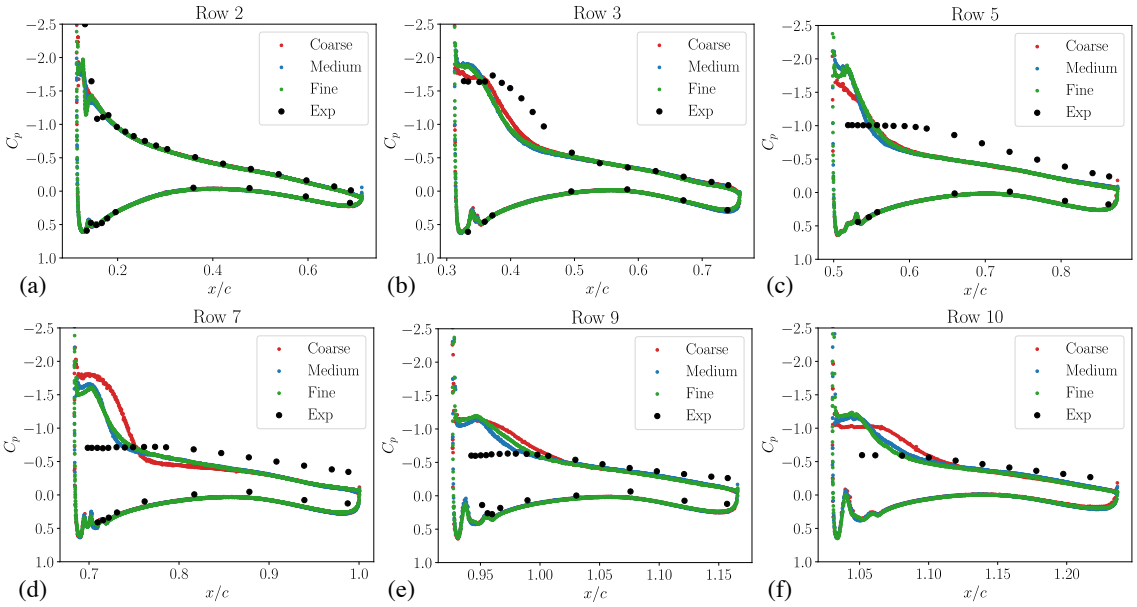

Figure 5.11: Streamwise pressure profiles of the artificial ice shape for the spanwise locations of (a) row 2, (b) 3, (c) 5, (d) 7, (e) 9, and (f) 10 at $\alpha = 8°$ compared to [18] with the coarse (24 M CVs), medium (85 M CVs), and fine (320 M CVs) grid resolutions.

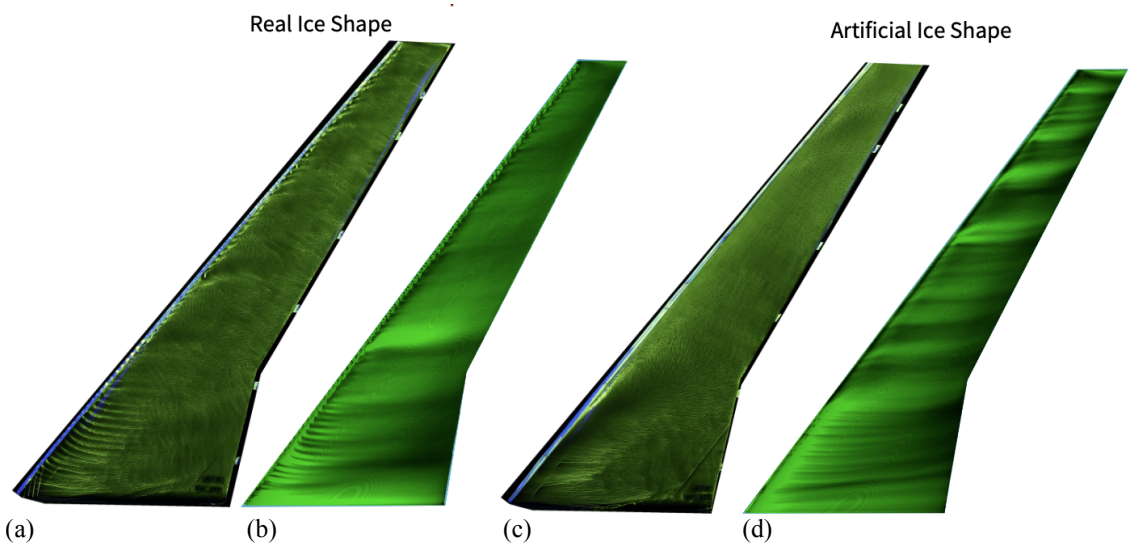

Figure 5.12: Experimental oil flow visualizations (a,c) compared to the average simulated wall shear-stress values (b,d) on the surface of the real ice geometry (a,b) and artificial ice geometry (c,d) on the fine grid at $\alpha = 8°$.

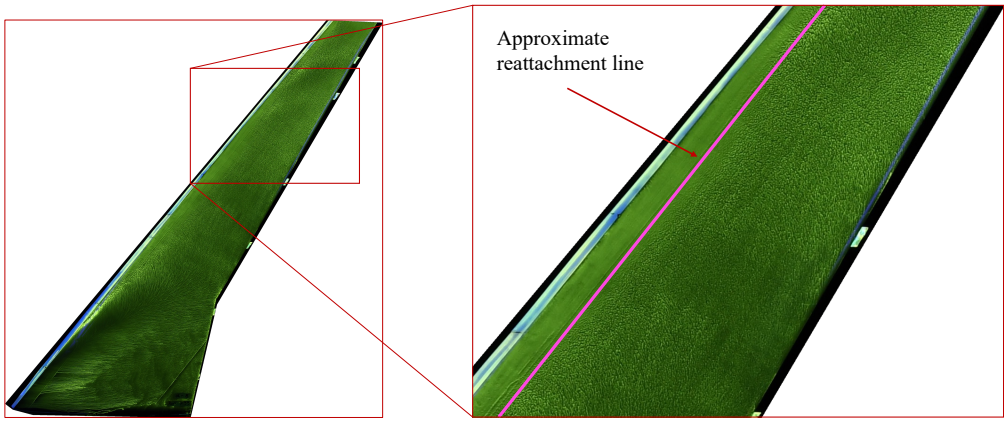

Figure 5.13: Oil flow visualization illustrating the location where we split the applied boundary conditions dependent on the attachment line of the flow at $\alpha = 8°$.

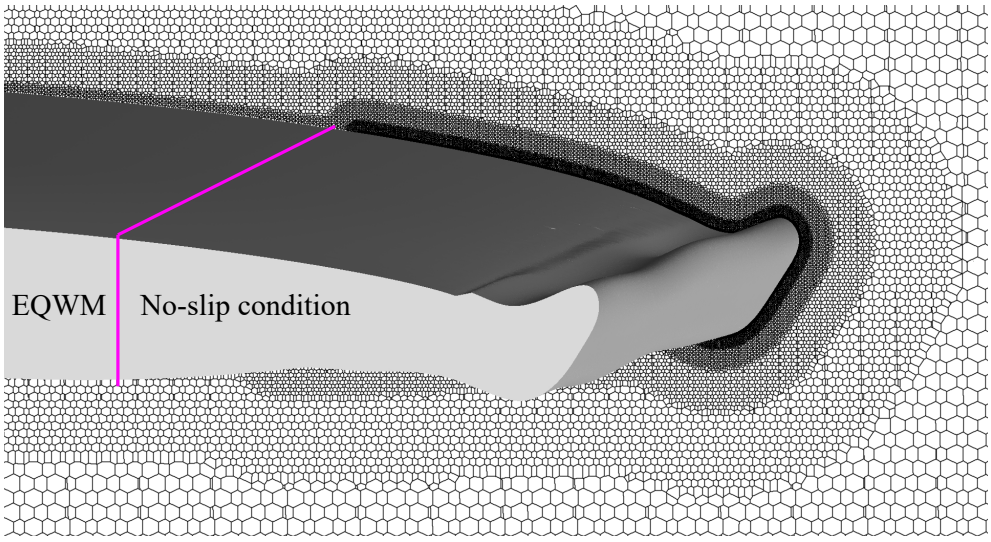

Figure 5.14: Boundary condition assignment and grid resolution image for the xxfine artificial ice shape.

B CVs) with a no-slip condition applied to the leading edge as opposed to the EQWM applied at the rest of the wing surface. Significant improvements are observed at each spanwise station compared to the fine grid resolution. In particular, the outboard sections near the wing's leading edge no longer overpredict suction. This results in a much shallower adverse pressure gradient near the quarter-chord location for each spanwise pressure profile.

To better understand the physical implications of using a highly resolved no-slip leading edge, we examine surface contours of wall shear stress and a slice of streamwise velocity at the Row 10 spanwise station in Figure 5.16. Comparisons are made with the (a) fine grid artificial ice case (320 M CVs), (b) xxfine (1.2 B CVs) leading-edge artificial ice case with the no-slip leading edge boundary condition, and (c) fine real ice case (320 M CVs). In Figure 5.16(b), a thin laminar boundary layer is at the leading edge of the smoothed horn. A wall normal boundary layer probe located at the leading edge of the Row 10 spanwise station ($x = 40.56$ in., $y = 54.0$ in., $z = 0.08725$ in.) was used to determine that the 1.2 B CV grid resolution has only 3.25 CVs per δ_{99}. (see Table 5.2). At this location, the flow has had little time to develop, so the boundary layer thickness is small relative to the scale of the horn shape, which has 72 CVs per radius of curvature, R, evaluated at the same location as the boundary layer probe (see Table 5.2 for how R is calculated). Even at the coarsest resolution, there are 4.5 points per R. Further downstream, as the flow passes over the upper region of the horn, it detaches, resulting in local flow separation and transition to turbulence.

In contrast, the fine grid geometry of Figure 5.16(a) with the EQWM applied everywhere results in a reduced separation bubble downstream of the leading edge horn, with reattachment occurring further upstream compared to the xxfine case with a no-slip leading edge boundary condition in Figure 5.16(b). Additionally, the downstream turbulent boundary layer is smaller than found in the xxfine case. This fine grid approach [Figure 5.16(a)] results in increased drag error as well as incorrect pressure distributions throughout the span of the wing. At this resolution, there is less than one cell per δ_{99} at the Row 10 spanwise leading edge location, which is insufficient to resolve the leading-edge flow field. Lastly, the real ice case shown in (c) encounters immediate transition and separation events due to the leading-edge roughness. These geometrically induced transition and separation phenomena remain robust even at coarse resolutions, highlighting the dominant effect of the rough surface on the flow field. For this case, the primary length scale of interest is the reference scallop length, which is resolved with 7 cells at the coarsest resolution, leading to an accurate representation of the integrated forces.

These results emphasize the challenges of modeling complex ice shapes with artificially smoothed geometries, which require additional degrees of freedom and careful consideration of where to apply the EQWM versus a no-slip condition. Table 5.6 compares the integrated forces between the fine (320 M CVs) and xxfine (1.2 B CVs) grid resolutions of the artificial ice shape. The integrated forces confirm additional improvements in the quantities of interest, drastically reducing the error of both moments and drag. While we obtain improved results, we note that it is at the cost of

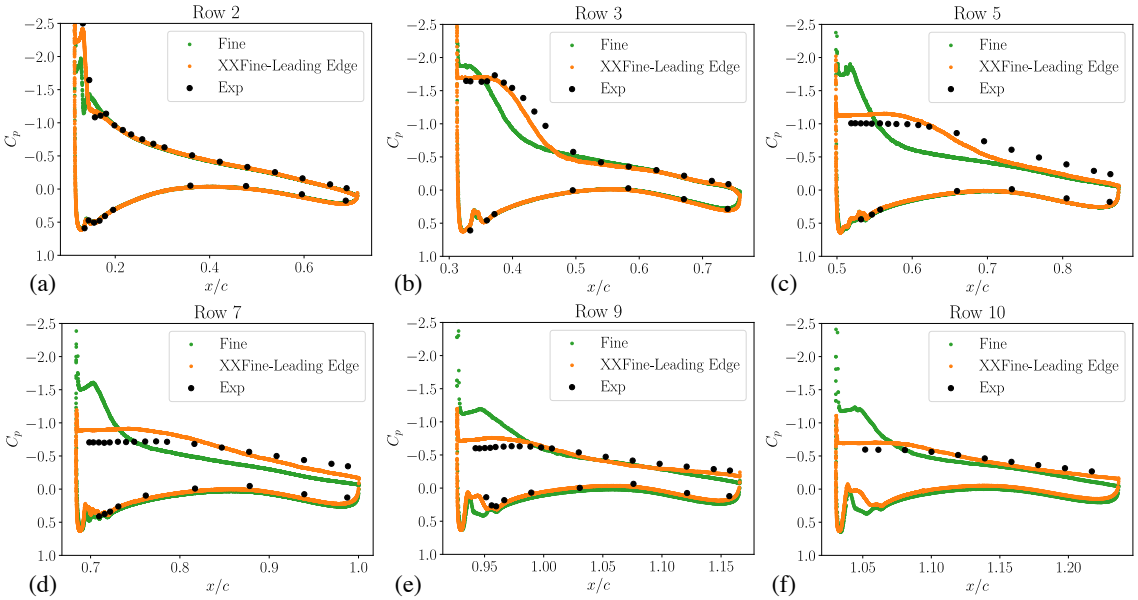

Figure 5.15: Streamwise pressure profiles of the artificial ice shape for the spanwise locations of (a) row 2, (b) 3, (c) 5, (d) 7, (e) 9, and (f) 10 at $\alpha = 8°$ compared to [18] with a fine and xxfine (using targeted refinement on the leading edge) grids.

Table 5.6: Error reduction for integrated forces with fine grid using the EQWM at the leading edge and fine grid (320 M CVs) using the no-slip condition at the leading edge.

Res.	Lift counts ($\lvert\Delta C_L\rvert = 0.01$)	$\epsilon_L(\%)$	ΔC_M	$\epsilon_M(\%)$	Drag counts ($\lvert\Delta C_D\rvert = 0.0001$)	$\epsilon_D(\%)$
Fine	1.0	1.69	-0.01908	9.71	274	33.51
XXFine	0.96	1.39	0.00229	-1.17	49	5.99

significant computational overhead and the need to use experiments to select where to place boundary conditions. It is known that laminar conditions can significantly increase the computational cost for aerospace applications due to laminar boundary layers [98]. Current models aim to reduce this cost by addressing both laminar boundary layers and the transition to turbulence using a Falkner-Scan wall model coupled with a parabolized stability equation solver [51]. While these efforts are promising for general applications, they do not address the issue of laminar separation, which occurs at the leading edge of these artificial horns.

5.3.4 Reynolds number effects on simulating both real and artificial ice shapes

In Section 5.3.3, it was shown that special considerations were necessary to accurately simulate the artificial ice shape at wind tunnel Reynolds numbers (around $\mathcal{O}(10^6)$). However, it remains

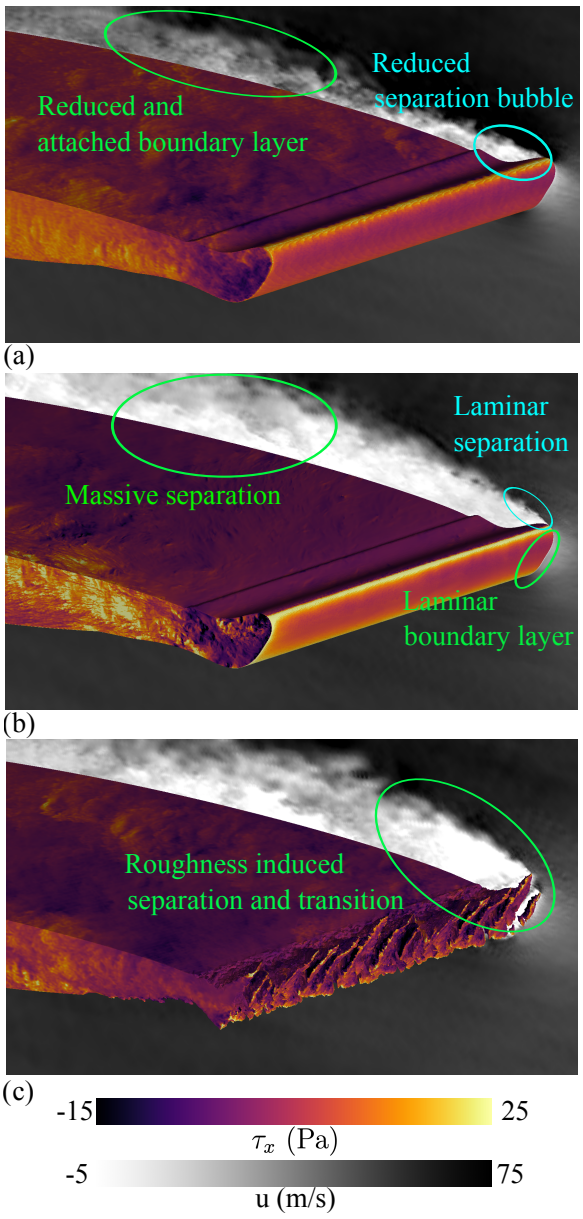

Figure 5.16: Comparison of instantaneous flow structures using contours of wall shear stress and a slice at Row 10 (see Figure 5.4) colored by streamwise velocity for (a) the fine artificial ice case (using EQWM at the leading-edge), (b) the xxfine artificial ice case (using the no-slip condition at the leading edge), and (c) the fine real ice case (using the EQWM at the leading edge).

unclear whether similar challenges would occur at flight Reynolds numbers (around $\mathcal{O}(10^7)$), where transition may occur further upstream [107], potentially relaxing the need for additional resolution at the leading-edge horn.

To study the Reynolds number effects on real and artificial ice shapes, [17] conducted additional experiments at the ONERA F1 pressurized wind tunnel in southern France. These experiments used a 13.3% scaled version of the CRM65 wing (in contrast to the 8.9% scaled version used at WSU) to represent the ice shapes (see Table 5.1). In this study, we extend our investigations by incorporating two additional Reynolds numbers at $M = 0.18$: $Re_{MAC} = 2.7 \times 10^6$ and $Re_{MAC} = 9.6 \times 10^6$. The former validates our setup in the new tunnel, while the latter explores Reynolds numbers approaching flight-like conditions. For the real ice shape, we conducted simulations at all three grid resolutions to further confirm the robustness of coarsened resolutions in the presence of real ice shapes (see Table 5.2). For the artificial ice shape, we focus solely on the fine grid resolution (see Table 5.2) to assess if the issues identified in Section 5.3.3 persist.

In Figures 5.17 and 5.18, we compare the coarse (24 M CVs), medium (85 M CVs), and fine (320 M CVs) grid resolutions for the real ice geometry to the experimental data of [17]. Similar to the results shown in Figure 5.7, all grid resolutions demonstrate agreement with the experimental data [17]. This is further emphasized in Table 5.7, where the error in lift counts for the fine grid real ice shape are both less than two. Additionally, we find excellent agreement in drag, where the error in drag counts are 2.1 and 1.09 for each Reynolds number, respectively. This confirms the robustness of using real ice shapes with WMLES, even at higher Reynolds numbers.

Conversely, Figures 5.19 and 5.20 show similar discrepancies to those detailed in Figure 5.11, between WMLES predictions of the artificial ice shape and experimental data [17]. Although slight improvements are noted with increasing Reynolds numbers, particularly evident in Figures 5.19(e) and 5.20(e), substantial disparities persist compared to the accuracy achieved with real ice geometries. For instance, while the error in drag reduces from 544 to 175 drag counts as Reynolds number increases from 1.8×10^6 to 9.6×10^6, the overall predictive capability for artificial ice shapes remains inadequate (see Tables 5.5 and 5.7). While WMLES's predictive capability improves when using artificial ice shapes at higher Reynolds numbers, these simulations do not yet achieve the same accuracy when using real ice geometries.

To better understand the behavior of the boundary layer at the leading edge of the horn, we approximate the horn's shape to that of a cylinder. It is well established that cylinders start to transition in their boundary layer, rather than in the wake region, at a Reynolds number, Re_d of approximately 2×10^5 [72]. In Figure 5.21, we propose two possible analogous cylinder radii, r_h, for the artificial horn at Row 10. The first, $r_{h,1}$, fits within the horn's leading edge curvature near the separation point and is considered the most relevant length scale for this analysis. The second radius, $r_{h,2}$, fits the curvature of the pressure side of the ice shape and serves as an upper bound for our estimates. Using these local length scales, we evaluate whether the simulated Reynolds numbers fall

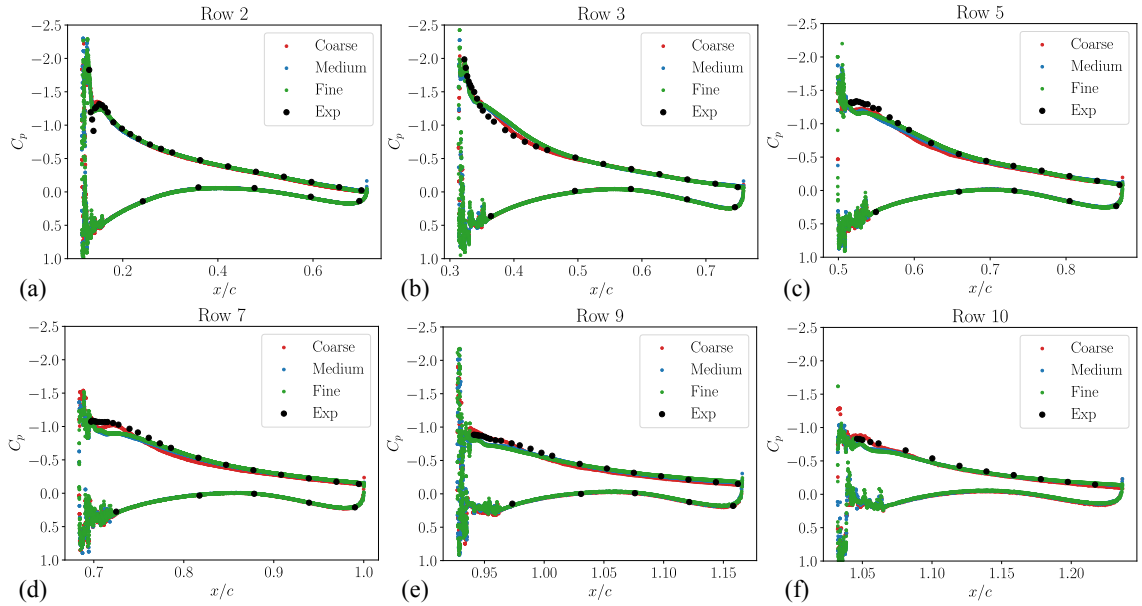

Figure 5.17: Streamwise pressure profiles of the real ice shape for the spanwise locations of row (a) 2, (b) 3, (c) 5, (d) 7, (e) 9, and (f) 10 at $\alpha = 8°$ and $Re_{MAC} = 2.7 \times 10^6$ compared to [17] at the coarse (24 M CVs), medium (85 M CVs), and fine (320 M CVs) resolutions.

within the sub-critical ($Re_d < 2\times10^5$) or critical regime ($2\times10^5 < Re_d < 5\times10^5$). As shown in Table 5.8, for all cases except $Re_{h,2}$ at $Re_{MAC} = 9.6\times10^6$, the local Reynolds number ($Re_{h,l} = 2U_\infty r_{h,l}/\nu$ where l is 0 or 1) remains in the sub-critical regime. Therefore, we expect the leading edge to be laminar in this sub-critical condition prior to the flow separation. The Re_{MAC} required to force $Re_{h,1}$ into the critical range is approximately 21 million. At such high Reynolds numbers, achieving a fully critical leading edge effect necessitates finer grid resolution due to Reynolds number scaling effects in separating flows [1]. However, since the real ice geometry shows minimal change with increasing Reynolds number, the resolution requirements for that geometry are expected to be less dependent on the Reynolds number.

5.4 Summary

A complex three-dimensional swept wing with scallop-like ice accretions was simulated using WM-LES methods. Two ice shapes were simulated: a real-ice shape directly using the laser-scanned shape and an artificial-ice shape constructed using the maximum combined cross-section of the 3D ice accretion. We find good agreement in the quantities of interest, such as lift, drag, moments, and pressure profiles for the real-ice shape at all grid resolutions (24 million control volumes (CV), 85 million CV, and 320 million CV). The comparison to oil flow visualizations further validated the

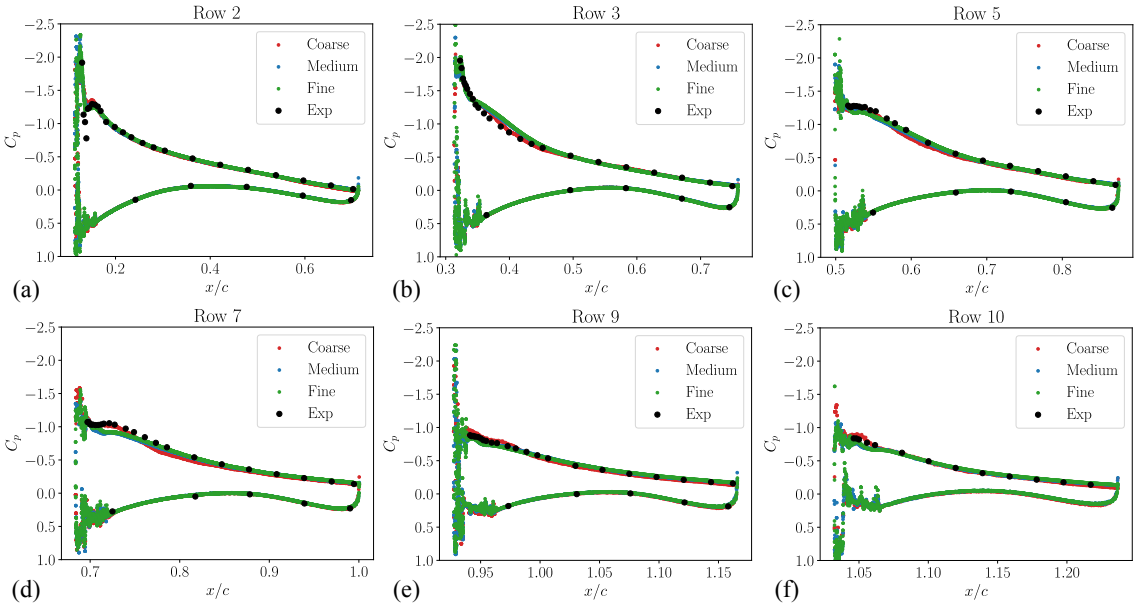

Figure 5.18: Streamwise pressure profiles of the real ice shape for the spanwise locations of row (a) 2, (b) 3, (c) 5, (d) 7, (e) 9, and (f) 10 at $\alpha = 8°$ and $Re_{MAC} = 9.6 \times 10^6$ compared to [17] with the coarse (24 M CVs), medium (85 M CVs), and fine (320 M CVs) grid resolutions.

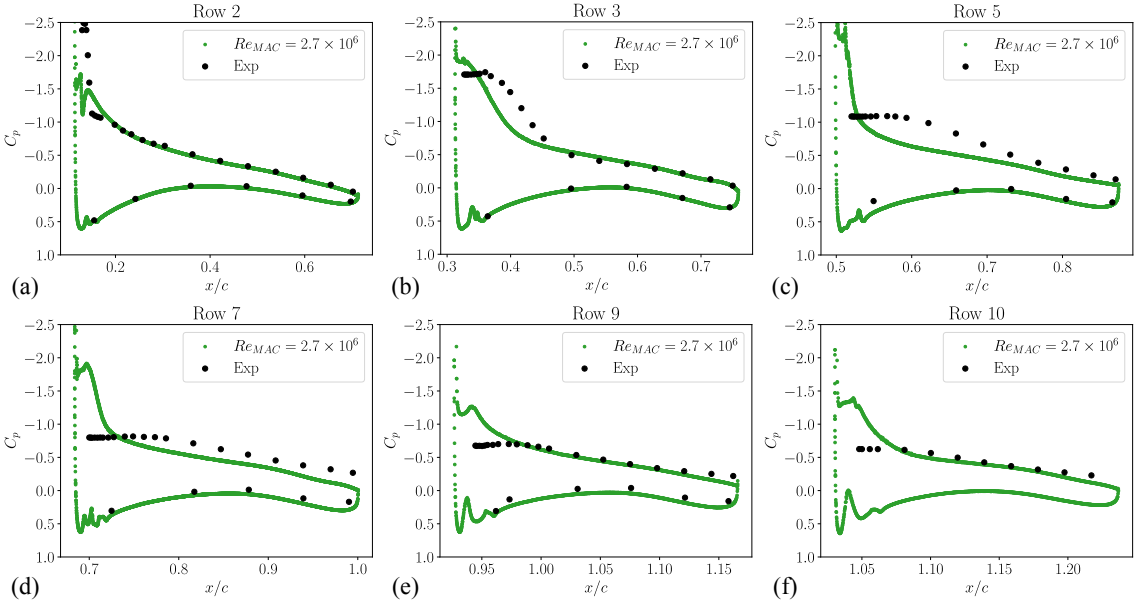

Figure 5.19: Streamwise pressure profiles of the artificial ice shape for the spanwise locations of row (a) 2, (b) 3, (c) 5, (d) 7, (e) 9, and (f) 10 at $\alpha = 8°$ and $Re_{MAC} = 2.7 \times 10^6$ compared to [17] at the fine grid resolution (320 M CVs).

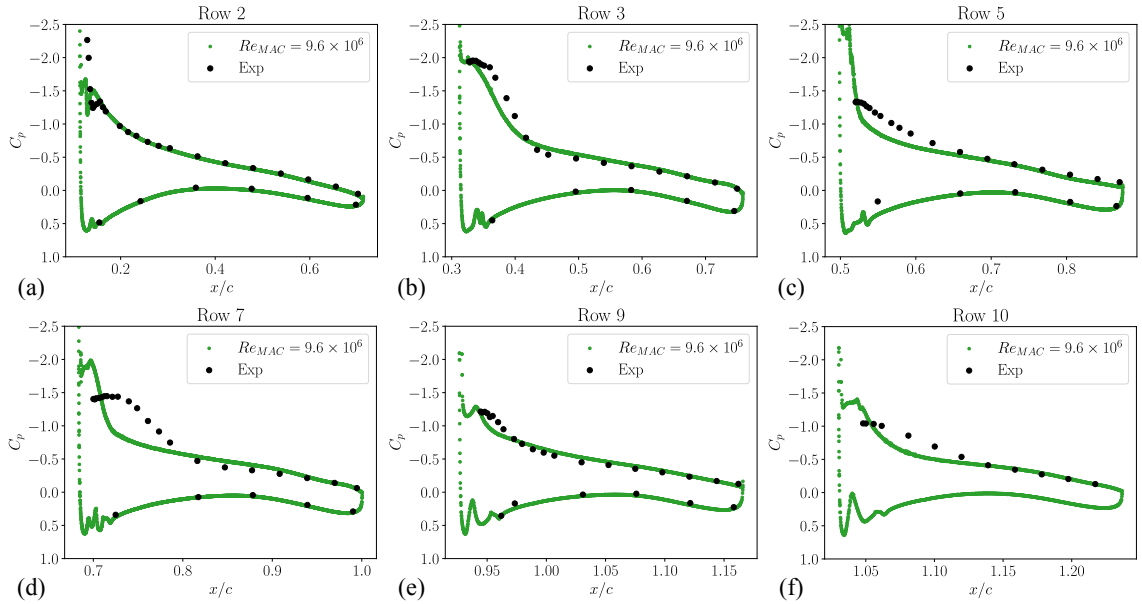

Figure 5.20: Streamwise pressure profiles of the artificial ice shape for the spanwise locations of row (a) 2, (b) 3, (c) 5, (d) 7, (e) 9, and (f) 10 at $\alpha = 8°$ and $Re_{MAC} = 9.6 \times 10^6$ compared to [17] at the fine grid resolution (320 M CVs).

Table 5.7: Fine grid (320 M CVs) errors for the integrated forces of the real and artificial ice geometries with increasing Reynolds number. Experimentally, the relative (and absolute) uncertainty for C_L, C_D, and C_M was found to be 0.272% (0.137 lift counts), 3.15% (6.8 drag counts), and 9.01% ($\Delta C_M = 0.0006$) respectively given a reference condition of $\alpha = 4°$ and $Re_{MAC} = 2.4 \times 10^6$ [118].

Ice shape	Re_{MAC}	Lift counts ($\lvert\Delta C_L\rvert = 0.01$)	$\epsilon_L(\%)$	ΔC_M	$\epsilon_M(\%)$	Drag counts ($\lvert\Delta C_D\rvert = 0.0001$)	$\epsilon_D(\%)$
Real	2.7×10^6	1.9	2.95	0.01552	-8.01	2.1	0.27
Real	9.6×10^6	1.34	2.04	0.00865	-4.46	1.09	0.14
Artificial	2.7×10^6	0.93	1.30	-0.03219	-16.10	301	37.40
Artificial	9.6×10^6	0.26	0.36	-0.00972	-4.19	175	26.20

Table 5.8: Estimation of local Reynolds number of the artificial horn ice shape at Row 10 for each Re_{MAC}. Note, cases are considered in the critical regime when $Re_{h,l} > 2 \times 10^5$.

Re_{MAC}	$Re_{h,1}$	$Re_{h,2}$
1.8×10^6	0.17×10^5	0.45×10^5
2.7×10^6	0.26×10^5	0.68×10^5
9.6×10^6	0.92×10^5	2.4×10^5

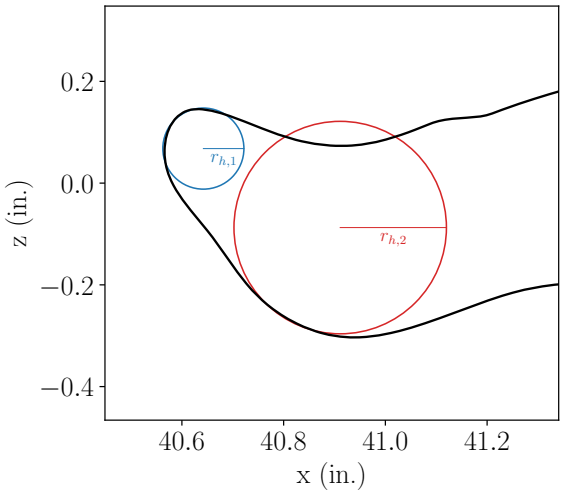

Figure 5.21: Outer mold line slice at Row 10 for the artificial ice shape zoomed-in at the leading edge identifying two potential analogous cylinders ($r_{h,1}$ and $r_{h,2}$) to represent the scale of the local flow phenomena.

ability of WMLES results to capture observed flow features faithfully.

For the artificial ice shape, it was found that the same grid resolutions used for the real ice shape were unable to simulate this geometry accurately. While reasonable lift coefficients were obtained, pressure profiles showed this was due to a cancellation of errors. The smooth leading edge in the artificial-ice shape introduces additional physics not present in the real-ice geometry, including laminar boundary layers, laminar separation, and turbulent transition. These additional physics stress the assumptions of the equilibrium wall model and, therefore, require a different approach. Additional refinement was added to the leading edge of the artificial wing, and this region was run with a no-slip condition, a more consistent boundary layer for laminar flows. Using this strategy improved the accuracy of the simulations at the cost of additional computational resources (1.2 B control volumes).

To better understand the performance of the models at more flight-like conditions, a series of simulations were conducted at two additional Reynolds numbers: 2.7×10^6 and 9.6×10^6. For the real ice geometry, it was again shown that all grid resolutions resulted in an accurate prediction of the pressure distributions. Additionally, the fine grid was used with the artificial ice shape at these Reynolds numbers, and minimal improvements were obtained with increased Reynolds numbers. These results further emphasized the utility of real ice shapes in the context of a WMLES simulation framework.

Artificial ice shapes are utilized in engineering analysis primarily due to two reasons: (a) the prediction of accreted ice on a wing is non-trivial, and state-of-the-art ice accretion modeling tools typically provide little information on the roughened surface, and (b) it is numerically challenging

to perform detailed calculations with the real-ice shape with standard computational practices using standard gridding approaches. However, the geometry simplification directly impacts the WMLES approach's predictability at lower grid resolutions.

Chapter 6

Summary and Conclusions

In this dissertation, a comprehensive evaluation of Large Eddy Simulation (LES) techniques for iced airfoils and wings has been conducted. It is demonstrated that LES of roughened ice shapes, even when marginally resolved, can accurately predict critical aerodynamic parameters such as lift, drag, moments, and pressure profiles. The evaluation of WMLES identified a gap in accurately resolving the early-time rime ice shape, which motivated the development and demonstration of a new roughness wall model that acts as a simple augmentation to the classical algebraic equilibrium wall model.

The simulations of five NACA23012 ice geometries, grown and laser-scanned in an icing wind tunnel and a clean geometry, demonstrated the success of wall-modeled LES (WMLES) for ice configurations. These included the early-time rime, streamwise (long exposure to rime), early-time glaze, horn (long exposure to glaze), and spanwise ridge (due to thermal protection system) ice shapes that represent the most critical ice shapes encountered in icing conditions. In particular, improvements were observed in the lift and drag prediction for glaze ice shapes as compared to the established literature. The WMLES results accurately captured the critical stall angle, observed the appropriate decrease in lift in the post-stall region, and yielded good agreement with the rising drag coefficient at high angles of attack.

It was shown that at high angles of attack, when the flow is largely separated, it is necessary to simulate most of the span of the airfoil to minimize spanwise correlations in the stall behaviors. At pre-stall angles, only minimal differences were obtained, specifically due to the inclusion of additional roughness scales by incorporating more of the laser-scanned ice shape.

For the early-time rime geometry, a practical grid resolution (suitable for the cost-effective simulation of an aircraft geometry) was inadequate to accurately predict the critical angle of attack and maximum lift. For this grid resolution, all the roughness scales are sub-grid. Even with additional grid resolution, the prediction of lift and drag is less accurate than the simulations of the glaze ice shapes. From this, it was determined that the rime ice geometry was a good candidate for wall

modeling of rough surfaces.

To address the inaccurate results for moderate resolutions of the rime ice geometry, we developed a novel velocity transformation for turbulent flows over rough walls and extended it as a new wall model. The development of the model required the construction of a DNS database to characterize each roughness topology's deviation from the smooth wall boundary layer. For the first time, a collapse of the velocity profiles in the roughness sublayer was proposed and integrated with a logarithmic layer using a newly defined roughness function. This model relies on a minimal set of geometric parameters, namely, the root-mean-square roughness height, effective slope, and skewness.

This model was then used as an augmentation of the EQWM and was tested on a rough-wall turbulent channel flow and the early-time rime ice geometry. Results demonstrated the utility of the new rough-wall model, particularly in post-stall angles of attack where the EQWM failed to predict stall. In contrast, the new model successfully predicted stall even at coarser resolutions.

The evaluation of WMLES was then extended to three-dimensional swept wing geometries with scallop ice shapes. As is often done in the icing community, a simplified and smoothed version of the scallop ice shape was constructed from the real laser-scanned geometry. Here, both geometries are simulated to determine the impacts of using an artificially constructed ice shape when using WMLES. While excellent agreement was obtained on all grid resolutions when simulating the real, laser-scanned ice shapes, the simulations of the artificial ice shapes were observed to be inaccurate at even the finest resolution.

The smooth leading edge in the artificial-ice shape introduces additional physics not present in the real-ice geometry, including laminar boundary layers, laminar separation, and non-roughness-based turbulent transition. These additional physics stress the assumptions of the equilibrium wall model and, therefore, require a different approach. Additional refinement was added to the leading edge of the artificial wing, and this region was run with a no-slip condition, a more consistent boundary layer for laminar flows. Using this strategy improved the accuracy of the simulations at the cost of additional computational resources (1.5 billion control volumes).

The robustness of these approaches was then tested at Reynolds numbers closer to flight-like conditions, where it was further emphasized that the accuracy of the WMLES for the real-ice shape was independent of both the resolutions tested and the Reynolds number. This is not the case for the artificial ice shape, as it continued to demonstrate inaccurate results for the fine grid resolution at even higher Reynolds numbers.

Artificial ice shapes are commonly used in engineering analysis for two main reasons: (a) predicting ice accretion on a wing is complex, and current ice modeling tools often lack details about rough surfaces, and (b) detailed calculations with real-ice shapes are challenging when using standard gridding practices, that are sometimes unable to handle complex geometries. However, simplifying the geometry impacts the predictability of LES at lower grid resolutions.

The results discussed in this dissertation expand the state-of-the-art method of predicting both

airfoils and wings under a variety of icing conditions. The combination of modeling choices: Voronoi grid generation that can resolve complex roughness elements, low-dissipation numerics, advanced wall models, and dynamic sub-grid models led to reasonable agreement with the experimental data. These modeling efforts provide heightened confidence in the application of WMLES for accurately predicting the complex effects of ice shapes on aerodynamic performance. Collectively, these findings mark a significant step towards bridging the existing modeling gap and advancing our understanding of complex ice shapes' impact on aerodynamic behavior and our ability to simulate them accurately.

Appendix A

Wall-resolved LES of a NACA23012 airfoil under clean and early-time rime conditions

Wall-resolved large-eddy simulations (WRLES) of a "clean" and rime-iced NACA23012 at an angle of attack of 8° are presented, utilizing reduced spanwise extents. The rime ice geometry is equivalent to the one shown in Figure 3.1(a). Table A.1 presents the resolutions of the two cases, along with their spanwise extent, minimum grid spacing, maximum y_w^+, and average y_w^+ (defined at the first grid cell off the wall). Both cases use spanwise periodicity.

For the clean geometry, we employ a stranded mesh topology in the near-wall region, comprising prismatic meshes that yield anisotropic cells. All stranded topologies maintain an aspect ratio of 10:5:1 for streamwise, spanwise, and wall-normal directions. In contrast, due to the inclusion of complex ice geometries in the rime ice surface, we utilize a hexagonally close-packed (HCP) topology near the leading-edge ice region, with locally isotropic cells. For the rime ice geometry, the ice does not go past the chord-normalized streamwise coordinate (s/c) of 0.11, where $s/c = 0$ is located at the leading edge of the airfoil with positive values corresponding to the suction (upper) surface of the airfoil. Therefore, we choose to switch to the anisotropic stranded mesh in the downstream

Table A.1: Grid resolution details for the WRLES simulations.

Case	Number of Cells (B CVs)	Min. grid spacing (normalized by c)	S_p	Max. y_w^+	Avg. y_w^+
Clean	1.16	9.16×10^{-6}	0.05	0.985	0.362
Rime	3.73	1.37×10^{-5}	0.15	1.38	0.769

Figure A.1: Instantaneous flow structures identified with iso-surfaces of Q-criterion of a (a) clean and (b) rime ice geometry colored by streamwise velocity at $\alpha = 8^\circ$ and $Re_c = 1.8 \times 10^6$.

region of the flow ($s/c > 0.15$). This decision significantly reduces computational costs by reducing the overall number of cells. The anisotropic cells in the rime ice case also follow an aspect ratio of 10:5:1.

In Figure A.1, we compare instantaneous structures of the flow field using a matching Q-criterion for both cases. For the clean geometry, we observe a transitional flow at the leading edge of the airfoil. In contrast, evidence of transition very close to the leading edge is observed in the rime ice geometry. In both cases, the flow remains attached throughout the streamwise direction, with a growing turbulent boundary layer. Figure A.2 presents a comparison of lift and drag coefficients to the experimental data of [15]. WRLES results are in good agreement with the experimental data. The current chord-based flow through time for each geometry is 20 and 16 for the clean and rime ice geometries, respectively. In addition to integrated forces, we compare the clean and rime pressure coefficients in Figure A.3. We observe good agreement between both cases, with a minor shift in pressure correctly predicted between them. Figure A.4 compares mean streamwise velocity profiles at several s/c locations with and without rime ice. The boundary layer becomes thicker with the addition of the rime ice, and we observe a faster transition to a turbulent boundary layer. Similarity is observed in all profiles in the outer layer, consistent with Townsend's hypothesis, which posits that the outer layer of turbulence is independent of wall roughness effects except in its role in setting the friction velocity and boundary layer thickness [62, 65]. Despite the roughness ending at $s/c \approx 0.11$,

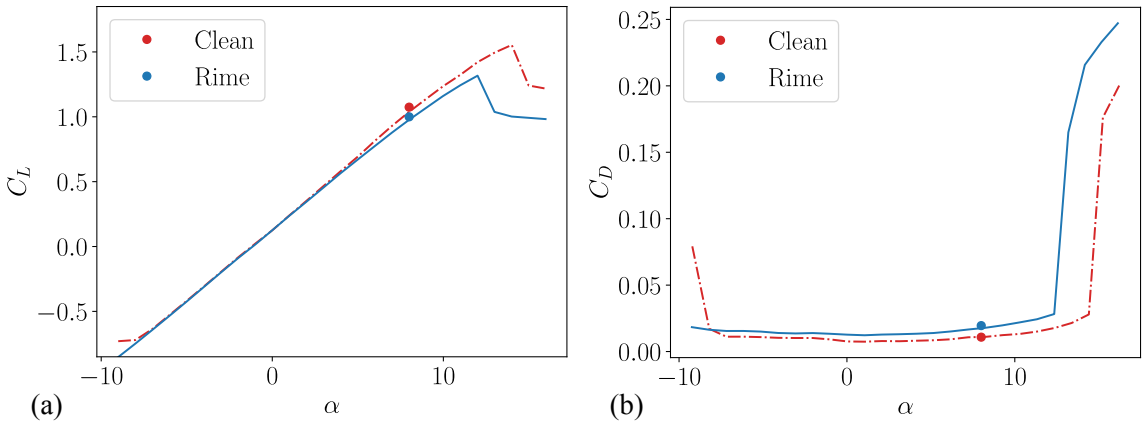

Figure A.2: Sensitivity of (a) lift (C_L) and (b) drag (C_D) coefficients for the clean and rime ice geometries compared to the measurements of [15].

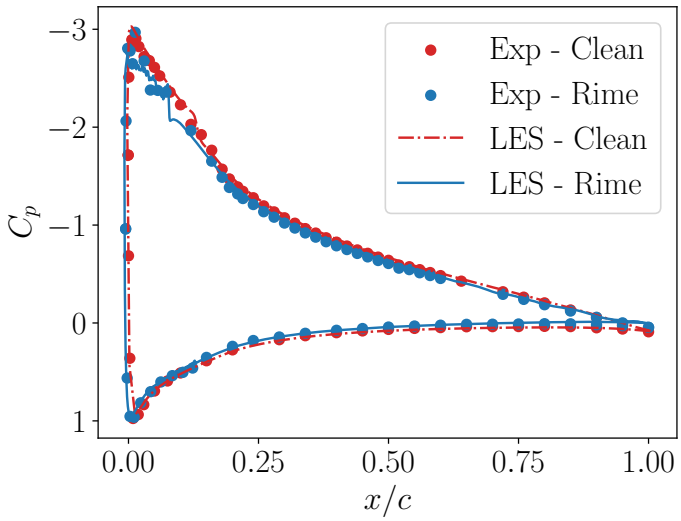

Figure A.3: Pressure coefficients (C_p) for the clean and rime ice geometries compared to the measurements of [15] at $\alpha = 8°$.

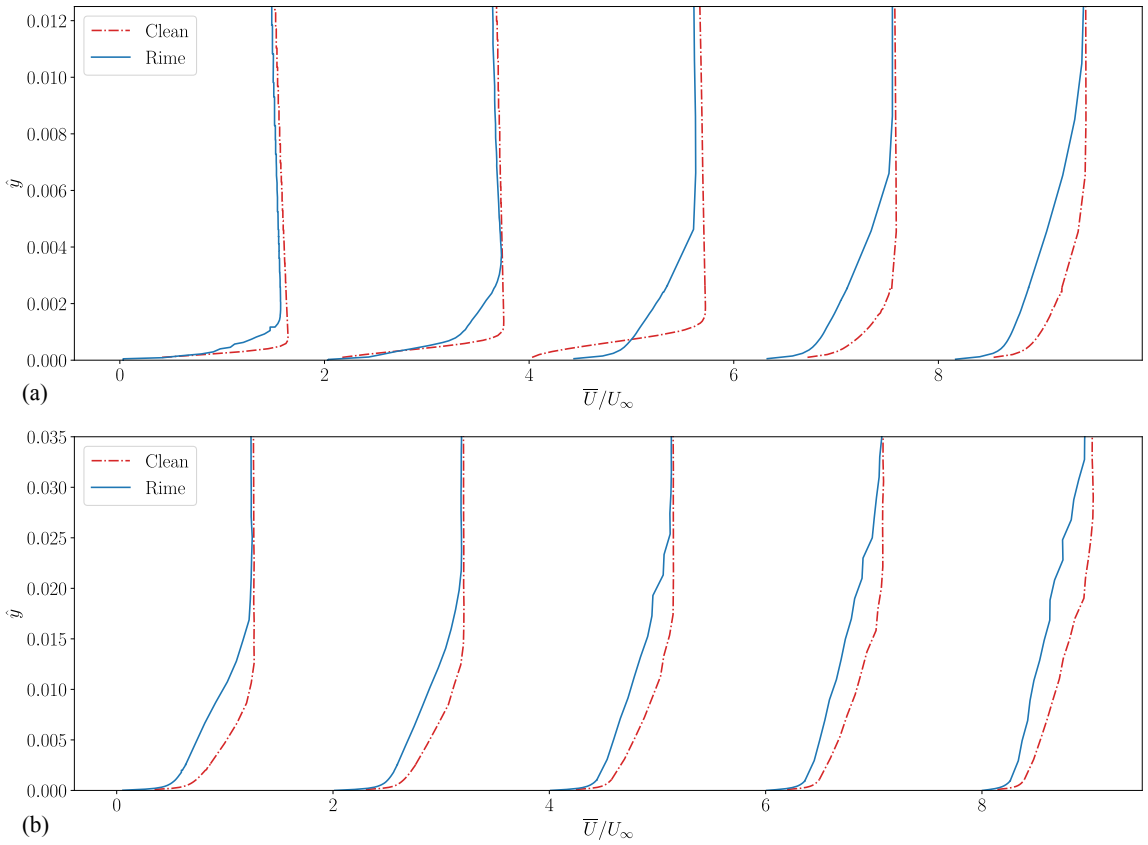

Figure A.4: Profiles of normalized mean streamwise velocity for the clean and rime geometries plotted normal to the wall ($\hat{y}$) at (a) $s/c = 0.05, 0.1, 0.15, 0.2, 0.3$ and (b) $s/c = 0.5, 0.6, 0.7, 0.8, 0.9$ with an offset of two for each profile.

the effect of the rough surface persists in the further downstream velocity profiles, suggesting a flow history effect that persists to the trailing edge of the airfoil.

A.1 Laminar-turbulence transition sensitivity to the presence of ice

The addition of the rough ice surface results in a rapid transition to a turbulent flow. This is observed in Figure A.5, where friction coefficients (C_f) are compared between the clean and rime conditions. The clean airfoil undergoes a natural transition path without any additional disturbances from the local surface. Details of the iso-surfaces of the Q-criterion for the transition of the clean airfoil are shown in Figure A.6. Here, we observe hairpin vortex structures that undergo the eventual breakdown into a turbulent boundary layer. A similar transition is shown in Figure A.7 but at a

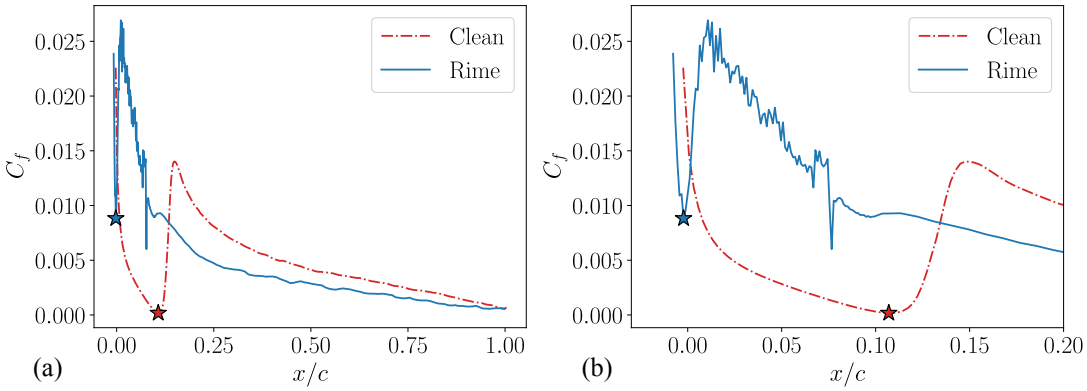

Figure A.5: Friction coefficient (C_f) profiles of the suction (upper) surface for the clean and rime geometries. (a) Full airfoil and (b) zoom-in to the leading edge with the transition location denoted by a star for each case.

much further upstream location due to the inclusion of the leading-edge roughness elements. The boundary layer thickness (δ_{95}, hereafter referred to as δ) obtained using the method of [53] is shown in Figure A.8. The rime ice geometry leads to an immediate increase in the boundary layer height. The red dashed line indicates the height of the zero-pressure gradient (ZPG) laminar boundary layer. In the region prior to transition, indicated by the red star in Figure Q3.5, the boundary layer growth of the clean airfoil aligns with this value. The two dotted lines show the estimated boundary layer thickness for a ZPG turbulent boundary layer, with the red dotted line shifted to approximately begin at the clean airfoil's transition location. For the rime geometry, immediate agreement is observed between the growth of the boundary layer and the ZPG theory in the leading-edge region. In further downstream sections, it is observed that the boundary layer height grows faster than the ZPG theory, which is attributed to the higher angle of attack and adverse pressure gradient in the flow field.

The local friction-based Reynolds number is shown in Figure A.9. As suggested by the boundary layer thickness and friction coefficient, the growth of the friction Reynolds number for the clean geometry is delayed until after the transition location. In contrast, for the rime case, the friction Reynolds number immediately increases to approximately $Re_\tau = 430$ at the transition point between the ice and smooth geometry. The maximum value of Re_τ increases from approximately 1090 to 1500 due to the ice roughness.

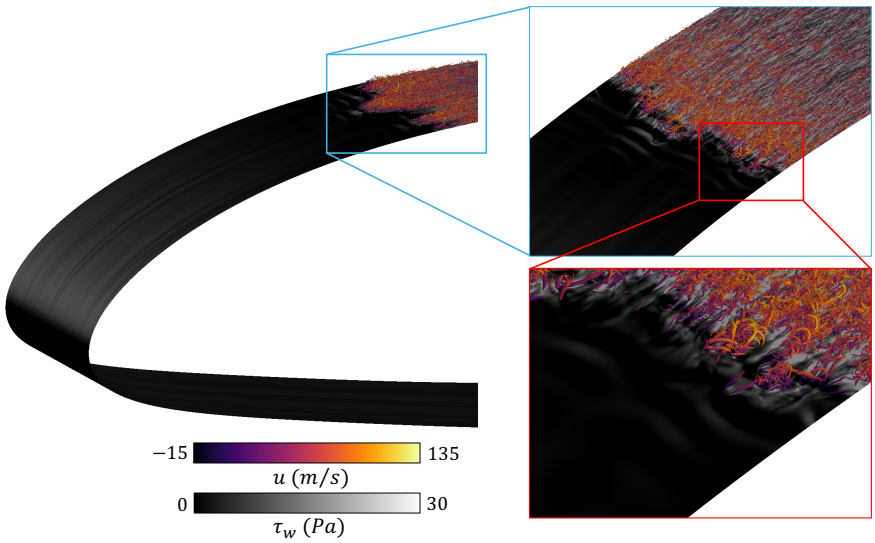

Figure A.6: Iso-surfaces of Q-criterion colored by streamwise velocity and surface contours colored by wall shear stress highlighting the flow structures during the clean airfoil transition.

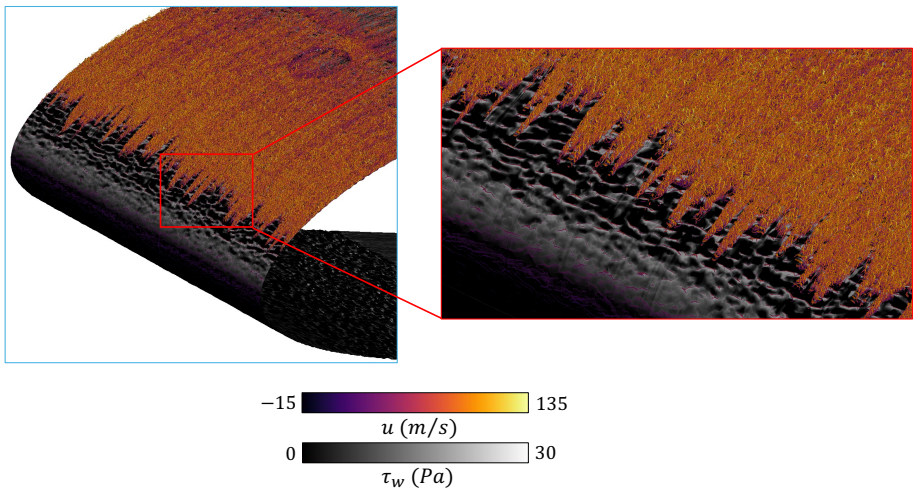

Figure A.7: Iso-surfaces of Q-criterion colored by streamwise velocity and surface contours colored by wall shear stress highlighting the flow structures during the rime airfoil transition.

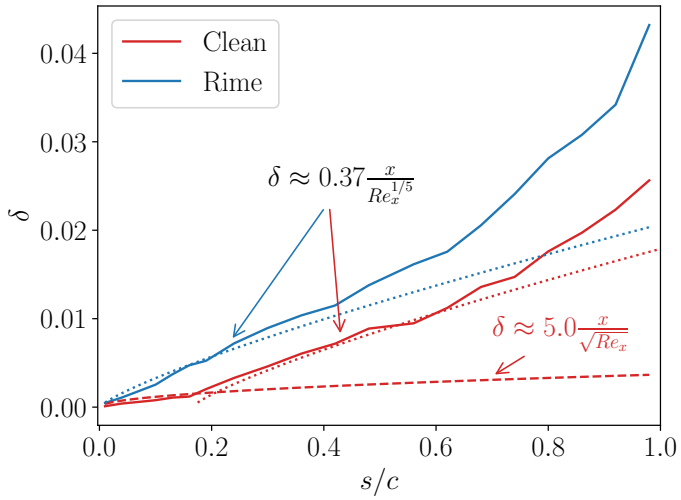

Figure A.8: Boundary layer growth (δ) as a function of s/c for the clean and rime ice geometries. The dotted blue line denotes the ZPG turbulent boundary layer growth function ($\delta \approx 0.37x/Re_x^{1/5}$). The red-dotted line is the same function shifted to the start of the clean transition location. The dashed red line denotes the ZPG laminar boundary layer growth function ($\delta \approx 5.0x/\sqrt{Re_x}$).

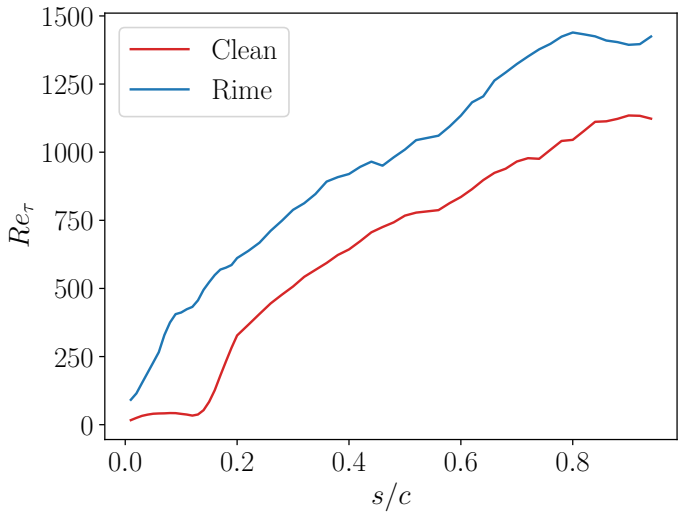

Figure A.9: Friction-based Reynolds number (Re_τ) as a function of s/c for the clean and rime ice geometries

Bibliography

[1] R. Agrawal, S. Bose, and P. Moin. Reynolds number dependence of length scales governing turbulent flow separation with application to wall-modeled large-eddy simulations. *arXiv preprint arXiv:2401.00075*, 2023.

[2] R. Agrawal, M. Whitmore, K. Goc, S. Bose, and P. Moin. Reynolds number sensitivities in wall-modeled large-eddy simulation of a high-lift aircraft. In *Center for Turbulence Research Annual Research Briefs*, pages 229–244, 2023.

[3] N. N. Ahmad, L. Wang, W. K. Anderson, P. Balakumar, P. S. Iyer, and E. J. Nielsen. FUN3D simulations for the 4th AIAA High-Lift Prediction Workshop. In *AIAA Aviation 2022 Forum*, page 3436, 2022.

[4] A. Aihara and S. Kawai. Effects of spanwise domain size on LES-predicted aerodynamics of stalled airfoil. *AIAA Journal*, 61(3):1440–1446, 2023.

[5] M. F. Alam, D. S. Thompson, and D. K. Walters. Hybrid reynolds-averaged navier-stokes/large-eddy simulation models for flow around an iced wing. *Journal of Aircraft*, 52(1):244–256, 2015.

[6] B. Aupoix. Revisiting the discrete element method for predictions of flows over rough surfaces. *Journal of Fluids Engineering*, 138(3):031205, 2016.

[7] J. P. Bons. A review of surface roughness effects in gas turbines. *J. Turbomach.*, 2010.

[8] B. Bornhoft, S. S. Jain, K. Goc, S. T. Bose, and P. Moin. Large-eddy simulations of the NACA23012 airfoil with laser-scanned ice shapes. *Aerospace Science and Technology*, page 108957, 2024.

[9] S. Bose and G. Park. Wall-modeled large-eddy simulation for complex turbulent flows. *Annual Review of Fluid Mechanics*, 50:535–561, 2018.

[10] M. Bragg, A. Khodadoust, R. Soltani, S. Wells, and M. Kerho. Aerodynamic measurements on a finite wing with simulated ice. In *9th Applied Aerodynamics Conference*, page 3217, 1991.

[11] M. B. Bragg, A. P. Broeren, and L. A. Blumenthal. Iced-airfoil aerodynamics. *Progress in Aerospace Sciences*, 41(5):323–362, 2005.

[12] G. A. Bres, S. T. Bose, M. Emory, F. E. Ham, O. T. Schmidt, G. Rigas, and T. Colunius. Large-eddy simulations of co-annular turbulent jet using a Voronoi-based mesh generation framework. In *2018 AIAA/CEAS Aeroacoustics Conference*, page 3302, 2018.

[13] A. P. Broeren. Aerodynamic simulation of ice accretion on airfoils. Technical Report 20110013362, NASA Glenn Research Center, 2011.

[14] A. P. Broeren, H. E. Addy, S. Lee, and M. C. Monastero. Validation of 3-D ice accretion measurement methodology for experimental aerodynamic simulation. Technical Report 2015-218724, NASA Glenn Research Center, 2015.

[15] A. P. Broeren, H. E. Addy, Jr, S. Lee, M. C. Monastero, and S. T. McClain. Three-dimensional ice-accretion measurement methodology for experimental aerodynamic simulation. *Journal of Aircraft*, 55(2):817–828, 2018.

[16] A. P. Broeren, S. Lee, M. B. Bragg, B. S. Woodard, E. Radenac, and F. Moens. Experimental and computational icing simulation for large swept wings. Technical report, United States. Department of Transportation. Federal Aviation Administration, 2023.

[17] A. P. Broeren, S. Lee, B. Woodard, C. W. Lum, and T. G. Smith. Independent effects of reynolds and mach numbers on the aerodynamics of an iced swept wing. In *2018 Atmospheric and Space Environments Conference*, page 3492, 2018.

[18] A. P. Broeren, S. Lee, B. S. Woodward, and M. B. Bragg. Effect of geometric fidelity on the aerodynamics of a swept wing with glaze ice accretion. In *AIAA Aviation Forum*, page 2846, 2020.

[19] A. Buasse and T. O. Jelly. Effect of high skewness and kurtosis on turbulent channel flow over irregular rough walls. *Journal of Turbulence*, 24:57–81, 2023.

[20] A. Busse, M. Lützner, and N. D. Sandham. Direct numerical simulation of turbulent flow over a rough surface based on a surface scan. *Computers & Fluids*, 116:129–147, 2015.

[21] A. Busse and N. D. Sandham. Parametric forcing approach to rough-wall turbulent channel flow. *Journal of Fluid Mechanics*, 712:169–202, 2012.

[22] W. Cabot and P. Moin. Approximate wall boundary conditions in the large-eddy simulation of high reynolds number flow. *Flow, Turbulence and Combustion*, 63(1):269–291, 2000.

[23] S. Camello, S. Lee, C. Lum, and M. B. Bragg. Generation of full-span leading-edge 3D ice shapes for swept-wing aerodynamic testing. In *8th AIAA Atmospheric and Space Environments Conference*, page 3737, 2016.

[24] L. Chan, M. MacDonald, D. Chung, N. Hutchins, and A. Ooi. A systematic investigation of roughness height and wavelength in turbulent pipe flow in the transitionally rough regime. *Journal of Fluid Mechanics*, 771:743–777, 2015.

[25] L. Chan, M. MacDonald, D. Chung, N. Hutchins, and A. Ooi. Secondary motion in turbulent pipe flow with three-dimensional roughness. *Journal of Fluid Mechanics*, 854:5–33, 2018.

[26] P. Chandrashekar. Kinetic energy preserving and entropy stable finite volume schemes for compressible Euler and Navier-Stokes equations. *Communications in Computational Physics*, 14(5):1252–1286, 2013.

[27] X. Chi, Y. Li, H. Addy, G. Addy, Y. Choo, T. Shih, and H. Chen. A comparative study using CFD to predict iced airfoil aerodynamics. In *43rd AIAA Aerospace Sciences Meeting and Exhibit*, page 1371, 2005.

[28] D. Chung, N. Hutchins, M. P. Schultz, and K. A. Flack. Predicting the drag of rough surfaces. *Annual Review Fluid Mechanics*, 53:439–471, 2021.

[29] A. M. Clark, J. P. Slotnick, N. J. Taylor, and C. L. Rumsey. Requirements and challenges for CFD validation within the High-Lift Common Research Model ecosystem. In *AIAA Aviation 2020 Forum*, page 2772, 2020.

[30] F. H. Clauser. Turbulent boundary layers in adverse pressure gradients. *Journal of the Aeronautical Sciences*, 21(2):91–108, 1954.

[31] C. F. Colebrook, T. Blench, H. Chatley, E. H. Essex, J. F. Finniecome, G. Lecey, J. Williamson, and G. G. Macdonald. Correspondence. turbulent flow in pipes, with particular reference to the transition region between the smooth and rough pipe laws (includes plates). *Journal of the Institution of Civil Engineers*, 12:393–422, 1939.

[32] C. F. Colebrook and C. M. White. Experiments with fluid friction in roughened pipes. *Proceedings of the Royal Society London*, 161:367–381, 1937.

[33] M. de Marchis, D. Soccone, B. Milici, and E. Napoli. Large eddy simulations of rough turbulent channel flows bounded by irregular roughness: Advances toward a universal roughness correlation. *Flow Turbulence and Combustion*, 105(2):627–648, 2020.

[34] Y. K. Demirel, O. Turan, and A. Incecik. Predicting the effect of biofouling on ship resistance using CFD. *Applications of Ocean Research*, 62:100–118, 2017.

[35] Q. Du, M. Emelianenko, and L. Ju. Convergence of the Lloyd algorithm for computing centroidal Voronoi tessellations. *SIAM journal on numerical analysis*, 44(1):102–119, 2006.

[36] M. Duclercq, V. Brunet, and F. Moens. Physical analysis of the separated flow around an iced airfoil based on ZDES simulations. In *4th AIAA Atmospheric and Space Environments Conference*, page 2798, 2012.

[37] P. A. Durbin. Reflections on roughness modelling in turbulent flow. *Journal of Turbulence*, 24(1-2):3–13, 2023.

[38] E. Fares. Unsteady flow simulation of the ahmed reference body using a lattice boltzmann approach. *Computers & fluids*, 35(8-9):940–950, 2006.

[39] K. Flack, M. Schultz, and J. Barros. Skin friction measurements of systematically-varied roughness: probing the role of roughness amplitude and skewness. *Flow, Turbulence and Combustion*, 104:317–329, 2020.

[40] K. A. Flack and D. Chung. Important parameters for a predictive model of k_s for zero-pressure-gradient flows. *AIAA Journal*, 60(10):5923–5931, 2022.

[41] P. Forooghi, A. Stroh, F. Magagnato, S. Jakirlić, and B. Frohnapfel. Toward a universal roughness correlation. *Journal of Fluids Engineering*, 139(12):121201, 2017.

[42] L. Fu, M. Karp, S. Bose, P. Moin, and J. Urzay. Shock-induced heating and transition to turbulence in a hypersonic boundary layer. *Journal of Fluid Mechanics*, 909(A8), 2021.

[43] R. W. Gent, N. P. Dart, and J. T. Cansdale. Aircraft icing. *Philosophical Transactions of the Royal Society of London. Series A: Mathematical, Physical and Engineering Sciences*, 358(1776):2873–2911, 2000.

[44] A. S. Ghate, G. K. Kenway, G.-D. Stich, D. Maldonado, and C. C. Kiris. A wall-modeled LES perspective for the high lift common research model using LAVA. In *AIAA Aviation Forum and Exposition 2022*, 2022.

[45] K. Goc. *Towards certification by analysis : large-eddy simulations of commercial aircraft across the flight envelope*. PhD thesis, Stanford University, March 2023.

[46] K. Goc, R. Agrawal, S. T. Bose, and P. Moin. Studies in large-eddy simulations of the NASA transonic common research model. In *Center for Turbulence Research Annual Research Briefs*, pages 13–30, 2022.

[47] K. Goc, R. Agrawal, P. Moin, and S. Bose. Studies of transonic aircraft flows and prediction of initial buffet onset using large-eddy simulations. In *AIAA Aviation 2023 Forum*, page 4338, 2023.

[48] K. Goc, S. T. Bose, and P. Moin. Large eddy simulation of the NASA high-lift common research model. In *AIAA SciTech 2022 Forum*, page 1556, 2022.

[49] K. Goc, O. Lehmkuhl, G. I. Park, S. T. Bose, and P. Moin. Large eddy simulation of aircraft at affordable cost: a milestone in computational fluid dynamics. *Flow*, 1, E14, 2021.

[50] K. Goc, P. Moin, S. T. Bose, and A. M. Clark. Wind tunnel and grid resolution effects in large-eddy simulations of the high-lift common research model. *Journal of Aircraft*, 61(1):267–279, 2024.

[51] C. Gonzalez, M. Karp, and P. Moin. Wall-stress modeling for laminar boundary layers in coarse grids. *Annual Research Briefs*, pages 85–95, 2020.

[52] S. Gottlieb, C.-W. Shu, and E. Tadmor. Strong stability-preserving high-order time discretization methods. *SIAM review*, 43(1):89–112, 2001.

[53] K. P. Griffin, L. Fu, and P. Moin. General method for determining the boundary layer thickness in nonequilibrium flows. *Physical Review Fluids*, 6(2):024608, 2021.

[54] C. Grigson. The full-scale viscous drag of actual ship surfaces and the effect of quality of roughness on predicted power. *Journal of ship research*, 31(03):189–206, 1987.

[55] F. R. Hama. Boundary layer characteristics for smooth and rough surfaces. *Trans. Soc. Nav. Arch. Marine Engrs.*, 62:333–358, 1954.

[56] A. Hamed, W. Tabakoff, and R. Wenglarz. Erosion and deposition in turbomachinery. *Journal of propulsion and power*, 22(2):350–360, 2006.

[57] R. Hann, R. J. Hearst, L. R. Sætran, and T. Bracchi. Experimental and numerical icing penalties of an S826 airfoil at low reynolds numbers. *Aerospace*, 7(4), 2020.

[58] D. R. Hanson, M. P. Kinzel, and S. T. McClain. Validation of the discrete element roughness method for predicting heat transfer on rough surfaces. *International Journal of Heat and Mass Transfer*, 136:1217–1232, 2019.

[59] A. E. Honein and P. Moin. Higher entropy conservation and numerical stability of compressible turbulence simulations. *Journal of Computational Physics*, 201(2):531–545, 2004.

[60] Z. W. Hu, C. L. Morfey, and N. D. Sandham. Wall pressure and shear stress spectra from direct simulations of channel flow. *AIAA journal*, 44(7):1541–1549, 2006.

[61] J. Jansson, C. Johnson, and R. Scott. Predictive euler CFD-resolution of NASA Vision 2030. In *AIAA Aviation 2022 Forum*, page 3589, 2022.

[62] J. Jiménez. Turbulent flows over rough walls. *Annu. Rev. Fluid Mech.*, 36:173–196, 2004.

[63] J. Joo, M. Emory, S. Bose, G. Medic, F. Ham, and O. Sharma. Large-eddy simulation of NACA65 compressor cascade with roughness. *Proceedings of the Center for Turbulence Research Summer Program*, pages 343–352, 2016.

[64] M. A. Jouybari, J. Yuan, G. J. Brereton, and M. S. Murillo. Data-driven prediction of the equivalent sand-grain height in rough-wall turbulent flows. *Journal of Fluid Mechanics*, 912:A8, 2021.

[65] M. Kadivar, D. Tormey, and G. McGranaghan. A review on turbulent flow over rough surfaces: Fundamentals and theories. *International Journal of Thermofluids*, 10:100077, 2021.

[66] C. C. Kiris, A. S. Ghate, O. M. Browne, J. Slotnick, and J. Larsson. HLPW-4: Wall-modeled large-eddy simulation and lattice–boltzmann technology focus group workshop summary. *Journal of Aircraft*, 60(4):1118–1140, 2023.

[67] Y. Kuwata and Y. Kawaguchi. Direct numerical simulation of turbulence over systematically varied irregular rough surfaces. *Journal of Fluid Mechanics*, 862:781–815, 2019.

[68] O. J. Kwon and L. N. Sankar. Numerical simulation of the flow about a swept wing with leading-edge ice accretions. *Computers & fluids*, 26(2):183–192, 1997.

[69] B. König, E. Fares, and A. P. Broeren. Lattice-boltzmann analysis of three-dimensional ice shapes on a NACA 23012 airfoil. In *SAE Technical Papers 2015-01-2084*, 2015.

[70] S. Lee, A. P. Broeren, R. E. Kreeger, M. Potapczuk, and L. Utt. Implementation and validation of 3-D ice accretion measurement methodology. In *6th AIAA Atmospheric and Space Environments Conference*, page 2613, 2014.

[71] O. Lehmkuhl, G. Park, and P. Moin. LES of flow over the NASA common research model with near-wall modeling. In *Center for Turbulence Research Proceedings of the Center for Turbulence Research Summer Program*, pages 335–341. Stanford University, 2016.

[72] O. Lehmkuhl, I. Rodríguez, R. Borrell, J. Chiva, and A. Oliva. Unsteady forces on a circular cylinder at critical reynolds numbers. *Physics of Fluids*, 26(12), 2014.

[73] A. Lozano-Duran, S. T. Bose, and P. Moin. Prediction of trailing edge separation on the NASA juncture flow using wall-modeled LES. In *AIAA Scitech 2020 Forum*, page 1776, 2020.

[74] H. Ma, Y. Li, X. Yang, and L. Ye. Data-driven prediction of the equivalent sand-grain roughness. *Scientific Reports*, 13(1):19108, 2023.

[75] R. Ma, K. Alamé, and K. Mahesh. Direct numerical simulation of turbulent channel flow over random rough surfaces. *Journal of Fluid Mechanics*, 908:A40, 2021.

[76] T. Mauery, J. Alonso, A. Cary, V. Lee, R. Malecki, D. Mavriplis, G. Medic, J. Schaefer, and J. Slotnick. A guide for aircraft certification by analysis. Technical report, NASA, 2021.

[77] P. Moin, K. Squires, W. Cabot, and S. Lee. A dynamic subgrid-scale model for compressible turbulence and scalar transport. *Physics of Fluids A: Fluid Dynamics*, 3(11):2746–2757, 1991.

[78] M. Monastero. *Validation of 3-D ice accretion documentation and replication method including pressure-sensitive paint*. PhD thesis, University of Illinois at Urbana-Champaign, 2014.

[79] E. Napoli, V. Armenio, and M. de Marchis. The effect of the slope of irregularly distributed roughness elements on turbulent wall-bounded flows. *Journal of Fluid Mechanics*, 613:385–394, 2008.

[80] V. Nikora, D. Goring, I. McEwan, and G. Griffiths. Spatially averaged open-channel flow over rough bed. *Journal of Hydraulic engineering*, 127(2):123–133, 2001.

[81] V. Nikora, K. Koll, I. McEwan, S. McLean, and A. Dittrich. Velocity distribution in the roughness layer of rough-bed flows. *Journal of Hydraulic Engineering*, 130(10):1036–1042, 2004.

[82] J. Nikuradse. Laws of flows in rough pipes. Technical report, Technical Memorandum, 1937.

[83] I. Ozcer, A. Pueyo, F. Menter, S. Hafid, and H. Yang. Numerical study of iced swept-wing performance degradation using RANS. Technical report, SAE Technical Paper, 2023.

[84] J. Pan and E. Loth. Detached eddy simulations for iced airfoils. *Journal of Aircraft*, 42(6):1452–1461, 2005.

[85] T. Poinsot and S. Lele. Boundary conditions for direct simulations of compressible viscous flows. *Journal of Computational Physics*, 101:104–129, 1992.

[86] M. Politovich and M. Belo-Pereira. Aircraft icing. *National Center for Atmospheric Research*, pages 68–75, 2003.

[87] M. G. Potapczuk. Aircraft icing research at NASA Glenn Research Center. *Journal of Aerospace Engineering*, 26(2):260–276, 2013.

[88] M. G. Potapczuk, M. Bragg, O. J. Kwon, and L. Sankar. Simulation of iced wing aerodynamics. In *Fluid Dynamics Panel Specialists Meeting*, number NASA-TM-104362, 1991.

[89] Federal Aviation Administration (FAA). Airplane performance and handling qualities in icing conditions. final rule. Technical Report 72, Federal register, 2007.

[90] Federal Aviation Administration (FAA). Airplane and engine certification requirements in supercooled large drop, mixed phase, and ice crystal icing conditions. final rule. Technical Report 79, Federal register, 2014.

[91] M. B. Rivers and A. Dittberner. Experimental investigations of the NASA common research model in the NASA Langley national transonic facility and NASA Ames 11-ft transonic wind tunnel. In *49th AIAA aerospace sciences meeting*, page 1126, 2011.

[92] M. B. Rivers and A. Dittberner. Experimental investigations of the NASA common research model. *Journal of Aircraft*, 51(4):1183–1193, 2014.

[93] C. L. Rumsey, J. P. Slotnick, and A. J. Sclafani. Overview and summary of the Third AIAA High Lift Prediction Workshop. *Journal of Aircraft*, 56:621–644, 2019.

[94] C. L. Rumsey, J. P. Slotnick, and C. D. Woeber. Fourth high-lift prediction/third geometry and mesh generation workshops: Overview and summary. *Journal of Aircraft*, pages 1–18, 2023.

[95] T. Salomone, U. Piomelli, and G. De Stefano. Wall-modeled and hybrid large-eddy simulations of the flow over roughness strips. *Fluids*, 8(1):10, 2022.

[96] S. K. Samal, P. Kumar, and S. K. Saha. Comparative study of surface roughness models in the hydro-thermal characterization of flow over rough walls. *Physics of Fluids*, 35(9), 2023.

[97] R. H. Shaw and U. Schumann. Large-eddy simulation of turbulent flow above and within a forest. *Boundary-Layer Meteorology*, 61(1-2):47–64, 1992.

[98] J. Slotnick, A. Khodadoust, J. Alonso, D. Darmofal, W. Gropp, E. Lurie, and D. Mavriplis. CFD Vision 2030 study: a path to revolutionary computational aerosciences. 2014.

[99] J. P. Slotnick, A. Khodadoust, J. Alonso, D. Darmofal, W. Gropp, E. Lurie, and D. J. Mavriplis. Cfd vision 2030 study: a path to revolutionary computational aerosciences. Technical report, NASA, 2014.

[100] S. Stebbins, E. Loth, A. P. Broeren, M. Potapczuk, and C. Porter. Aerodynamics of a common research model wing with leading-edge ice shape. *Journal of Aircraft*, 58(4):894–906, 2021.

[101] S. J. Stebbins, E. Loth, A. P. Broeren, and M. Potapczuk. Review of computational methods for aerodynamic analysis of iced lifting surfaces. *Progress in Aerospace Sciences*, 111:100583, 2019.

[102] S. J. Stebbins, C. Qin, and E. Loth. Computations of swept wing icing aerodynamics. In *AIAA SciTech Forum*, page 0328, 2019.

[103] M. Stripf, A. Schulz, H.-J. Bauer, and S. Wittig. Extended models for transitional rough wall boundary layers with heat transfer—part i: Model formulations. 2009.

[104] K. L. Suder. *Experimental investigation of the flow field in a transonic, axial flow compressor with respect to the development of blockage and loss*. Case Western Reserve University, 1996.

[105] E. Tadmor. Entropy stability theory for difference approximations of nonlinear conservation laws and related time-dependent problems. *Acta Numerica*, 12(1):451–512, 2003.

[106] Y. Tamaki, H. Asada, R. Takaki, and S. Kawai. Wall-modeled LES around the CRM-HL using fully-automated cartesian-grid-based flow solver FFVHC-ACE. In *AIAA Aviation 2022 Forum*, page 3435, 2022.

[107] Y. Tamaki and S. Kawai. Wall-resolved large-eddy simulation of near-stall airfoil flow at $Re_c = 10^7$. *AIAA Journal*, 61(2):698–711, 2023.

[108] R. P. Taylor, H. W. Coleman, and B. Hodge. Prediction of turbulent rough-wall skin friction using a discrete element approach. 1985.

[109] M. Thakkar, A. Busse, and N. Sandham. Surface correlations of hydrodynamic drag for transitionally rough engineering surfaces. *Journal of turbulence*, 18(2):138–169, 2017.

[110] M. Thakkar, A. Busse, and N. Sandham. Direct numerical simulation of turbulent channel flow over a surrogate for nikuradse-type roughness. *Journal of Fluid Mechanics*, 837:R1, 2018.

[111] A. Townsend, N. Senin, L. Blunt, R. Leach, and J. Taylor. Surface texture metrology for metal additive manufacturing: a review. *Precision Engineering*, 46:34–47, 2016.

[112] J. Varghese and P. A. Durbin. Representation of surface roughness in hybrid turbulence simulations. *Flow, Turbulence and Combustion*, 109(2):255–277, 2022.

[113] J. Vassberg, M. Dehaan, M. Rivers, and R. Wahls. Development of a common research model for applied CFD validation studies. In *26th AIAA applied aerodynamics conference*, page 6919, 2008.

[114] J. Vassberg, E. Tinoco, M. Mani, B. Rider, T. Zickuhr, D. Levy, O. Brodersen, B. Eisfeld, S. Crippa, R. Wahls, et al. Summary of the fourth AIAA CFD drag prediction workshop. In *28th AIAA Applied Aerodynamics Conference*, page 4547, 2010.

[115] Z. J. Wang. Wall-modeled large eddy simulation of the NASA CRM high-lift configuration with the high-order FR/CPR method. In *AIAA Aviation 2022 Forum*, page 3395, 2022.

[116] E. Whalen, A. P. Broeren, and M. Bragg. Considerations for aerodynamic testing of scaled runback ice accretions. In *44th AIAA Aerospace Sciences Meeting and Exhibit*, page 260, 2006.

[117] M. L. Wong, A. S. Ghate, G.-D. Stich, G. K. Kenway, and C. C. Kiris. Numerical study on the aerodynamics of an iced airfoil with scale-resolving simulations. In *AIAA SCITECH 2023 Forum*, page 0252, 2023.

[118] B. S. Woodward, A. P. Broeren, J. M. Diebold, M. B. Bragg, and J. T. Riley. Preliminary testing of low reynolds number aerodynamics for a swept wing with artificial ice roughness. Technical Report DOT/FAA/TC-17/48, Federal Aviation Administration William J. Hughes Technical Center Aviation, 2017.

[119] M. Xiao, Y. Zhang, and F. Zhou. Numerical investigation of the unsteady flow past an iced multi-element airfoil. *AIAA Journal*, 58(9):3848–3862, 2020.

[120] J. Yang, A. Stroh, S. Lee, S. Bagheri, B. Frohnapfel, and P. Forooghi. Prediction of equivalent sand-grain size and identification of drag-relevant scales of roughness–a data driven approach. *Journal of Fluid Mechanics*, 975:A34, 2023.

[121] X. I. Yang, J. Sadique, R. Mittal, and C. Meneveau. Integral wall model for large eddy simulations of wall-bounded turbulent flows. *Physics of Fluids*, 27(2), 2015.

[122] H. Zhang, J. Li, Y. Jiang, W. Shi, and J. Jin. Analysis of the expanding process of turbulent separation bubble on an iced airfoil under stall conditions. *Aerospace Science and Technology*, 114:106755, 2021.